

2014-01-01

Modeling and Simulation of a Lead-free Active Structural Fiber for Multifunctional Composites

Linda Vera

University of Texas at El Paso, lsvera@miners.utep.edu

Follow this and additional works at: https://digitalcommons.utep.edu/open_etd



Part of the [Mechanical Engineering Commons](#)

Recommended Citation

Vera, Linda, "Modeling and Simulation of a Lead-free Active Structural Fiber for Multifunctional Composites" (2014). *Open Access Theses & Dissertations*. 1371.

https://digitalcommons.utep.edu/open_etd/1371

This is brought to you for free and open access by DigitalCommons@UTEP. It has been accepted for inclusion in Open Access Theses & Dissertations by an authorized administrator of DigitalCommons@UTEP. For more information, please contact lweber@utep.edu.

MODELING AND SIMULATION OF A LEAD-FREE ACTIVE STRUCTURAL
FIBER FOR MULTIFUNCTIONAL COMPOSITES

LINDA S. VERA

Department of Mechanical Engineering

APPROVED:

Yirong Lin, Ph.D., Chair

Bill Tseng, Ph.D.

Norman Love, Ph.D.

Charles Ambler, Ph.D.

Dean of the Graduate School

Copyright ©

by

Linda S. Vera

2014

Dedication

To my family that has supported me in every step of my life. Without you this wouldn't be possible. Thank you, I love you all.

MODELING AND SIMULATION OF A LEAD-FREE ACTIVE STRUCTURAL
FIBER FOR MULTIFUNCTIONAL COMPOSITES

by

LINDA S. VERA, B.S. in M.E.

THESIS

Presented to the Faculty of the Graduate School of

The University of Texas at El Paso

in Partial Fulfillment

of the Requirements

for the Degree of

MASTER OF SCIENCE

Department of Mechanical Engineering

THE UNIVERSITY OF TEXAS AT EL PASO

December 2014

ACKNOWLEDGEMENTS

First I would like to express my gratitude to my advisor Dr. Yirong Lin for his constant guidance, teaching, and support throughout my research. Thank you for making me a better student. I would like to thank my committee members, Dr. Norman Love and Dr. Bill Tseng, for agreeing to be a part of my defense committee. To the faculty and staff in the Mechanical Engineering Department, thank you for contributing towards my personal and professional growth with your knowledge, assistance, and friendship. I would like to thank all the members of Dr. Lin's research group for their help and invaluable suggestions throughout this project. A special thanks to Mr. Ricardo Martinez for all his help and patience throughout this research. I would like to thank Ms. Luz Bugarin and Ms. Eira Chico for being such good friends and making things easier for me.

Thank you to my parents, Raul and Hilda, and my siblings, Raul and Naty who supported me every step of the way, for sharing their wisdom and advice. I could not have made it without their prayers, encouragement and love. To my daughter, Samantha, thank you for lighting my days with your smile and love, you are the greatest gift that life could give me. And last but not least, to my husband Alan, thank you for all your support, encouragement, patience, and love; I could not have completed my thesis without you.

ABSTRACT

Piezoelectric materials are widely used in a many areas of science and technology due to their unique electromechanical properties. The transformation of mechanical energy into electrical energy and vice versa caused by the piezoelectric effect has led to the development of piezoelectric sensor devices and actuators used in accelerometers, pressure and vibration meters, micropositioning devices, ultrasound generators, structural health monitoring, etc.

The most used piezoelectric material to this day is lead zirconate titanate $\text{PbZrO}_3\text{-PbTiO}_3$ (PZT) because of its high piezoelectric coefficient and Curie temperature, which allows it to be used in a more wide variety of applications. However, the commercial manufacture and application of PZT represents serious health hazards for humans because of its lead-based nature. The rising need to reduce environmental contamination by lead-based substances has created the urgent need to develop lead-free piezoelectric materials to replace these hazardous materials.

The present work describes the development of a lead-free novel active structural fiber that can be embedded in a composite material in order to perform sensing and actuation, while having a load bearing functionality. The multifunctional composite consists of a carbon core fiber with a piezoelectric coating of barium titanate (BaTiO_3) embedded into a polymer matrix. A one-dimensional micromechanics model of the piezoelectric fiber will be used to characterize the possibility of constructing a structural composite lamina with high piezoelectric coupling, as well as a three-dimensional modeling of the active structural fiber to estimate the effective electroelastic properties of the multifunctional composite.

TABLE OF CONTENTS

ACKNOWLEDGMENTS	v
ABSTRACT.....	vi
TABLE OF CONTENTS.....	vii
LIST OF TABLES	ix
LIST OF FIGURES	x
 CHAPTER 1: INTRODUCTION	 1
1.1 Motivation for Research	3
1.2 Literature Review.....	4
1.2.1 Piezoelectric materials	4
1.2.2 Lead-free vs lead-based piezoelectric ceramics	10
1.2.3 Barium Titanate (BaTiO_3).....	13
1.2.4 Engineering approach to high performance piezoelectrics.....	15
1.2.4.1 Titanate perovskites.....	18
1.2.4.2 Alkaline niobates	26
1.2.4.3 Discussion and continued developments in lead-free piezoceramics.....	32
1.3 Multifunctional Composites.....	34
1.3.1 Electrical and/or thermal conductivity	34
1.3.2 Sensing and actuation	37
1.3.3 Energy harvesting/storage	41
1.3.4 Self-healing capability	45
1.4 Piezoelectric Fiber Composites.....	48
1.4.1 Macro Fiber Composites	48
1.4.2 Hollow Fiber Composites.....	51
1.4.3 Active Fiber Composites	54
 CHAPTER 2: MICROMECHANICS MODELING OF ACTIVE STRUCTURAL FIBER.....	 57
2.1 Introduction.....	57
2.2 One Dimensional Micromechanics Modeling	59

2.3	Double Inclusion Micromechanics Model.....	62
2.4	Results and Discussion	68
CHAPTER 3: FINITE ELEMENT MODELING.....		73
3.1	Introduction.....	73
3.2	3D Finite Element Modeling	73
3.3	Results and Discussion	75
CHAPTER 4: CONCLUSION		80
4.1	Summary of Thesis and Results.....	80
4.2	Recommendations for Future Research	81
REFERENCES		82
VITA		99

LIST OF TABLES

Table 1.1: Room-temperature piezoelectric coefficients (d_{33}), depolarization temperature (T_d), and Curie temperatures (T_c) for the titanate perovskites.	21
Table 1.2: Room-temperature piezoelectric coefficients (d_{33}), depolarization temperature (T_d) and Curie temperatures (T_c) for the alkaline niobate perovskites.	31
Table 2.1: Electroelastic properties of reinforcement and matrix materials.	68
Table 3.1: FEA boundary conditions for identifying each of the constituent properties.	75

LIST OF FIGURES

Figure 1.1: Journal publications related to multifunctional materials. Data collected from Engineering Village web-based information service.	1
Figure 1.2: Crystallographic groups and polarized materials.	6
Figure 1.3: Schematic diagram of 4 different types of polarization mechanisms in a material.	7
Figure 1.4: Dielectric constants of BaTiO ₃ as a function of temperature.	8
Figure 1.5: Dielectric constants of BaTiO ₃ as a function of frequency.	9
Figure 1.6: Schematic structure of a typical bismuth layered structure.	11
Figure 1.7: Schematic of the perovskite structure of BaTiO ₃	12
Figure 1.8a: Polymorphic phase transitions in BaTiO ₃ single crystals observed through changes in the unit cell parameters.	13
Figure 1.8b: Schematic figure of phase transitions in BaTiO ₃ single crystals.	14
Figure 1.9: Characteristic phase diagrams for perovskite solid solutions exhibiting either a (a) morphotropic phase boundary (MPB) or (b) orthorhombic to tetragonal (O-T) polymorphic phase transformation (PPT).	16
Figure 1.10: Role of ‘engineered materials’ approaches to enhance piezoelectric properties.	17
Figure 1.11: Phase diagram of the (Bi _{1/2} K _{1/2})TiO ₃ - BaTiO ₃ solid solution.	22
Figure 1.12: Phase diagram of the (Bi _{1/2} Na _{1/2})TiO ₃ - BaTiO ₃ solid solution.	25
Figure 1.13: Phase diagram of the (Bi _{1/2} Na _{1/2})TiO ₃ - (Bi _{1/2} K _{1/2})TiO ₃ solid solution.	25
Figure 1.14: Ternary phase diagram for the BaTiO ₃ -(Bi _{1/2} Na _{1/2})TiO ₃ - (Bi _{1/2} K _{1/2})TiO ₃ solid solution.	26
Figure 1.15: Phase diagram of the KNbO ₃ -NaNbO ₃ solid solution.	30
Figure 1.16: Piezoelectric coefficient over depolarization temperature for the various families of lead-free and including lead based piezoelectric ceramics.	33
Figure 1.17: Electrical conductivity of CNT/epoxy nanocomposites at various CNT concentrations. Percolation threshold is 0.04 wt.%.	36
Figure 1.18: Effect of CNT aspect ratio on percolation threshold for CNT nanocomposites with varying dispersion states.	36
Figure 1.19: Nanograss-enhanced polymer adhesive joint for improved through-thickness thermal conductivity.	37
Figure 1.20: Hollow piezoelectric fiber with radial poling and longitudinal actuation of fiber.	39
Figure 1.21: Stanford-Multi-Actuator-Receiver-Transduction (SMART) layer concept of integrated sensor/actuator network in a composite laminate.	40
Figure 1.22: Resistance of inkjet-printed 160 μm-wide electrode under static loading for several electrode thicknesses.	43
Figure 1.23: Construction of (a) conventional non-structural polymer lithium-ion battery and (b) new structural battery.	43
Figure 1.24: Energy density and specific modulus of multifunctional structural capacitors. Dashed line represents design goal for true multifunctionality.	45
Figure 1.25: Illustration of self-healing of cracks in polymers by the use of a microencapsulated healing agent and a catalyst for polymerizing the healing agent.	46
Figure 1.26: Illustration of self-healing of cracks in polymers by the use of a microencapsulated healing agent and a catalyst for polymerizing the healing agent.	47
Figure 1.27: Schematic showing the order of different layers in the macro-fiber composite actuator.	49

Figure 1.28: Fabrication process of the macro-fiber composite piezofibers.	49
Figure 1.29: Fabrication of the macro fiber composites.	50
Figure 1.30: Fabrication of the macro fiber composites.	51
Figure 1.31: MFCX fabrication process.	52
Figure 1.32: Schematic showing of hollow fiber lamina fabrication.....	53
Figure 1.33: Cross section of an Active Fiber Composite with glass rods.	54
Figure 1.34: Schematic of the manufacturing process of the active fiber composite.	55
Figure 1.35: Schematic of the active fiber composites.	55
Figure 2.1: Schematic showing the cross-section of the novel multifunctional fiber.....	58
Figure 2.2: Schematic demonstrating the relationship between the fiber aspect ratio and fiber volume fraction.	61
Figure 2.3: Schematic illustrating of the three phase active composites.	66
Figure 2.4: Schematic drawing of the ASF in the global coordinate system.....	67
Figure 2.5: Resulting electromechanical coupling of the ASF with respect to the aspect ratio. ..	68
Figure 2.6: Result for the active fiber coupling of a lamina consisting of the active structural fiber to that of bulk piezoelectric material, with respect to the volume fraction of the active fiber for various fiber aspect ratios.....	69
Figure 3.1: FEM model of multifunctional composite with the front view shown on the right. ..	73
Figure 3.2: Effective Young's modulus with respect to ASF volume fraction, (a) longitudinal Young's modulus, (b) transverse Young's modulus.....	76
Figure 3.3: FEA Effective Shear modulus with respect to ASF volume fraction, (a) longitudinal Shear modulus, (b) transverse Shear modulus.....	78
Figure 3.4: FEA Effective longitudinal dielectric const. with respect to ASF volume fraction... ..	79

CHAPTER 1

INTRODUCTION

With the ever-increasing demand for new technology to satisfy the current and developing scientific needs, the arrival of nanotechnology opened new doors for many fields and has lead to the introduction of smart materials. Some examples of 'smart' materials are piezoelectrics, electro- and magnetostrictive materials, shape-memory alloys, electrorheological liquids etc. These materials, also referred to as multifunctional materials, are capable of carrying external mechanical loading as well as exhibit one or more additional performance functions. They are integrated material systems that serve multiple roles such as structural load bearing, energy absorption, thermal management, sensing, power generation, vibration control, etc. The number of publications dealing with various aspects of the mechanics of multifunctional materials has increased noticeably in recent years clarifying the importance and success of smart materials. Fig. 1.1 shows the number of English language refereed journal articles in multifunctional materials and structures and how it has been increasing progressively since 2000, based on data collected from the Engineering Village web-based information service [152].

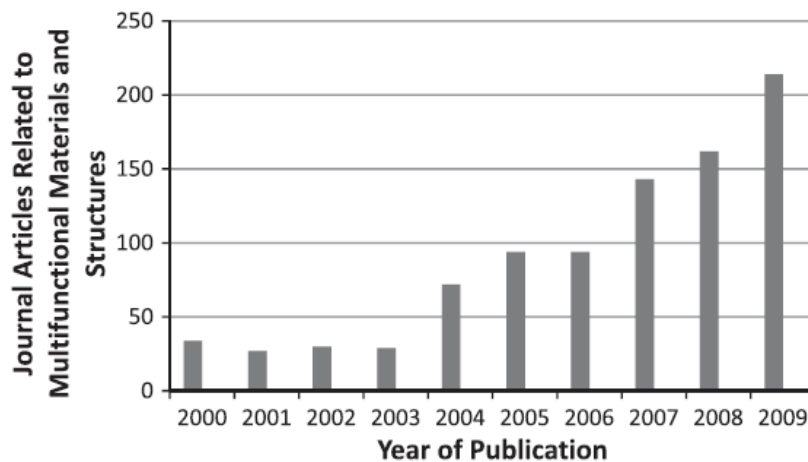


Fig. 1.1. Journal publications related to multifunctional materials. Data collected from Engineering Village web-based information service.

Although many multifunctional materials exist, piezoelectric materials, which possess the capability of coupling the energy between mechanical and electrical domains, remain the most commonly used smart material because of their excellent structural sensing and actuation properties. Manufacturing and industrial are currently the largest application markets for piezoelectric devices, followed by the automotive industry. Their popularity is mainly because piezoceramics have a high stiffness which provides them with strong, voltage-dependent actuation authority, as well as a great capability to interact with dynamic systems at frequencies extending six orders of magnitude. But however many benefits they offer over traditional engineering materials for structural design, monolithic piezoceramic devices impose some restrictions for its practical use in real-world applications. The extremely fragile and brittle nature of the material requires a lot of care in the handling and bonding procedures [2]. Furthermore, the congruity with curved surfaces is extremely low requiring extra treatment of the surfaces and additional manufacturing capabilities. To solve the scantiness of monolithic piezoceramic materials, a lead-free novel active piezoelectric structural fiber embedded in polymer matrix was developed that can be placed in a composite material to perform sensing and actuation, as well as having a load bearing functionality. This will allow the multifunctional material to be designed with several embedded functions such as power generation, vibration sensing control, damping, and structural health monitoring. And not only will this fiber overcome piezoceramic limitations like stress, it will also provide a solution to the ever-increasing issue of environmental contamination and health hazards caused by lead-based components. This thesis shows the process of modeling and simulation of this active structural fiber to estimate its electroelastic properties.

1.1 Motivation for Research

In recent years the attention given to smart materials has experienced an enormous increase. One of these smart materials is piezoelectrics that because of its ability to convert mechanical energy to electrical energy and vice versa have a wide variety of uses. This dual nature enables piezoelectric materials to be used in electromechanical systems such as ultrasound sensors and generators, electromechanical actuators and transducers, nanopositioning devices and many more [3]. Current applications of piezoelectric devices extend to automotive fuel injection, accelerometers, piezoelectric transformers and motors, vibration control, inkjet printers and etc.[4-7].The most used piezoelectric material to this day is lead zirconate titanate PbZrO_3 - PbTiO_3 (PZT) because of its high piezoelectric coefficient and Curie temperature, which allows its use in a broader set of functions. Additionally, a variety of dopants can be used to manufacture a range of "hard" and "soft" PZT piezoelectrics tuned for specific applications[7]. However, the manufacture and application of PZT as commercial products represents serious environmental and health hazards because of the improper disposal of lead and its evaporation during high temperature sintering. In the last decade legislation governing the use of lead containing compounds has been enforced in the EU and the State of California including the draft Directives on Waste from Electrical and Electronic Equipment (WEEE), Restriction of Hazardous Substances (RoHS), and End-of-Life Vehicles (ELV) [8-12].

The rising manufacturing and application of lead-based substances, more specifically lead zirconate titanate, has created the urgent need to develop lead-free piezoelectric materials to replace lead-based materials and reduce health and environmental issues.

The present work describes the modeling and simulation of a lead-free novel active structural fiber that can be embedded in a composite material in order to perform sensing and

actuation, while having a load bearing functionality. As mentioned before, this active fiber will solve monolithic piezoelectric inadequacies that restrain their usage in real-world applications. The multifunctional composite consists of a carbon core fiber with a piezoelectric coating of barium titanate (BaTiO_3) and will then be embedded into a polymer matrix. Configuration of the material in this way is advantageous because typical crystalline materials have much higher strengths in the fiber form due to reduced volume fractions of flaws during fabrication [13]. In addition to providing toughness to the fragile fibers, the flexible nature of polymer matrix will allow the material to be more easily used in curved surfaces. A one-dimensional micromechanics model of the piezoelectric active fiber will be used to characterize the possibility of constructing a structural composite lamina with high piezoelectric coupling. Also a three-dimensional modeling and simulation of the active structural fiber will be used to estimate the effective electroelastic properties of the multifunctional composite.

1.2 Literature Review

This chapter is devoted to explain the foundations for the active structural novel studied in this thesis. It contains a brief summary of important properties, constants, and terminology of piezoelectric materials. Such terms to be reviewed are dielectric permittivity, piezoelectric effect, and crystal structure, which impose the most significance to the work presented here.

1.2.1 Piezoelectric materials and their properties

The word “piezoelectricity” is derived from the Greek “piezein”, which means to squeeze or press, hence the term piezoelectric, which is a material with the power to generate electricity as a result of mechanical pressure. The piezoelectric effect was discovered by Jacques and Pierre

Curie in 1880 when they found that certain crystals undergo polarization when a mechanical strain was applied. These same materials were found by the Curies to become deformed when they were exposed to an electric field. These two manifestations of piezoelectricity are called direct and converse piezoelectric effects respectively. In the direct effect, a change in polarization D_i occurs due to an applied stress σ_j

$$D_i = d_{ij}\sigma_j$$

where d_{ij} is the piezoelectric coupling coefficient. While the converse effect describes the strain S_i generated in a piezoelectric material in response to an applied electric field E_j .

$$S_i = d_{ij}E_j$$

The magnitude of the piezoelectric coefficient varies from 1 pC/N in quartz crystals to about 1000 pC/N in high-quality barium titanate (BaTiO_3) and lead zirconate titanate (PZT) ceramics [14]. A condition necessary for a crystal to exhibit the piezoelectric effect is a non-centro symmetry in the crystal since it is required for polarization. From the 32 crystal groups only 21 groups have a non-symmetric structure, and even when cubic class 432 lacks a center of symmetry it is not a piezoelectric since it's nonpolar. We are therefore left with 20 crystal groups that show piezoelectricity. Ten of these groups have a unique crystallographic axis and can have an electric dipole when no field is applied. These materials are defined as pyroelectrics, materials which show a change in polarization due to a change in temperature [15]. Under the pyroelectric category, another class of material exists which can change the direction of polarization with an applied external field; these materials are called ferroelectrics. The relationship between the different symmetry groups discussed above is shown in Fig. 1.2.

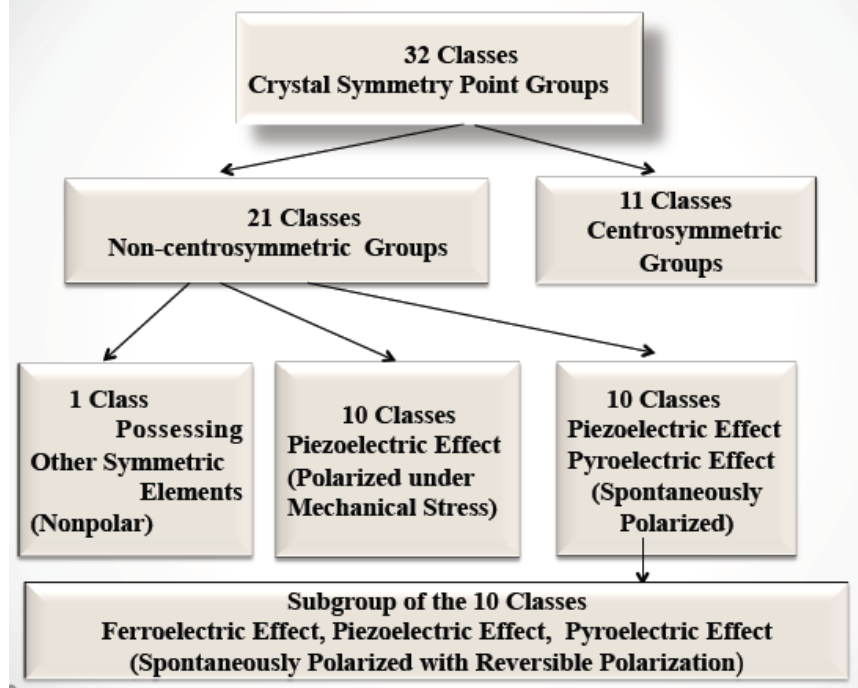


Fig. 1.2. Crystallographic groups and polarized materials.

The first listing of piezoelectric materials was collected by Victor Moritz Goldschmidt in 1926 [16]. It was not until 1940's that barium titanate was discovered be a ferroelectric and possessed an excellent high dielectric constant [17]. Having an understanding of the dielectric properties of a material is important to achieve a good performance in electronic devices or systems. While the term insulator implies low electrical conduction, dielectric typically means a material with high polarization. The latter is expressed by a number called the relative permittivity, also known as dielectric constant. Permittivity is a term used to indicate the energy storing capacity and the ability of a material to be polarized by an electrical field. Permittivity ϵ_{ij} is a second rank tensor which equation can be written as

$$D_i = \epsilon_{ij}E_j$$

The dielectric displacement vector D_i is equal to the sum of the charge stored on the electrodes and any induced charge from the polarization vector P_i

$$D_i = \epsilon_0 E_i + P_i$$

where ϵ_0 is the dielectric permittivity of vacuum. The dielectric constant or relative dielectric permittivity of a material is more often used and is expressed by

$$K_{ij} = \epsilon_{ij}/\epsilon_0$$

Commonly, dielectric constants for most ceramics and polymers are in the range of 2-10. Whereas for high dielectric constant materials such as water (K~80) and BaTiO₃ (K~1000) their dielectric constants are very high based on their polarization mechanisms due to ferroelectric phase transformations. The 4 types of polarization mechanisms while polarized and un-polarized are shown in Fig. 1.3.

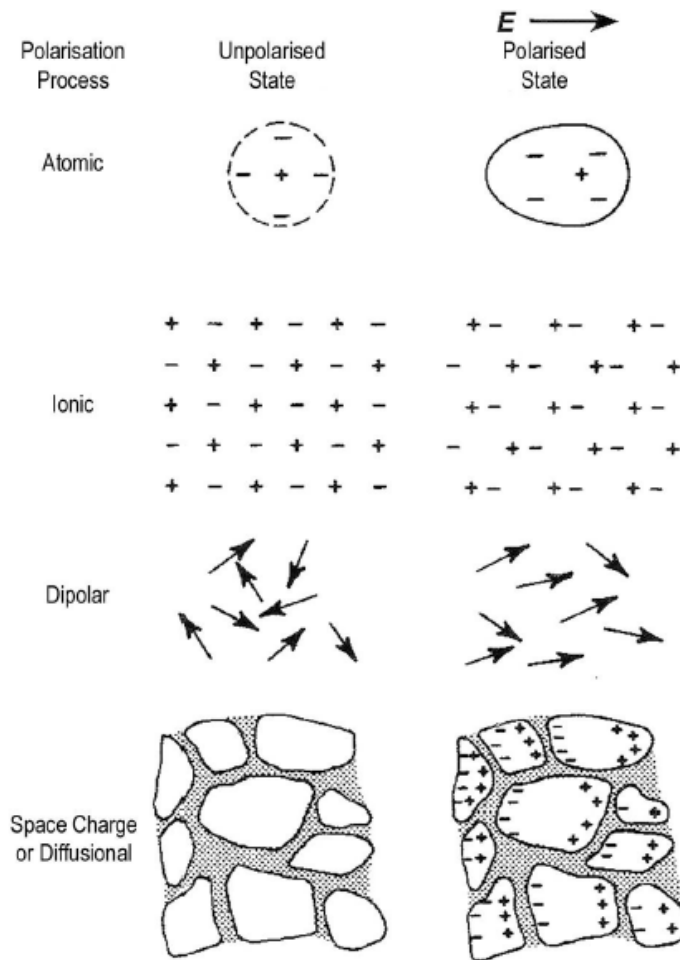


Fig. 1.3. Schematic diagram of 4 different types of polarization mechanisms in a material. [35]

BaTiO₃ was the first material that was used to manufacture devices such as dielectric ceramic capacitors, multilayer capacitors, etc. due to its high dielectric constant and low dielectric loss. The values of the dielectric constant depend on the synthesis route, which means purity, density, grain size etc [18]. While all techniques have their own advantages for obtaining ceramics with certain properties, the selected synthesis method depends on cost and end application. Some of the synthesis techniques used to develop BaTiO₃ ceramics are: conventional solid-state reaction, chemical synthesis (Sol-Gel, Hydrothermal, Coprecipitation, Polymeric precursor), and mechanochemical synthesis. Kim et al. [19] and Boulos et al. [20] reported the influence of grain size on the dielectric constant value, and with the only difference being the synthesis method used for the preparation, they both concluded that as grains size increased, the dielectric constant decreased.

Another two factors the dielectric constant is dependent on are temperature and frequency. Numerous amounts of papers have reported the temperature dependence of the dielectric constant. Figure 1.4 shows the temperature dependence of the dielectric constant measured with a small field along the pseudo-cubic edge [21].

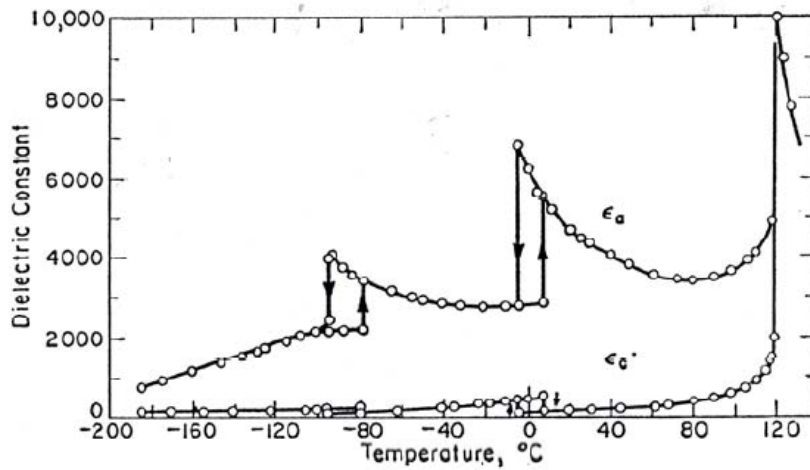


Fig. 1.4. Dielectric constants of BaTiO₃ as a function of temperature [21].

At lower temperatures the dielectric constant will mostly increase, while at higher temperatures (past Curie temperature~) it will decrease drastically.

To prove the frequency dependence of the dielectric constant, Benlahrache et al. [22] used milling and calcination to prepare pure BaTiO₃ and measure the frequency. At room temperature, for frequencies below 1kHz the dielectric constant decreased, while for higher frequencies the value was almost constant, as shown in Figure 1.5.

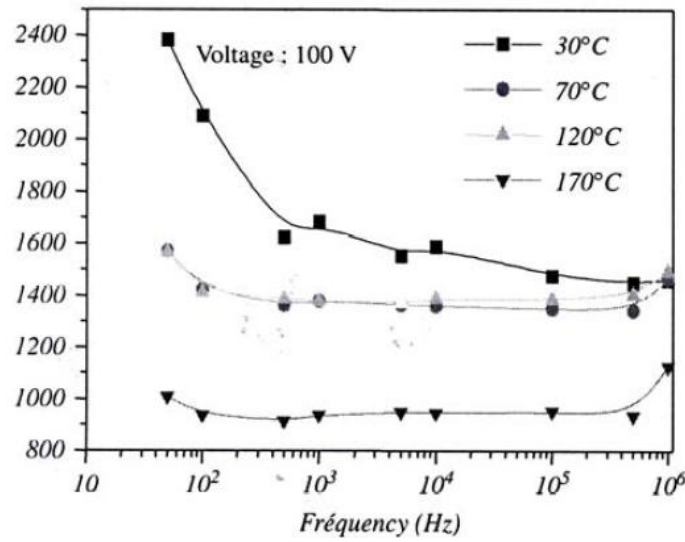


Fig. 1.5. Dielectric constants of BaTiO₃ as a function of frequency [22].

As explained above, the relative permittivity or dielectric constant is affected by heat and applied frequency, which alters the dipoles within the material. Since the dipole's orientation has been randomized, it is difficult to react instantaneously to changes in the applied electric field and losses of energy occur. Therefore, relative permittivity can be written as $\epsilon = \epsilon' + i\epsilon''$, where ϵ' is the real part of the dielectric constant, and ϵ'' is the imaginary component. The ratio of this imaginary component to the real part is called dielectric loss $\tan \delta = \epsilon''/\epsilon'$, which is the amount of power lost in the form of heat generated by an electric field. Usually, low dielectric loss is a factor desired when developing high quality dielectric materials.

1.2.2 Lead-free vs. lead-based piezoelectric ceramics

Lead oxide based piezoelectric materials, such as lead zirconate titanate ($\text{PbZrO}_3\text{--PbTiO}_3$ or PZT) and PZT-based multicomponent materials, are the most widely used materials for electronic devices such as actuators, sensors and transducers, because of their excellent piezoelectric properties. Piezoelectric coefficients (d_{33}) as high as 779 pC/N have been reported for modified PZT [23] with Curie temperatures (T_c) in the range 300–400 °C.

However, the environmental and health hazards of lead are well-known, and PZT and PZT based materials contain large amounts of lead (more than 60 wt%). For example, lead and lead derivatives can be highly toxic if they are ingested or inhaled. Furthermore, if someone is constantly exposed to lead, gradual accumulation in the body can occur. Absorption of toxic by the red blood cells can cause high blood pressure and circulate through the body where they accumulate in lipids of soft tissues. Every organ system in the body (i.e. kidneys, brain, nervous system) can be seriously, if not irreversibly damaged. For children, the exposure to high lead concentrations can cause slowed growth, behavior disorders or learning disabilities [24]. The evaporation of lead during high-temperature sintering has created a rising concern about the manufacturing of products containing PZT. Recycling and disposal of devices containing lead-based materials is also of great concern, especially in consumer products such as cars, computers, and medical devices. Through the world, the growing demand for lead-free materials that are benign to the environment and human health has made governments take an action on this issue. In the last decade, legislation governing the use of lead containing compounds has been enforced in the EU and the State of California including the draft Directives on Waste from Electrical and Electronic Equipment (WEEE), Restriction of Hazardous Substances (RoHS) and End-of-Life Vehicles (ELV) [25–28]. Thus, the interest to reduce environmental contamination

by lead-based substances has given the motivation to develop alternative lead-free piezoelectric materials.

To date, the two types of lead-free piezoelectric ceramics have drawn the most attention and been extensively studied are: bismuth-layered and perovskite structures. Bismuth layered structure ceramics are featured with low permittivity and high Curie temperature, and are therefore been widely studied for high-temperature sensor applications. Some examples of bismuth layered ceramics are Lithium Niobate (LiNbO_3) and Lithium Tantalate (LiTaO_3) for which their Curie Temperatures are 1210°C and 660°C respectively. A typical bismuth layered structure is shown in Figure 1.6 [29]. The structure consists of perovskite layers and $(\text{Bi}_2\text{O}_2)^{2+}$ layers that separate them periodically.

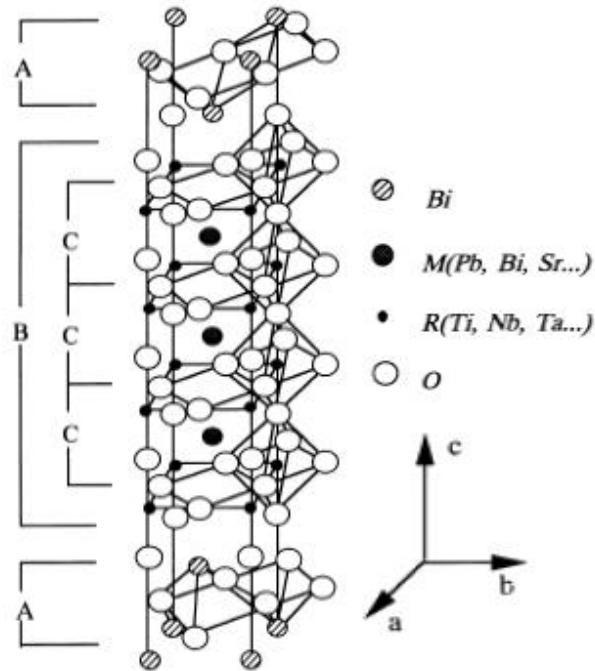


Fig. 1.6. Schematic structure of a typical bismuth layered structure [29].

Bismuth layer structures usually have high Curie temperatures ($600^\circ\text{C}\sim 900^\circ\text{C}$), much higher than those of the lead-based materials ($200^\circ\text{C}\sim 400^\circ\text{C}$) [30-31]. Nevertheless, due to the

anisotropic nature of their structures, the spontaneous polarization within the materials during poling is limited within a two-dimensional plane (the ab plane shown in Fig. 4) [32-33], which results in the low piezoelectric properties in bismuth layer structured ceramics ($d_{33} < 20 \text{pC/N}$).

Meanwhile, perovskite structures have very good electromechanical and piezoelectric properties. Perovskite piezoelectrics are of great importance since most of the piezoelectric materials used today belong to this family. This structure, which has a general formula of ABO_3 , is described by a simple cubic unit cell with oxygen atoms at the face centers, with its corners occupied by large cations "A" (such as Ba, Pb, K, Na, etc.), and a smaller cation "B" (such as Ti, Nb, Zr, Mg, etc.) located in the center of the cube. Figure 7 shows a schematic drawing of the structure

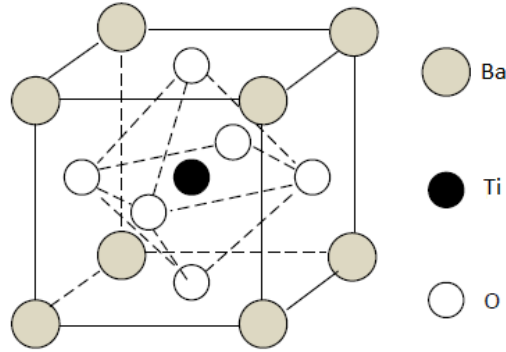


Fig. 1.7. Schematic of the perovskite structure of BaTiO_3

In general, any structure similar to Figure 1.7 can be considered a perovskite structure even if it's slightly distorted. In some cases there can be multiple cations in the A or B site. For example, PZT has both Zr and Ti at the B site; also, sodium potassium niobate (NKN) has both Na and K at the A site. It all depends on how well can this cations fit together to form the perovskite structure, and this can be predicted by the following relation

$$t = \frac{(R_A + R_O)}{\sqrt{2}(R_B + R_O)}$$

where t is the "tolerance factor" and R_o , R_a , and R_b the ionic radii of the oxygen, A and B cations, respectively. For a perfect perovskite structure where the bonding between the ions is ideally, the tolerance factor is 1.0 [34]. If $0.95 < t < 1.0$ the structure is cubic, those with $t < 0.95$ are non-ferroelectric, and when t is slightly greater than 1 they are ferroelectric. A typical perovskite material is Barium Titanate (BaTiO_3), which was the first piezoelectric ceramic in which ferroelectricity was discovered.

1.2.3 Barium Titanate (BaTiO_3)

The first piezoelectric ceramic developed on a large scale was Barium titanate. It was discovered in the 1940s and had the highest coupling coefficients among previously known materials (except Rochelle salt) [35] BaTiO_3 was more stable chemically than Rochelle salt, had a wider temperature range, and was easy to produce. These factors made BaTiO_3 an important technological material for many decades [35]. Although, in present days, this material does not have a very high piezoelectric constant, it does have a very high permittivity, making it a good material for capacitors [36]. Barium Titanate has a perovskite crystal structure and it goes through various phase transitions as a function of temperature as shown in Figure 1.8a [37].

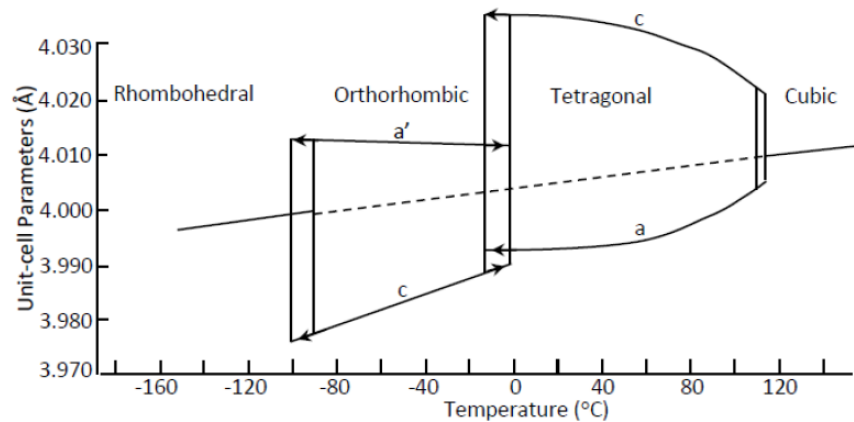


Fig. 1.8a. Polymorphic phase transitions in BaTiO_3 single crystals observed through changes in the unit cell parameters [37]

At temperatures near 0°C , a change from the orthorhombic to tetragonal phase can be observe, whereas a transition from tetragonal to cubic (paraelectric phase) occurs at 120°C . The low Curie temperature of Barium titanate results from this phase transition at 120°C [38]. In contrast to the morphotropic phase boundary (MPB) which is composition-dependent, each of these temperature-dependent phase transitions is referred to as a polymorphic phase transition (PPT). More recent studies by Wada et al. on single crystal BaTiO_3 found that these phase transitions can also be induced by an applied electric field [39]. They found that the room temperature structure can change from tetragonal to monoclinic under applied electric field amplitude of 10 kV/cm and then to rhombohedral at an amplitude of 30 kV/cm [39].

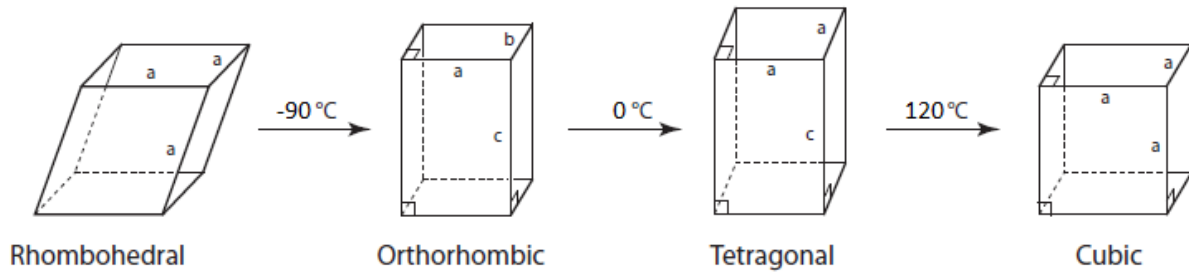


Fig. 1.8b. Schematic figure of phase transitions in BaTiO_3 single crystals

Despite these low transition temperatures, barium titanate ceramics made out of ultra pure powder produced by hydrothermal synthesis and manufactured by microwave sintering showed high electromechanical properties $d_{33} = 350\text{ pC/N}$, $k_p = 0.36$ and $e_{33} = 4200$ [40]. It is important to reproduce the processing since these properties are influenced by grain size, density, and defect in the structure.

Recent developments in BaTiO_3 materials have reported extraordinary non-piezoelectric properties including piezoresistivity [41], permittivity up to $\sim 10^6$ in carefully prepared nanocrystalline ceramics [42], and very large reversible strain up to $\sim 0.8\%$ due to defect-

mediated domain switching [43]. BaTiO₃ continues to serve as a model system for more fundamental investigations, as in reference [44, 45].

1.2.4 Engineering approach to high performance lead-free piezoelectrics

(Taken from[46]: S. Leontsev and R. Eitel, "Progress in engineering high strain lead-free piezoelectric ceramics", Science and Technology of Advanced Materials, v.l 1, 044302, 2010)

Traditionally, enhancement of the electromechanical response in piezoelectric materials is achieved by compositional engineering. Following this approach the composition of a material or solid-solution is optimized to bring the material into proximity with a structural instability such as polymorphic phase transition (PPT) or morphotropic phase boundary (MPB) [47]. Hypothetical phase diagrams used for compositional engineering of both PPT- and MPB-based piezoceramic systems and the resulting temperature dependence of the piezoelectric response are illustrated in Figure 1.9. In both cases, improved piezoelectric properties result from a combination of (i) a ‘softening’ the crystal lattice due to the coexistence of two phases with equivalent free energies and (ii) increased alignment of ferroelectric domains following poling enabled by the large number of equivalent polarization directions from the different symmetries of the two phases. As illustrated in figure 9(c), MPB-based piezoceramics typically exhibit relatively flat temperature dependence of the poled piezoelectric properties and broad usage temperatures approaching $\sim 1/2T_c$. Conversely, PPT-based piezoceramics generally exhibit large temperature dependence of the piezoelectric coefficient and rapid degradation of poled piezoelectric coefficient (due to partial depoling) subsequent to temperature excursions close to the PPT temperature.

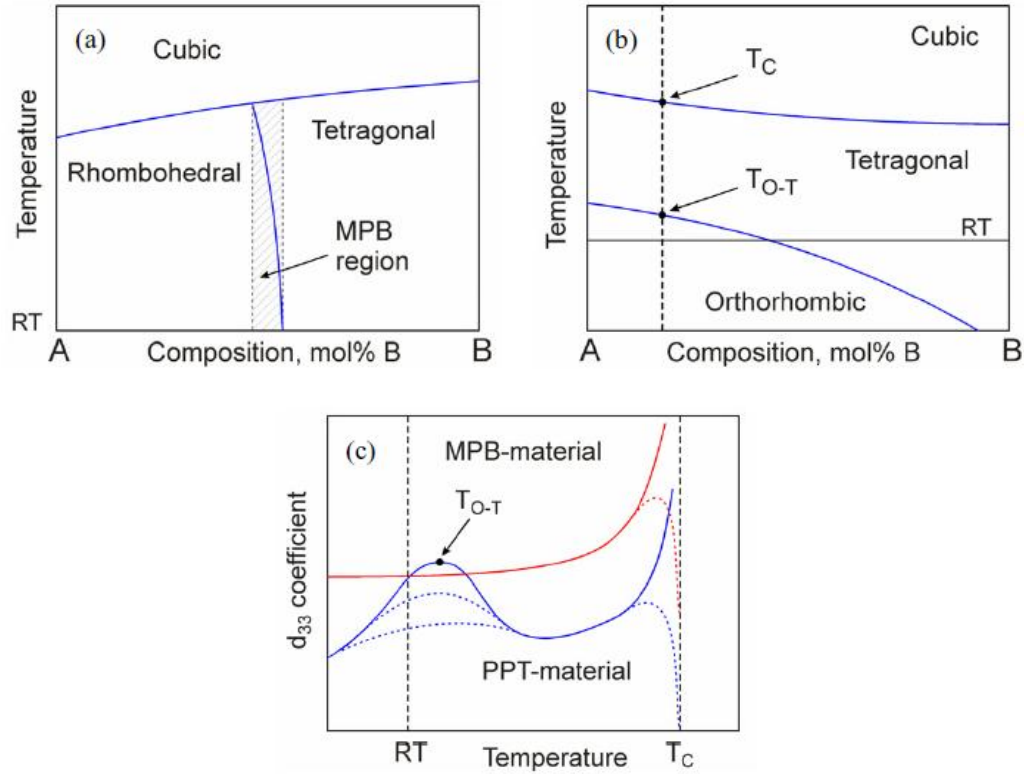


Fig. 1.9. Characteristic (hypothetical) phase diagrams for perovskite solid solutions exhibiting either a (a) morphotropic phase boundary (MPB) or (b) orthorhombic to tetragonal (O-T) polymorphic phase transformation (PPT). The resulting temperature dependence of the piezoelectric coefficient (c) for hypothetical MPB and PPT materials with the same room-temperature (RT) piezoelectric coefficient and same Curie temperature (T_c), where dotted trend lines indicate degradation of piezoelectric properties due to depolarization at temperatures near T_o-T and T_c . [46]

Recently, the depolarization temperature (T_d) has been proposed to describe the temperature at which a poled ferroelectric material completely or partially depolarizes, as determined from pyroelectric measurements [48]. This temperature typically coincides with the ferroelectric Curie temperature. However, in materials exhibiting one or more polymorphic phase transitions below the ferroelectric Curie temperature but above room temperature, T_d refers to the temperature of the lowest of these phase transitions. In contrast to compositional engineering approaches, the ‘structurally engineered materials’ approach focuses on controlling the micro and/or nanoscale structure of a piezoelectric material. Significant enhancements of electromechanical properties have been achieved utilizing various structurally engineered

techniques including: templated grain growth [49, 50], optimized grain size [51], and domain engineering [52-54]. The resulting enhancement of piezoelectric properties using several structural engineering approaches is illustrated in Figure 1.10. The above methods have been applied to a wide variety of existing piezoelectric materials including: bulk and single crystal BaTiO_3 , PZT ceramics, and bulk and single crystal $\text{Pb}(\text{Mg,Nb})\text{TiO}_3$ - PbTiO_3 . These methods represent an important future path for engineering the high performance lead-free piezoelectrics.

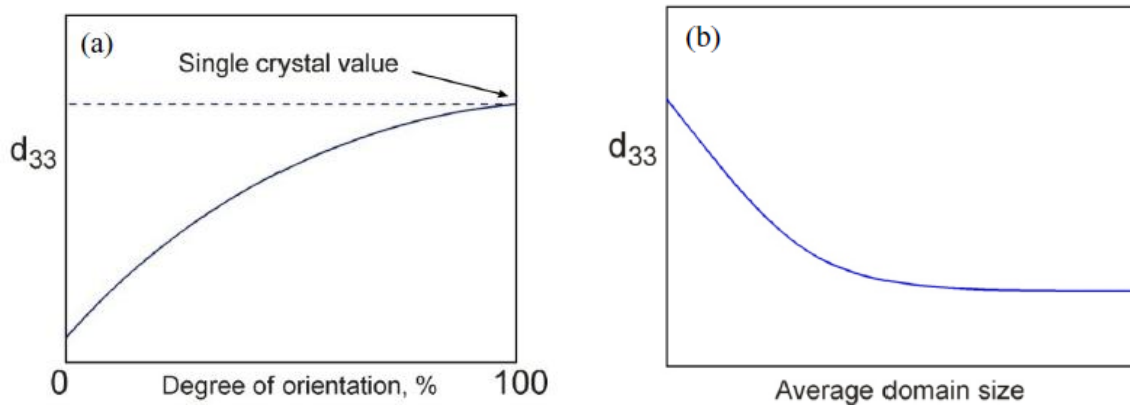


Fig. 1.10. Role of ‘engineered materials’ approaches to enhance piezoelectric properties (a) increasing texture fracture in template [46] grain grown ceramics leads to piezoelectric coefficients approaching the single crystal value, and (2) domain engineering to decrease domain size (enhance domain wall density) leading to increased piezoelectric coefficients.

Despite the many opportunities identified by structurally engineered materials the majority of the search for high performance lead-free piezoelectrics remains centered on brute force compositional investigations. The following review presents a survey of the classical literature on synthesis and optimization of lead free perovskite based piezoelectric ceramics, including some of the recent structural engineering approaches to achieve enhanced properties. Bulk piezoelectricity has been reported in many families of lead-free ceramic materials including: perovskite, tungsten bronze, and bismuth layer structured ferroelectrics as well as various grain oriented non-ferroelectric materials [55]. However, the relatively higher symmetry of prototype cubic perovskite structure generally leads to improved poling in randomly oriented

ferroelectric perovskites and subsequently higher piezoelectric coefficients compared to other lead free piezoceramic structures. The current review is organized into compositional families including: the titanate perovskite based materials (BaTiO_3 , $\text{Bi}_{1/2}\text{Na}_{1/2}\text{TiO}_3$, $\text{Bi}_{1/2}\text{K}_{1/2}\text{TiO}_3$) and solid solutions (section 1.2.4.1), the alkaline niobate perovskites (KNbCH , NaNbCh) and solid solutions (section 1.2.4.2) Finally, the status and promise of realizing viable lead-free piezoelectric ceramics for actuator applications is discussed by comparing reported piezoelectric coefficients and depolarization temperatures of both lead free, and lead based piezoelectric ceramics (section 1.2.4.3).

1.2.4.1 Titanate perovskites

Perovskite ferroelectrics in which the ferroelectric cation is the B-site Ti⁴⁺ ion make up a large fraction of the materials under consideration for lead-free piezoelectrics. Published piezoelectric coefficients and relevant phase transition temperatures for the titanate perovskites and their solid-solutions are summarized in Table 1.1.

Barium titanate:

Barium titanate BaTiO_3 is the prototype polymorphic phase transition (PPT) based high performance piezoceramic material. The discovery of the process for poling barium titanate led to development of the first polycrystalline piezoelectric ceramics [56, 57]. The piezoelectric coefficient d_{33} of pure BaTiO_3 fabricated by conventional solid state processing is around 190 pC/N [58]. Prior to the discovery of PZT based materials, BaTiO_3 was used in naval sonar applications and phonograph needles; however widespread commercial application of BaTiO_3 for piezoelectric actuators remains limited by its low Curie temperature ($T_c = 120^\circ\text{C}$) [47] which severely constrains the operational (or transient exposure) temperature for BaTiO_3 materials.

Recently, structural engineering approaches by several groups have led to significantly improved piezoelectric response in BaTiO₃. Introduction of fine-scale ferroelectric domains into barium titanate ceramics prepared from nano-scale particles and densified by microwave sintering results in a high d_{33} value of 350 pC/N [59-61]. In other work, a piezoelectric coefficient of 460 pC/N is achieved in high quality hydrothermally synthesized BaTiO₃ powders and an optimized conventional sintering process, resulting in fine grain ceramics, with grain sizes on order of 1-2 μm [62, 63]. A separate report also describes the tendency of the piezoelectric coefficient to increase with decreasing domain size [51]. This increased d_{33} , in small grain and small domain size randomly oriented ceramics, has also been combined with the templated grain growth technique and further enhancement in the piezoelectric coefficient reported. A d_{33} of 788 pC/N is reported in [64] grain oriented BaTiO₃ ceramics with submicron domain size[53]. These findings clearly demonstrate the large inherent piezoelectric response in BaTiO₃ (up to 460 pC/N) and that structural engineering approaches are a viable approach to realize significantly enhanced piezoelectric properties in lead-free piezoceramics (up to -800 pC/N in BaTiOs).

Bismuth potassium titanate:

Bismuth potassium titanate, Bi_{1/2}K_{1/2}TiO₃ (BKT) is another common lead-free ferroelectric ceramic material. Bi_{1/2}K_{1/2}TiO₃ was originally fabricated by Popper et al. [65] in 1957 and its ferroelectricity including Curie temperature of 370 °C was confirmed later by Buhrer[66]. At room temperature Bi_{1/2}K_{1/2}TiO₃ has the perovskite structure with tetragonal symmetry and exhibits a second phase transition to a pseudocubic structure at around 300 °C. Bi_{1/2}K_{1/2}TiO₃ ceramics are difficult to sinter [67], however, high densities of 97% of theoretical are achieved by hot pressing methods yielding piezoelectric d_{33} coefficients close to 70

pC/N[66]. Hot pressed $\text{Bi}_{1/2}\text{K}_{1/2}\text{TiO}_3$ shows increased T_c of 410-435 °C and the temperature of the second phase transition increases to 315-340 °C. Slightly improved piezoelectric properties in $\text{Bi}_{1/2}\text{K}_{1/2}\text{TiO}_3$ ceramics are obtained using an optimized poling procedure resulting in a d_{33} of 82 pC/N [68]. Alternatively, doping with bismuth and using sintering aids has further increased the d_{33} value to 100pC/N[69].

Bismuth sodium titanate:

Bismuth sodium titanate, $\text{Bi}_{1/2}\text{Na}_{1/2}\text{TiO}_3$ (BNT), first reported by Smoleskii et al. in 1960, is another important lead-free piezoelectric material [70]. $\text{Bi}_{1/2}\text{Na}_{1/2}\text{TiO}_3$ was found to be a perovskite-type ferroelectric at room temperature and exhibits relaxor ferroelectric behavior. A diffuse phase transformation in the temperature range 200 to 320 °C is observed in $\text{Bi}_{1/2}\text{Na}_{1/2}\text{TiO}_3$ corresponding to a transition from rhombohedral to tetragonal symmetry [71-74]. This transition is rather complex and it is believed it takes place through an intermediate orthorhombic antiferroelectric phase [75]. The preparation of dense $\text{Bi}_{1/2}\text{Na}_{1/2}\text{TiO}_3$ ceramics is difficult, requiring sintering temperatures above 1200 °C, which results in significant loss of bismuth. High leakage currents and high coercive field negatively impact the poling process and polarization saturation could not be achieved in conventionally fabricated $\text{Bi}_{1/2}\text{Na}_{1/2}\text{TiO}_3$ samples. However, dense ceramics have been obtained using excess Bi or hot press sintering methods, and saturated polarization loops were observed [76]. $\text{Bi}_{1/2}\text{Na}_{1/2}\text{TiO}_3$ ceramics fabricated by these latter techniques have piezoelectric d_{33} coefficients 94-98 pC/N and a depolarization temperature of 200 °C [70, 75, 76].

Table. 1.1. Room-temperature piezoelectric coefficients (d_{33}), depolarization temp. (T_d), and Curie temp. (T_C) for titanate perovskites. Notes: Measurement method is indicated when available: *Refers to a Berlincourt-type meter and # to the IEEE resonance method. Polymorphic phase transition occurring at T_d is indicated as follows: O–T, orthorhombic-tetragonal; PC, pseudocubic phase transformation; AFE, antiferroelectric phase transformation. Other abbreviations: BKT ($\text{Bi}_{1/2}\text{K}_{1/2}$) TiO_3 and BNT ($\text{Bi}_{1/2}\text{Na}_{1/2}$) TiO_3 .

Titanates and solid solutions				
Material	d_{33} (pC N ⁻¹)	T_{PPT} (°C)	T_C (°C)	Comment, reference
BaTiO ₃	190*	0	120	[7]
		O–T		
BaTiO ₃	350*	0	120	Microwave sintered
		O–T		[59]
BaTiO ₃	460*	24	126	Hydrothermal powders
		O–T		[63]
BaTiO ₃	788*	0	120	Textured
		O–T		[53]
BKT	70#	315	410	[139]
		PC		
BKT	82#	310	410	Hot-pressed
		PC		[68]
BKT–Bi	100#	280	391	[69]
BaTiO ₃ –BKT20 + Mn	76#	AFE	230	[55]
BaTiO ₃ –BKT5 + Mn	100#	none		
BNT–BaTiO ₃	155*	105	288	[83]
		AFE		
BNT–BaTiO ₃ + Li	208	85	260	[87]
		AFE		
BNT–BKT	150#	210	320	[91]
		PC		
BNT–BKT	144*	130	330	[92]
		PC		
BNT–BKT	157#	174	280	[93]
		PC		
BNT–BKT– BaTiO ₃	170*	162	262	[96]
		AFE		
BNT–BKT– BaTiO ₃	135#	197	290	[99]
		AFE		
BNT–BKT– BaTiO ₃ + Li	205*	210	N/A	[100]
		AFE		

Bismuth potassium titanate-barium titanate solid solution:

Both barium titanate (BaTiO_3) and bismuth potassium titanate ($\text{Bi}_{1/2}\text{K}_{1/2}\text{TiO}_3$) are tetragonal ferroelectric materials with Curie temperatures of 120 and 370 °C respectively. The binary system $(\text{Bi}_{1/2}\text{K}_{1/2})\text{TiO}_3$ - BaTiO_3 (BKT-BT) has been investigated in order to obtain a compound with enhanced piezoelectric properties and higher T_c than pure BaTiO_3 . The solid solution $x(\text{Bi}_{1/2}\text{K}_{1/2})\text{TiO}_3$ -(1-x) BaTiO_3 is single phase ferroelectric perovskite over the complete compositional range and shows close to linear dependence of the Curie temperature on $(\text{Bi}_{1/2}\text{K}_{1/2})\text{TiO}_3$ concentration, as shown in Figure 1.11 [55].

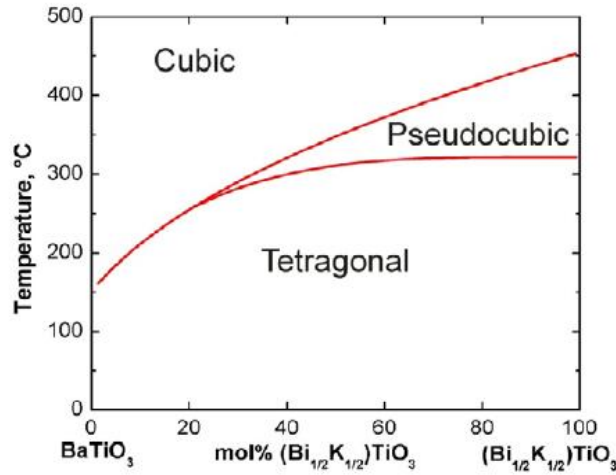


Fig. 1.11. Phase diagram of the $(\text{Bi}_{1/2}\text{K}_{1/2})\text{TiO}_3$ - BaTiO_3 solid solution. [55]

In compositions above $x = 60$ mol% $(\text{Bi}_{1/2}\text{K}_{1/2})\text{TiO}_3$ a second transition from tetragonal to an intermediate pseudocubic phase is observed at around 300°C and remains nearly independent of $(\text{Bi}_{1/2}\text{K}_{1/2})\text{TiO}_3$ concentration. Values of the piezoelectric d_{33} coefficient do not change significantly with composition and are in the range 60-70 pC/N. The highest d_{33} of 100 pC/N is obtained for $x=5$ mol% $(\text{Bi}_{1/2}\text{K}_{1/2})\text{TiO}_3$ with the addition of manganese, however this composition has a relatively low depolarization temperature (T_d) of 168 °C (likely associated

with the polymorphic phase transition from the tetragonal to pseudocubic phases). Compositions with $x > 60$ mol% $(\text{Bi}_{1/2}\text{K}_{1/2})\text{TiO}_3$ show good thermal stability of the coupling coefficient up to 250 °C and are considered attractive for piezoelectric applications even with their low d_{33} 's ~ 70 pC/N. Structural engineering in $(\text{Bi}_{1/2}\text{K}_{1/2})\text{TiO}_3$ - BaTiO_3 leads to a significantly improved d_{33} value of 121 pC/N, for $x = 10$ mol% $(\text{Bi}_{1/2}\text{K}_{1/2})\text{TiO}_3$ textured using the templated grain growth technique [77, 78].

Bismuth sodium titanate-barium titanate solid solution:

It might be expected that the solid solution of the rhombohedral ferroelectric bismuth sodium titanate $(\text{Bi}_{1/2}\text{Na}_{1/2})\text{TiO}_3$ and a tetragonal material such as barium titanate would exhibit a rhombohedral-tetragonal morphotropic phase boundary (MPB) as in the prototype PZT system. Subsequently this binary system $(\text{Bi}_{1/2}\text{Na}_{1/2})\text{TiO}_3$ - BaTiO_3 (BNT-BT) was investigated by Takenaka [79, 80] and the existence of an MBP confirmed at around 6-7 mol% BaTiO_3 , as illustrated in Figure 1.12. Enhanced dielectric constant, electromechanical coupling coefficient, and piezoelectric properties ($d_{33} = 125$ pC/N), compared to unmodified BNT ($d_{33} = 64$ pC/N), were observed at the MBP [81, 82]. Piezoelectric coefficients in the range 122-176 pC/N at the MPB have been reported by various researchers [83-86]; d_{33} values of 208 pC/N were achieved in lithium modified $(\text{Bi}_{1/2}\text{Na}_{1/2})\text{TiO}_3$ - BaTiO_3 [87, 88]. While the MPB composition for $(\text{Bi}_{1/2}\text{Na}_{1/2})\text{TiO}_3$ - BaTiO_3 has a relatively high T_c of 288 °C, a low depolarization temperature (T_d) of 150 °C has been reported. By analogy to the $(\text{Bi}_{1/2}\text{Na}_{1/2})\text{TiO}_3$ end member, the low T_d arises due to a polymorphic phase transformation to an antiferroelectric (AFE) phase, as substantiated by high temperature dielectric and polarization hysteresis measurements [79].

Bismuth sodium titanate-bismuth potassium titanate solid solution:

The solid solution of bismuth sodium titanate, $(\text{Bi}_{1/2}\text{Na}_{1/2})\text{TiO}_3$ (BNT), and bismuth potassium titanate, $(\text{Bi}_{1/2}\text{K}_{1/2})\text{TiO}_3$ (BKT), was synthesized by Elkechai et al. in 1996 [89] and an increase in the piezoelectric properties was observed in this system close to the rhombohedral to tetragonal morphotropic phase boundary, shown in Figure 1.13. The existence of an MPB between $(\text{Bi}_{1/2}\text{Na}_{1/2})\text{TiO}_3$ and $(\text{Bi}_{1/2}\text{K}_{1/2})\text{TiO}_3$ in the compositional range 16-20 mol% $(\text{Bi}_{1/2}\text{K}_{1/2})\text{TiO}_3$ was later substantiated by Sasaki et al.[90] based on structural studies indicating coexistence of rhombohedral and tetragonal phases as well as the corresponding compositionally dependant peaks in the dielectric, piezoelectric and electromechanical coefficients. More recent studies [55, 91-93, 94, 95] confirm high piezoelectric properties (d_{33} in the range 140-192 pC/N) at the MPB composition. The Curie temperature of the MPB ($T_c = 280\text{-}300\text{ }^\circ\text{C}$) is higher than that of pure $(\text{Bi}_{1/2}\text{Na}_{1/2})\text{TiO}_3$ as expected, however the depolarization temperature (due to a polymorphic phase transformation to the intermediate pseudocubic phase) is quite low reaching a minimum ($T_d = 140\text{ }^\circ\text{C}$) at the MPB.

Barium titanate-bismuth sodium titanate-bismuth potassium titanate ternary solid solution:

The ternary BaTiO_3 - $(\text{Bi}_{1/2}\text{Na}_{1/2})\text{TiO}_3$ - $(\text{Bi}_{1/2}\text{K}_{1/2})\text{TiO}_3$ (BT-BNT-BKT) solid solution (phase diagram, shown in Figure 1.14, has also been widely investigated due to relatively large Curie temperatures and high piezoelectric properties. BT-BNT-BKT exhibits a tetragonal-rhombohedral MPB and while maintaining piezoelectric properties similar to its end members. Reported values of the piezoelectric d_{33} coefficient are in the range 135-191 pC/N and are inversely proportional to the observed depolarization temperature, which is prohibitively low ($T_d \sim 110^\circ\text{C}$) at the MPB [96, 97, 98]. For compositions with a more reasonable depolarization

temperature ($T_d = 197\text{ }^{\circ}\text{C}$) a maximum d_{33} of 135 pC/N was obtained [99]. Further enhanced performance was found in Li-modified BT-BNT-BKT, exhibiting a d_{33} of 205 pC/N, with a depolarization temperature $T_d = 210\text{ }^{\circ}\text{C}$ [100].

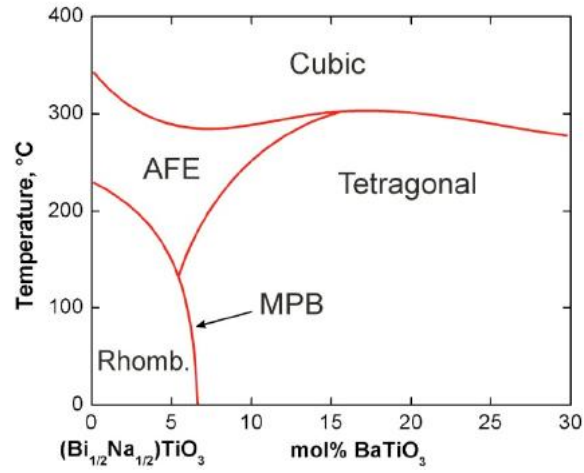


Fig. 1.12. Phase diagram of the $(\text{Bi}_{1/2}\text{Na}_{1/2})\text{TiO}_3$ - BaTiO_3 solid solution. [79]

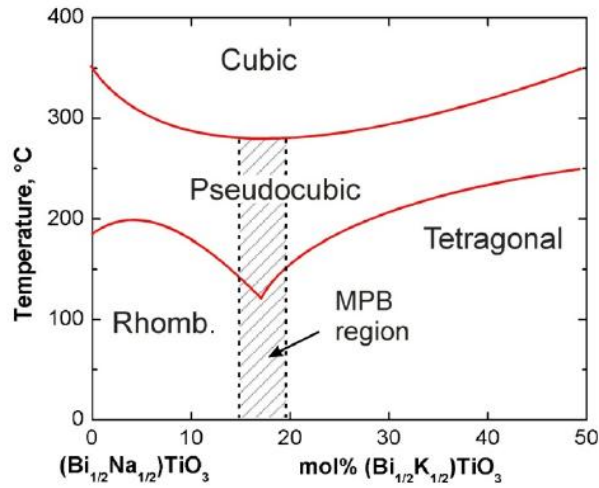


Fig. 1.13. Phase diagram of the $(\text{Bi}_{1/2}\text{Na}_{1/2})\text{TiO}_3$ - $(\text{Bi}_{1/2}\text{K}_{1/2})\text{TiO}_3$ solid solution. [55, 89, 93]

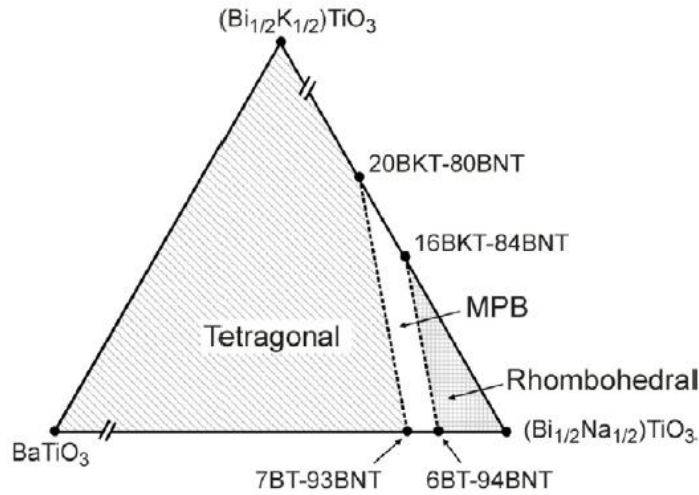


Fig. 1.14. Ternary phase diagram for the BaTiO_3 - $(\text{Bi}_{1/2}\text{Na}_{1/2})\text{TiO}_3$ - $(\text{Bi}_{1/2}\text{K}_{1/2})\text{TiO}_3$ solid solution. [98, 99]

1.2.4.2 Alkaline niobates

The alkaline niobates and their solid solutions are another interesting family of lead free perovskites. Significant recent experimental efforts in these materials have been undertaken largely following Saito et al's 2004 Nature paper and the accompanying editorial "Lead Free at Last"[101, 102]. While exhibiting high piezoelectric coefficients, particularly in structurally engineered ceramics these materials are still limited in application by low depolarization temperatures arising from an orthorhombic to tetragonal (O-T) PPT near room temperature. Published room temperature piezoelectric coefficients and phase transformation temperatures for the alkaline niobates and solid solutions are compiled in Table 1.2.

Potassium niobate:

In 1951, Matthias [103] discovered ferroelectricity in KNbO_3 reporting both its Curie temperature ($T_c = 435^\circ\text{C}$) and a second transition temperature at around 225°C . Further investigations revealed a sequence of phase transformations similar to those observed in BaTiO_3 (rhombohedral-orthorhombic-tetragonal-cubic) occurring at -10 , 220 , and 420°C respectively

[104]. Pure KNbO_3 ceramics are difficult to fabricate [47], however single crystals have been produced and interesting non-linear electro optic properties and piezoelectric coefficients along certain crystallographic directions have been reported [105-107]. High coupling coefficients ($k_x = 0.69$) and excellent temperature stability up to 160 °C make KNbO_3 single crystals attractive for ultrasonic and acoustic wave transducer applications, however, other uses of KNbO_3 's piezoelectric properties are limited [108]. Recent studies on bulk KNbO_3 ceramics report piezoelectric properties with a d_{33} coefficient of 97 pC/N [109] and large shear-mode d_{15} constant of 207pC/N [110, 111].

Sodium niobate:

The other alkaline niobate end member, Sodium niobate NaNbO_3 , is also an orthorhombic perovskite at room temperature transforming into the tetragonal phase at 370 °C and eventually to cubic above 640 °C [112]. At room temperature NaNbO_3 is antiferroelectric and as such exhibits no piezoelectric activity in its pure form [7].

Potassium niobate-sodium niobate solid solution:

The potassium niobate-sodium niobate, $\text{KNbO}_3\text{-NaNbO}_3$ (alternatively $(\text{K,Na})\text{NbO}_3$ or KNN) solid solution is widely considered as one of the most promising lead-free alternatives to the conventional piezoelectric ceramics. Both end members of the solid solution are orthorhombic at room temperature and early work on the ceramics in this system indicated multiple temperature induced phase transformations and morphotropic phase boundaries comprising a rather complex phase diagram, shown in Figure 1.15 [113, 114]. Piezoelectric d_{33} coefficients for KNN are reported in the range 80-160 pC/N and enhanced electromechanical properties observed near the 53 mol% sodium niobate composition [104, 64, 115, 116].

Processing of KNN ceramics is problematic due to the low sintering temperatures required because of the instability of the KNN phase above 1140 °C and volatility of the alkali species at high temperatures. This low temperature requirement makes it difficult to obtain ceramics of high sintered density [7, 116]. However, reasonable piezoelectric properties ($d_{33} = 100$ pC/N) of KNN have been achieved by optimizing the conventional sintering process [116]. The incorporation of liquid phase sintering aids ($K_4CuNb_8O_{23}$, $K_{5.4}CuTa_{10}O_{29}$, CuO)[117-119] can result in densities up to 97.5% theoretical. Liquid phase sintering has reduced sintering temperatures to as low as 950 °C, and high-field d_{33} of 180-270 pC/N have been reported. Densification of KNN ceramics is also significantly improved by hot-pressing, with sintered ceramics reaching ~99% of the theoretical density and the resulting piezoelectric constant nearly twice the value of conventionally sintered KNN [120-122]. Spark plasma sintering has also resulted in high density KNN ceramics and with enhanced piezoelectric coefficients ($d_{33} = 148$ pC/N) [123-125]. Numerous compositional engineering approaches have also been explored to optimize the piezoelectric properties of KNN materials. However, nearly all of these approaches achieve "enhanced" properties by shifting the orthorhombic-tetragonal (O-T) PPT temperature to slightly above or below room temperature. As discussed above and illustrated in Figure 9, this close proximity to a PPT results in significant softening of the piezoelectric properties (large d_{33}) however comes at the cost of large temperature dependence of the piezoelectric response and poor stability of the poled domain state in most modified KNN compositions. Compositional engineered KNN systems modified by $LiTaO_3$ and $LiSbO_3$ have been studied the most intensively. KNN in combination with tetragonal $LiTaO_3$ exhibits a morphotropic phase boundary between orthorhombic and tetragonal phases at 4-5 mol% of $LiTaO_3$ accompanied by enhancement of piezoelectric properties; d_{33} coefficients have been reported in the range 200-

259 pC/N [126, 127, 128-130]. The addition of LiSbO_3 to pure KNN shifts the orthorhombic to tetragonal polymorphic phase transition temperature down from 200 °C to nearly room temperature ($T_{\text{OT}} \sim 35$ °C) and increases the RT d_{33} coefficient; reaching a maximum ($d_{33} = 250\text{-}265$ pC/N) at approximately 5 mol% of LiSbO_3 content [131-133]. In the work of Saito et al. [101], optimization of the KNN by separate lithium, tantalum, and antimony additions (specifically $(\text{K}_{0.44}\text{Na}_{0.52}\text{Li}_{0.04})(\text{Nb}_{0.86}\text{Ta}_{0.10}\text{Sb}_{0.04})\text{O}_3$, the so-called LF4 composition) yielded a further increase of d_{33} to 300 pC/N. In the same work, the properties of the LF4 composition were further enhanced by the reactive template grain growth method produced d_{33} values as high as 416 pC/N in $\langle 001 \rangle$ oriented ceramics (LF4T) [101]. The observed enhancement of the piezoelectric coefficient was at first attributed to an MBP between orthorhombic and tetragonal phases. However, the authors themselves and more recent studies observed temperature dependence of the electromechanical properties near the room temperature and the existence of the orthorhombic-tetragonal PPT near room temperature in both the LF4 and LF4T compositions [101, 134]. Recently, an alternative modification of the KNN system has been proposed [135, 136]. In this work it is shown that the orthorhombic to tetragonal phase transition temperature in KNN can be effectively lowered by addition of CaTiO_3 . The authors show that orthorhombic to tetragonal transition temperature can be reduced 1 wt% CaTiO_3 addition to below room temperature. This results in improved thermal stability and reduced temperature dependence of the piezoelectric response in the range -50 to 200 °C while maintaining acceptable piezoelectric properties $d_{33} = 210$ pC/N [135, 136].

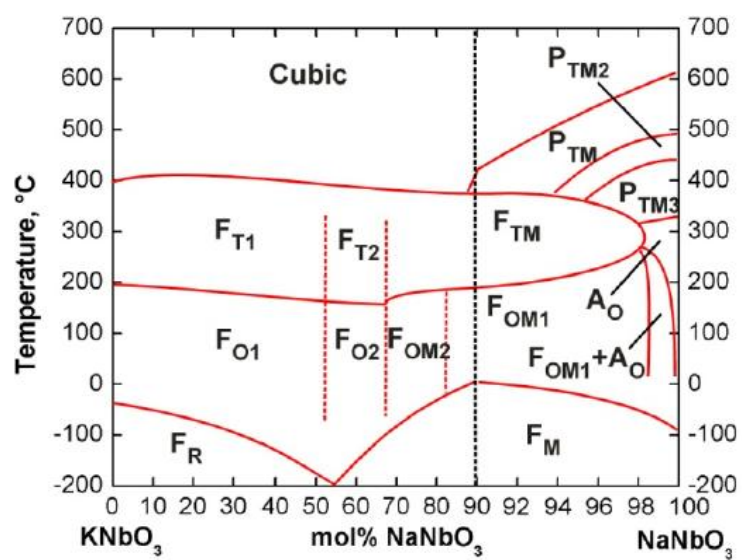


Fig. 1.15. Phase diagram of the KNbO_3 - NaNbO_3 solid solution [35].

Table. 1.2. Room-temperature piezoelectric coefficients (d_{33}), depolarization temp. (T_d) and Curie temp. (T_c) for alkaline niobate perovskites. For all cases the T_d is associated with an orthorhombic–tetragonal PPT (O–T). Notes: When available the measurement method used for determining the piezoelectric coefficient is indicated: * refers to a Berlincourt-type meter and # to the IEEE resonance method. O–T: orthorhombic–tetragonal.

Alkaline niobates				
Material	d_{33} (pC N ⁻¹)	T_{PPT} (°C)	T_C (°C)	Comment, reference
KNbO ₃	97	220 O–T	435	[69]
(K,Na)NbO ₃	80	195 O–T	420	[64]
(K,Na)NbO ₃	127	195 O–T	420	Hot pressed [120]
(K,Na)NbO ₃ + Sb	218*	160 O–T	352	Textured [140]
(K,Na)NbO ₃ + Ag	186*	170 O–T	355	[141]
(K,Na)NbO ₃ + Li	240*	20 O–T	460	[142]
(K,Na)NbO ₃ + Li,Ta	190*	50 O–T	310	[142]
(K,Na)NbO ₃ + Li,Ta	230*	50 O–T	323	[126]
(K,Na)NbO ₃ + Li,Ta	262*	35 O–T	325	[143]
(K,Na)NbO ₃ + SrTiO ₃	200*	27 O–T	277	[144]
(K,Na)NbO ₃ + LiTaO ₃	200*	55 O–T	430	[127]
(K,Na)NbO ₃ + LiNbO ₃	235*	70 O–T	452	[145]
(K,Na)NbO ₃ + LiSbO ₃	265#	35 O–T	368	[131]
(K,Na)NbO ₃ + Li,Sr,Sb	142*	115 O–T	353	[146]
(K,Na)NbO ₃ + Li,Sb,Ta	400*	20 O–T	230	[147]
(K,Na)NbO ₃ + Li,Sb,Ta(LF4)	300*	25 O–T	253	[101,134]
(K,Na)NbO ₃ + Li,Sb,Ta(LF4T)	416*	25 O–T	253	Textured [101,134]
(K,Na)NbO ₃ + LiSbO ₃ + CaTiO ₃	210*	–43 O–T	296	[135]
(K,Na)NbO ₃ + Li,Sb,Ta	370*	25 O–T	270	O ₂ sintering [148]
(K,Na)NbO ₃ + Sb,LiTaO ₃	321*	50 O–T	315	[149]
(K,Na)NbO ₃ + Li,Ag	220*	50 O–T	476	[150]
(K,Na)NbO ₃ + AgSbO ₃	192*	145 O–T	348	[151]

1.2.4.3 Discussion and continued developments in lead-free piezoceramics

The above review clearly identifies many significant recent advances in the search for lead-free materials for piezoceramic actuator applications. However, it can be difficult to appreciate the significant limitations associated with the vast majority of these materials. Zhang et al have proposed the use graphs of d_{33} over T_d (where T_d is the depolarization temperature corresponding to the lowest transition temperature, either T_c or TPPT) in order to make more reliable comparisons both among and between lead based and lead-free piezoelectrics materials [6, 137, 138]. Such plots provide a concise illustration of the relationship between the room temperature piezoelectric coefficient and phase transition temperatures. They also provide an indication of the temperature dependence and maximum usage temperatures of the various piezoelectric materials and families of materials.

Following this convention, the properties of the lead-free materials summarized in this work are reported in Figure 1.16. Reviewing this graph several general trends are readily identified. First, within a given compositional family the room temperature d_{33} coefficients increase as the T_d decreases. (The inherent consequences of reduced T_d are increased temperature dependence of d_{33} and reduced maximum usage temperature.) Second, the majority of the alkaline niobates (triangles) have depolarization temperatures below 100 °C (associated with the OT PPT) which is generally too low for these materials to be of broad commercial interest (as was the case for pure BT). Third, the titanates in general have both moderate d_{33} values (100-200 pC/N) and moderate depolarization temperature (100-300 °C). Finally, the lead based materials still maintain a clear performance advantage, universally possessing the highest d_{33} coefficients while maintaining Curie temperatures >200 °C.

In addition to the above general trends, this graph also suggests possible paths for future development. The vertically stacked circles at 110 °C represent the effect of various structural engineering approaches in pure BT ceramics. While the T_c of BT ceramics is still too low for these materials to be of broad interest, textured-domain engineered BT is the current "hero" piezoceramic with a $d_{33} \sim 800$ pC/N. Additionally, the top two triangles at -25°C also illustrated the effect of structural engineering, these are textured KNN materials processing nearly two fold enhancement of the d_{33} coefficient over randomly oriented ceramics of the same composition. On the basis of these strong enhancements observed in "structurally engineered" piezoceramics it is suggested that more effort should be focused understanding these effects and in applying them to existing materials rather the continued brute force compositional investigations.

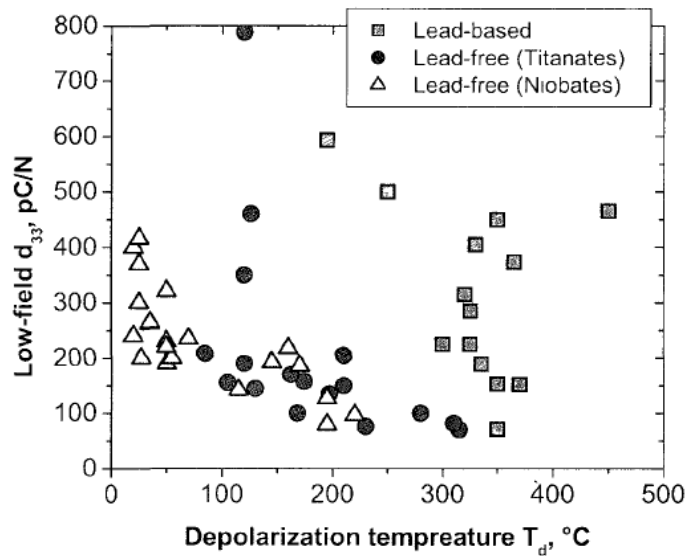


Fig. 1.16. Piezoelectric coefficient over depolarization temperature for the various families of lead-free and including lead based piezoelectric ceramics.

1.3 Multifunctional Composites

As mentioned before, multifunctional materials are integrated material systems that carry external mechanical loading while serving multiple integrated functionalities such as energy absorption, thermal management, sensing, power generation, vibration control, etc. Over the last decades the advancement in this field has been rapid due to the excellent performance benefits and safety achieved by multifunctional materials. To present day, the development in such composites has incorporated additional functionalities such as self healing, energy storage, and self-sensing and actuation. The following sections will discuss some of these developments and applications for these multifunctional composites.

(Following sections are based on the review of R.F. Gibson [152]: "A review of recent research on mechanics of multifunctional composite materials and structures". Composite Structures, 2010 92 p. 2793-2810)

1.3.1 Electrical and/or thermal conductivity

One important application of polymer composites is in aircraft structures, where electrical conductivity is required since non-conducting structures may be damaged by lightning strikes. Here, conductive polymer nanocomposites are being investigated as possible replacements for non-conducting polymer matrix materials. This would eliminate the need for add-on metallic conductors, which are too heavy and may be difficult to repair [155]. The added functionality of enhanced thermal conductivity in composites is important for cooling of electronic circuits and propulsion systems. In polymers, a small concentration of carbon nanotubes (CNT) or other conducting nanoreinforcements can lead to large improvements in the electrical conductivity of the nanocomposite. For example, Fig. 1.17 shows that the electrical conductivity of CNT/epoxy

nanocomposites increases by nearly 6 decades when the CNT concentration is increased by only 2 decades [153]. The carbon nanotube concentration in the polymer which marks the transition between insulator and conductor is called percolation threshold, which in the example given in Figure 1.18 is only 0.04 wt%. Sandler et al. [160] reported percolation thresholds as low as 0.0025 wt% for aligned MWNT/epoxy nanocomposites. The percolation threshold in polymer matrix materials is so low because of the extremely high aspect ratios of CNTs which make it relatively easy to create a conducting path along the CNTs in the insulating polymer matrix. Fig. 18 from Li et al. [154] shows how the percolation threshold decreases with increasing CNT aspect ratio. It can be noted that to ensure low percolation thresholds it is important to develop processes that preserve high aspect ratio of CNTs.

Although the thermal conductivity of CNT/polymer nanocomposites increases with the increasing CNT concentration, the increase is gradual and there is no sharp insulator–conductor transition or percolation threshold as in electrical conductivity [162]. According to Shenogina et al. [162], the difference lies in the conductivity ratio k_f/k_m . For thermal transport, even for very conductive, high aspect ratio CNTs, k_f/k_m is only about 10^4 , while for electrical transport, k_f/k_m can be as much as 10^{12} – 10^{16} . Therefore, electrical transport is dominated by percolating CNT threshold, whereas thermal transport is strongly influenced by the polymer matrix. But even with the lack of percolation threshold, small amounts of CNTs in CNT/polymer composites can lead to disproportional increases in thermal conductivity. Biercuk et al. [163] found that 1 wt% SWNTs in epoxy resulted in a 125% increase in thermal conductivity at room temperature, while Bonnet et al. [164] measured a 55% increase in thermal conductivity for a 7 wt% SWNT/PMMA composite, and Kim et al. [165] reported a 57% increase in thermal conductivity by adding 7 wt% MWNTs in phenolic resin. However, since higher filler loadings are required to create

significant improvements in thermal conductivity of polymers, this may lead to processing issues. For example, Ganguli et al. [166] achieved a 28-fold increase in thermal conductivity of epoxy by adding 20 wt.% chemically functionalized and exfoliated graphite flakes, but graphite loading levels greater than 4 wt.% were found to increase the viscosity of the mixture beyond the desirable processing window for the vacuum-assisted-resin-transfer molding (VARTM) process. Meantime, only small amounts of CNTs are needed to produce acceptable thermal conductivity in some applications. Sihn et al. [167] found that the through-thickness thermal conductivity of epoxy adhesive joints can be increased by several orders of magnitude when aligned MWNT “nanograss” is incorporated in the epoxy adhesive (Fig. 1.19).

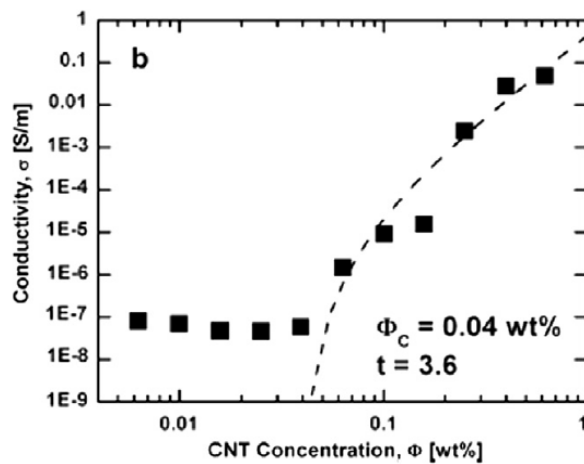


Fig. 1.17. Electrical conductivity of CNT/epoxy nanocomposites at various CNT concentrations. Percolation threshold is 0.04 wt.%. Copyright Elsevier. [153]

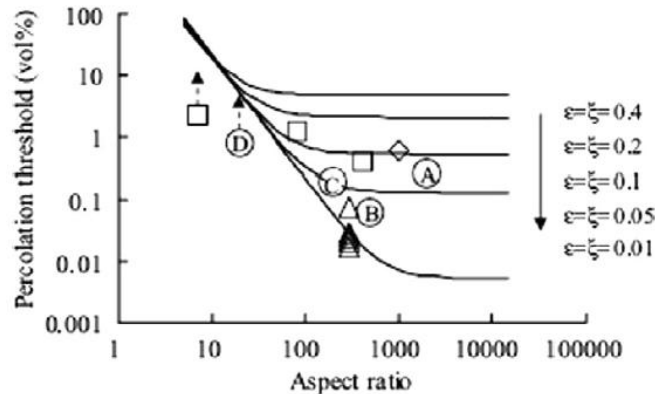


Fig. 1.18. Effect of CNT aspect ratio on percolation threshold for CNT nanocomposites with varying dispersion states. Copyright Wiley-VCH verlag GmbH & Co. KGaA. [154]

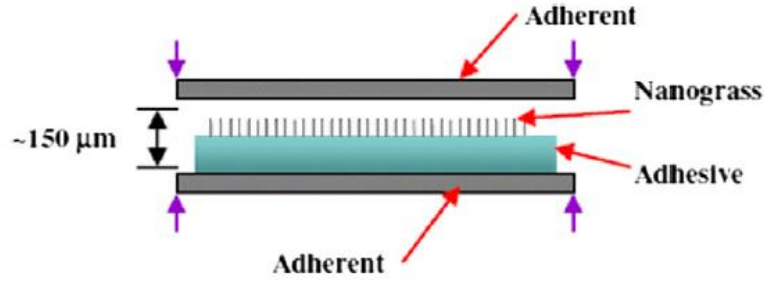


Fig. 1.19. Nanograss-enhanced polymer adhesive joint for improved through-thickness thermal conductivity. [167]

1.3.2 Sensing and actuation

Sensing and actuation are two closely related functions, and in many cases, they can be performed by the same material, as well as for other functions like energy harvesting/storage and structural health monitoring. Several recent review articles have already covered much of the recent research related to sensors and actuators that can be used in multifunctional structures. For example, Li et al. [168] and Gibson et al. [169] have reviewed recent research related to sensors and actuators based on carbon nanotubes and their composites. A review article by Ratna and Karger-Kocsis [170] covers recent research on shape memory polymers which have potential applications as sensors and/or actuators. Piezoelectric materials such as lead zirconate titanate (PZT), polyvinylidene fluoride (PVDF) and aluminum nitride (AlN) can be embedded in structures for sensing and actuation, as they naturally possess the required electromechanical coupling. The effectiveness with which a piezoelectric material converts applied mechanical energy to electrical energy (i.e., for sensing or energy harvesting) is characterized by the piezoelectric coupling coefficient [171].

The most widely used forms of piezoelectric materials are wafers [172] and thin films [173], and numerous publications have dealt with them over many years. Piezoelectric microelectromechanical systems (MEMS) for sensing and actuation have been the subject of

extensive research, and the state-of-the-art in this area has been very recently reviewed by Tadigadapa and Mateti [174]. So in order to avoid duplication, we focus here on other important recent developments in structurally integrated sensing and actuation in load-bearing multifunctional composite structures. Although not as common as piezoelectric wafers or thin films, piezoelectric fibers have been investigated as possible active components of multifunctional fiber-reinforced composites. The earliest reports of piezoelectric fiber composites (PFC) were apparently published by Hagood and Bent [175] and Bent et al. [176], who embedded micron sized piezoelectric fibers in an epoxy matrix to which PZT powder had been added to reduce the fiber/matrix dielectric mismatch. The PFC laminate was built up from PFC laminae embedded between conventional graphite/epoxy laminae and interlaminar electrodes which applied the electric field required for actuation. Good agreement was obtained between measured electrically-induced deformations and those predicted by a modified Classical Lamination Theory which included actuator-induced stress terms [176]. More recently developed hollow piezoelectric fibers [177,178] offer the advantage of lower operating voltage and a broader choice of possible matrix materials compared with solid cross-section piezoelectric fibers. Brei and Cannon [178] investigated the hollow piezoelectric fiber concept in Fig. 1.20, with emphasis on the effects of three key design parameters (matrix/fiber Young's modulus ratio, aspect ratio of the individual fibers, and overall active composite volume fraction) on the performance, manufacturing and reliability of the active composites. In Fig. 1.20, in the actuation mode, radial poling of the piezoelectric fiber results in longitudinal deformation of the fiber, while in the sensing mode, longitudinal deformation results in radial electrical output.

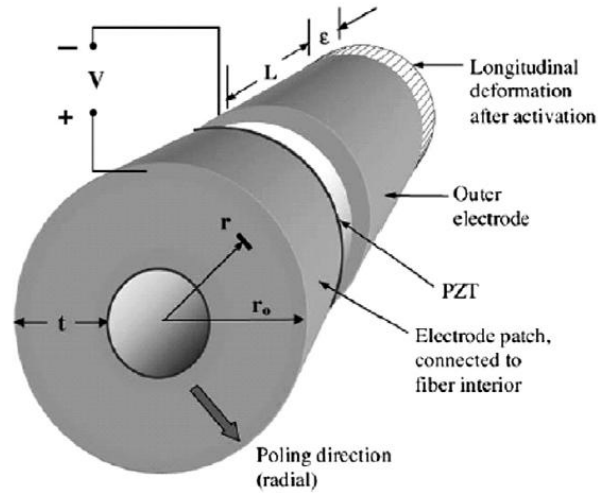


Fig. 1.20. Hollow piezoelectric fiber with radial poling and longitudinal actuation of the fiber. [178]

The capability of simultaneous control of stiffness and damping is a significant advantage of a new class of materials known as magnetorheological elastomers (MRE), which consist of conventional elastomers filled with micron-sized magnetizable particles such as iron. As reported by Fuchs et al. [179], an applied magnetic field of variable strength was used to continuously and rapidly control stiffness and damping of a polybutadiene elastomer filled with 3–7 μm diameter carbonyl iron particles. In this case, the optimum concentration of the iron particles for greatest improvement of damping and stiffness was found to be 60 wt%, and other important variables which govern the stiffness and damping of MREs are the alignment of the magnetic particles and the temperature.

As indicated earlier, several recent review articles have dealt with the general area of structural health monitoring [180–183]. Here we will focus specifically on the use of embedded piezoelectric sensor/actuator networks for damage detection in composite structures due to its importance in the development of multifunctional structures. Lin and Chang [184] described the fabrication and initial validation testing of the Stanford-Multi-Actuator-Receiver-Transduction (SMART) Layer concept (Fig. 1.21).

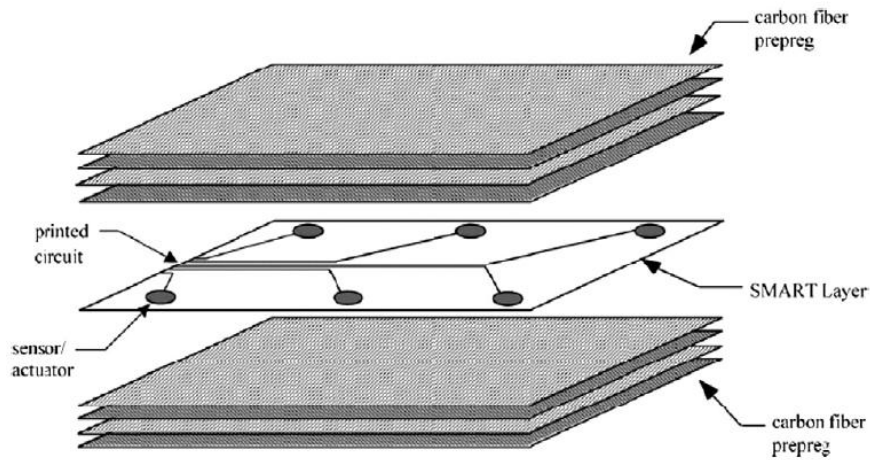


Fig. 1.21. Stanford-Multi-Actuator-Receiver-Transduction (SMART) layer concept of integrated sensor/actuator network in a composite laminate. [184]

This concept involves the use of printed circuit technology to produce a thin flexible, dielectric film with an array of networked piezoceramic actuators/sensors, which is embedded within a conventional composite laminate. It was shown that a conventional autoclave process and cure cycle can be used to fabricate carbon/epoxy composite laminates containing the SMART Layer, that the layer does not significantly degrade the mechanical behavior of the composite, and that by measuring the phase delay between the transmitted and received stress wave during the cure process, the state of cure can be monitored. Subsequent research [185] showed that such layers can be integrated into composite structures fabricated by RTM and filament winding processes, and that the concept can be applied to either active or passive sensing to monitor the health of the structure throughout its lifetime. Still more recently, Wu et al. [186] demonstrated the feasibility of an improved actuator/ sensor network for damage detection in composite laminates based on the use of PZT actuators and fiber Bragg grating (FBG) fiber optic sensors instead of using PZTs for both actuating and sensing. The advantage of this approach lies in the decoupling of the signal transmission mechanisms and elimination of the signal crosstalk between actuator and sensor signals in the PZT actuator/ sensor network. Other

approaches to active sensor networks for damage detection in composite structures have been reported by Su et al. [187,188]. Reports on the use of artificial neural networks to analyze the data from the piezoelectric sensor networks and classify and locate the damage in composite structures have been published by Watkins et al. [189], Haywood et al. [190], and Yu et al. [191]. Similar systems have been adapted for control of smart laminated structures by Srivastava et al. [192]. Layer-by-layer (LbL) assembly, which involves sequential deposition of dissimilar thin films at the nanoscale, has made it possible to develop sensors that are capable of detecting multiple phenomena. For example, Loh et al. [193] used the LbL method to fabricate a carbon nanotube-polyelectrolyte multilayer composite material for monitoring strain and corrosion. In this case, the concentration of carbon nanotubes determines the sensitivity to strain and the type of polyelectrolyte determines the sensitivity to pH. Deposition of such a LbL sensor on a miniature planar coil antenna results in a passive wireless sensor which does not require a battery power supply [194]. The LbL method can also be used to fabricate high strength multifunctional composites for biological implants, anticorrosion coatings, and thermal/electrical interface materials [195,196]. Shape memory polymers also have great potential for use in sensors and actuators. This is particularly true for electroactive shape memory polymer composites containing conductive fillers [170].

1.3.3 Energy storage/harvesting

The basic idea behind energy harvesting/storage as related to multifunctional structures is to parasitically extract energy from the motion and/or deformation of a host structure and convert it to electrical energy which can be stored and used for other purposes. One popular application is to power small electronic devices such as wireless sensors for structural health monitoring. Several review articles have already been published on this subject [183, 197–199], and since the

discussion of sensors and actuators in the previous section is also highly relevant to energy harvesting, the emphasis in this section will be on recent developments in energy storage in load-bearing multifunctional structures. The most common mode of energy harvesting involves the use of piezoelectric materials to convert mechanical deformations from vibrating structures such as beams and plates to electrical energy. It appears that Sodano et al. [200] were the first to report that the power output from a randomly vibrating piezoelectric material is capable of recharging a discharged nickel metal hydride battery. They also reported on the use of the piezoelectric output to charge a capacitor, but concluded that the capacitor discharge occurred too quickly for practical energy storage and that batteries provided more flexibility in use of the stored energy.

In a multifunctional structure, the battery should become part of the load-bearing structure. Pereira et al. [201,202] embedded thin film lithium energy cells within carbon/epoxy laminates to form energy storage structural composites. The lithium energy cells did not significantly change the strength and stiffness of the carbon/epoxy laminate, and the energy cells charged and discharged normally when the composite was mechanically loaded to as high as 50% of its ultimate tensile strength. Further integration was achieved by Kim et al. [203], who used a copper nano-inkjet-printed circuit on a polymer film to interconnect a thin-film solar module and a thin-film lithium-ion battery. The resulting film was embedded and co-cured within carbon/epoxy prepreg layers to fabricate an energy harvesting/storage laminate. The multifunctional laminate was then subjected to mechanical loading. As shown in Fig. 1.22, when the ink-jet-printed electrodes are thicker than 4 μm , they did not exhibit any significant resistance change up to the maximum strain of 1%.

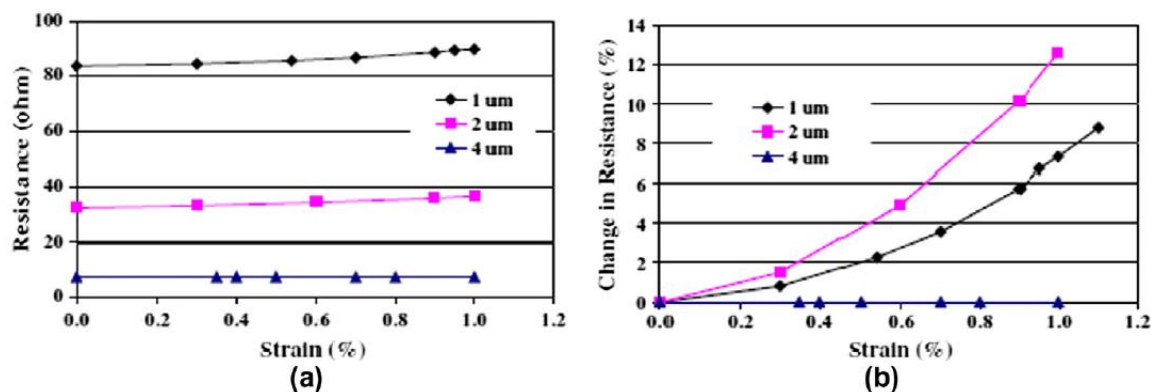


Fig. 1.22. Resistance of inkjet-printed 160 μm -wide electrode under static loading for several electrode thicknesses: (a) resistance and (b) percentage of resistance change. [203]

Liu et al. [204] developed a new load/bearing structural battery in which the polymer cathode in a conventional polymer lithium-ion battery (Fig. 1.23 (a)) was replaced by a higher molecular weight, carbon nanofiber-reinforced polymer (Fig. 1.23 (b)), the organic liquid electrolyte was replaced with a solid-state polymer electrolyte and the separator region was reinforced with nonconducting fibers. Although this design represents a starting point, the tensile modulus of the battery was only about 3 GPa, and the energy density was low compared with that of a conventional lithium-ion battery, so further work is needed to develop a usable structural battery.

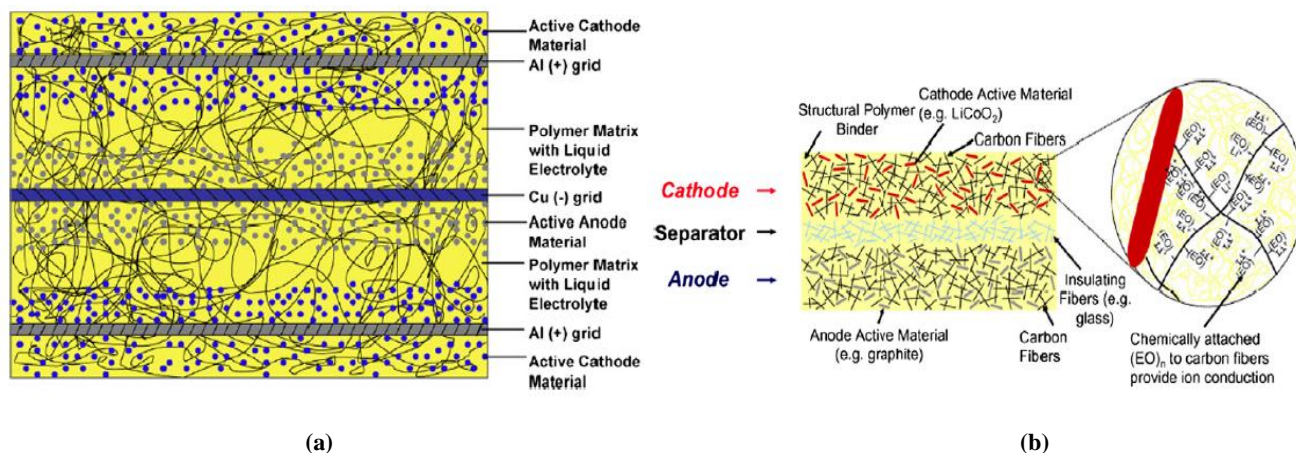


Fig. 1.23. Construction of (a) conventional non-structural polymer lithium-ion battery and (b) new structural battery [204]

Snyder et al. [205] investigated different polymer electrolyte formulations for multifunctional structural batteries ranging from highly conductive and structurally weak to poorly conductive and highly structural. It was found that the electrical conductivity and the elastic modulus of the different formulations are inversely related, which makes it difficult to optimize both properties. In a separate paper, Snyder et al. [206] investigated the properties of commercial carbon fabric materials, carbon nanotube papers and nanofoam papers for possible use as anodes in multifunctional lithium-ion batteries. IM-7 and T300 PAN-based carbon fabrics yielded the best balance between electrochemical and tensile strength performance, whereas the pitchbased fabrics exhibited poor multifunctional performance. The nanofoam papers had the best electrochemical performance but the mechanical properties were poor.

Although structural integrated batteries are more practical for slower discharge over a longer period of time, structurally integrated capacitors can provide energy storage for quick discharge at high energy levels. O'Brien et al. [207] compared stiffness and energy density of various structural capacitors. As shown in Fig. 1.24, conventional capacitors have high energy density but poor stiffness, whereas structural composites have good stiffness but poor energy density. None of the materials evaluated met the design goal of multifunctional efficiency for system level weight savings shown by the dashed line in Fig. 1.24. In a continuation of this work, Baechle et al. [208] addressed design issues for improving multifunctional efficiency and scaling issues related to manufacturing. Luo and Chung [209] developed a high capacitance structural capacitor consisting of a carbon/epoxy laminate with a paper interlayer to reduce through-the-thickness conductivity, but the capacitor was not mechanically tested.

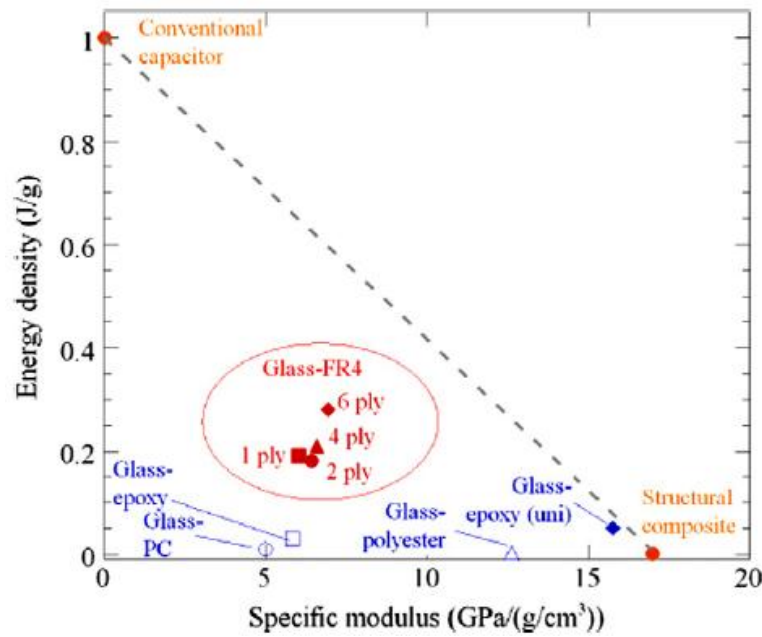


Fig. 1.24. Energy density and specific modulus of multifunctional structural capacitors. Dashed line represents design goal for true multifunctionality. [207]

1.3.4 Self-healing capability

A truly autonomous multifunctional structure will be capable of healing itself when damaged, as a biological system would, and recent research has demonstrated the feasibility of such materials, particularly polymeric materials. A comprehensive review of publications in the area of self-healing polymeric materials has recently appeared [182], so only a few representative publications will be discussed here. White et al. [210] developed self-healing polymers and polymer composites based on the use of a microencapsulated healing agent and a catalyst for polymerizing the healing agent. As shown in Fig. 1.25, when damage causes cracks in the polymer, the cracks break open the microcapsules, causing the healing agent to leak into the crack by capillary action. The healing agent then reacts with the catalyst, causing polymerization that bonds the crack faces together. Mode I fracture toughness tests of virgin epoxy and self-healed epoxy specimens using the tapered double cantilever beam (TDCB) test in Fig. 1.25

showed that fracture load and corresponding fracture toughness for the self-healed specimens reached up to 75% of the corresponding values for the virgin uncracked specimens.

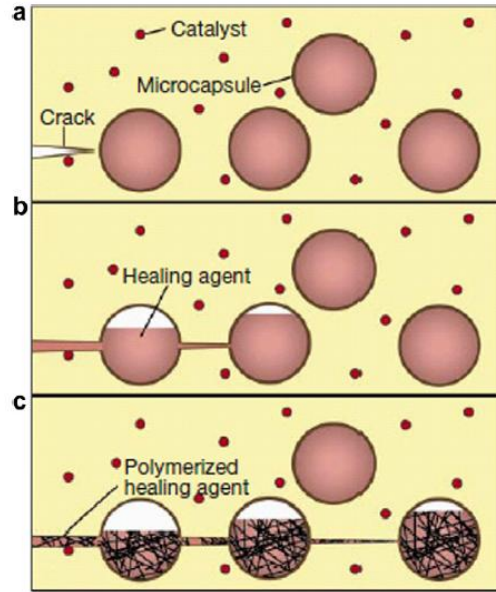


Fig. 1.25. Illustration of self-healing of cracks in polymers by the use of a microencapsulated healing agent and a catalyst for polymerizing the healing agent. [96]

Further research on optimization of the microcapsule concentration and choice of catalyst led to crack healing efficiencies of over 90% ($g = 0.9$) in self-healed specimens and maximum healing efficiency was achieved within 10 h of the fracture event [211]. Still more recently, Caruso et al. [212] obtained complete recovery of virgin fracture toughness ($g = 1$) by replacing the original solvent healing agent in the microcapsules with epoxy–solvent microcapsules containing a mixture of epoxy monomer and solvent. As shown in Fig. 1.26b, the resulting load–displacement curves indicate full recovery of virgin fracture toughness. Related research by the same group has considered self-healing polymers under fatigue loading [213–215] and low-velocity impact loading [216], as well as the development of self-healing polymer coatings to provide effective corrosion protection for steel substrates [217], and the use of three-dimensional

microvascular networks in the substrate beneath an epoxy coating to enable continuous delivery of healing agents for self-healing of repeated crack damage in the coating [218].

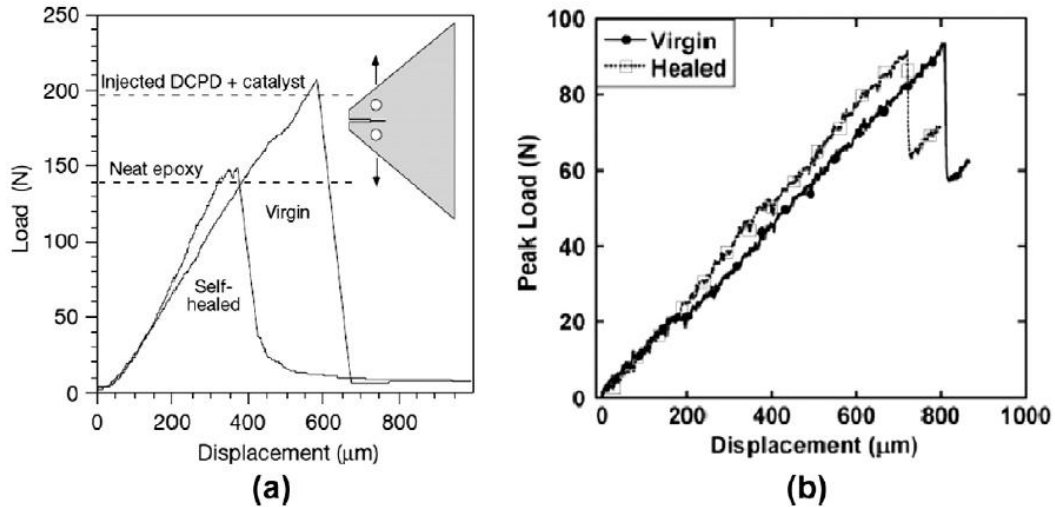


Fig. 1.26. Illustration of self-healing of cracks in polymers by the use of a microencapsulated healing agent and a catalyst for polymerizing the healing agent. [211]

Other recent developments in self-healing polymer composites include the use of different methods of healing agent microencapsulation such as nanoporous silica capsules [219] and nanoporous glass fibers [220]. The use of self-healing polymers as the matrix material in carbon fiber-reinforced composites has also been considered by Williams et al. [221]. Yin et al. [222] found that the self-healing ability of woven glass fabric/epoxy composites containing healant microcapsules degraded with storage time. The likely cause is believed to be time-dependent diffusion of the epoxy monomer from the microcapsules following contraction of the microcapsules during the cure process. This degradation was found to be a self-limiting process as the leaked epoxy gradually cured and blocked the diffusion sites on the microcapsules, but it was concluded that further research is needed to improve the microcapsule designs and materials.

1.4 Piezoelectric Fiber Composites

However many advantages monolithic piezoceramic materials may offer, there are several practical limitations to implementing them in real-life applications. Their brittle nature makes them vulnerable to breakage during bonding and handling procedures, as well as making their application to conform to curved surfaces very hard to achieve. This is why the idea of piezoelectric fiber composites (PFC), which consist of embedding piezoceramic fibers into a polymer matrix, has solved many of the restrictions of monolithic piezoceramics. This type of material configuration is advantageous because it provides much higher strengths to crystalline materials in the fiber form due to reduced volume fractions of flaws during fabrication [13]. Also, in addition to protecting the fibers, the flexible nature of the polymer matrix allows their application to curved surfaces, making possible their usage to more realistic structures. Currently, there exists a broad number of PFC commercially available, but only three of the most promising types will be discussed in this section: macro fiber composites, hollow fiber composites, and active fiber composites.

1.4.1 Macro fiber composites

The first type of piezoelectric fiber composite (PFC) that will be discussed is the macro fiber composite (MFC) developed at the NASA Langley Research Center. The MFC consists of three primary components: active piezoelectric fibers, interdigitated electrodes, and a polymer matrix, as shown in Fig. 1.27.

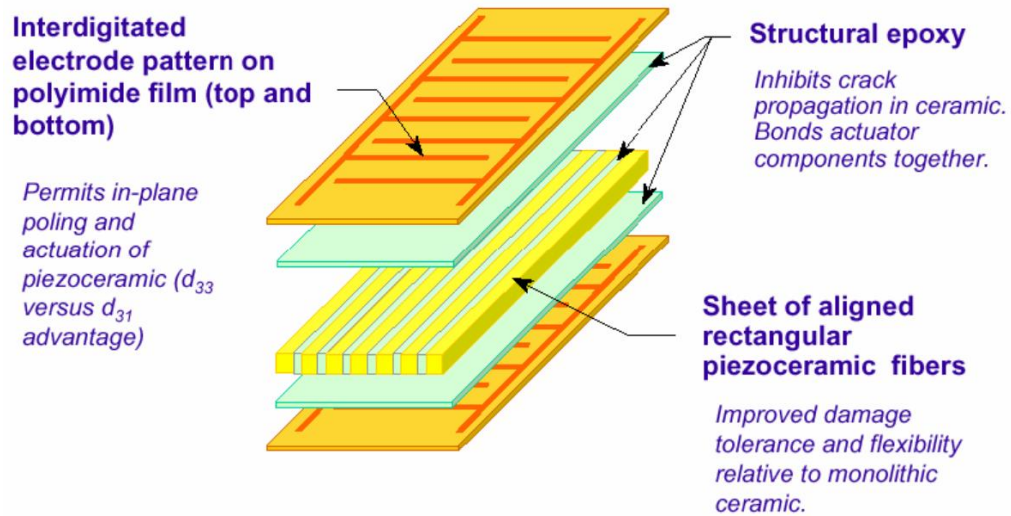


Fig. 1.27. Schematic showing the order of different layers in the macro-fiber composite actuator.

The piezoceramic fibers MFC utilizes have a rectangular cross section due to the method used to form the fibers. Fig 1.28 shows the fabrication process of the fibers. The piezoceramic wafer is placed on top of a polymer carrier film to hold the fibers in place while a computer controlled dicing saw cuts the piezoceramic fibers into the desired dimensions.

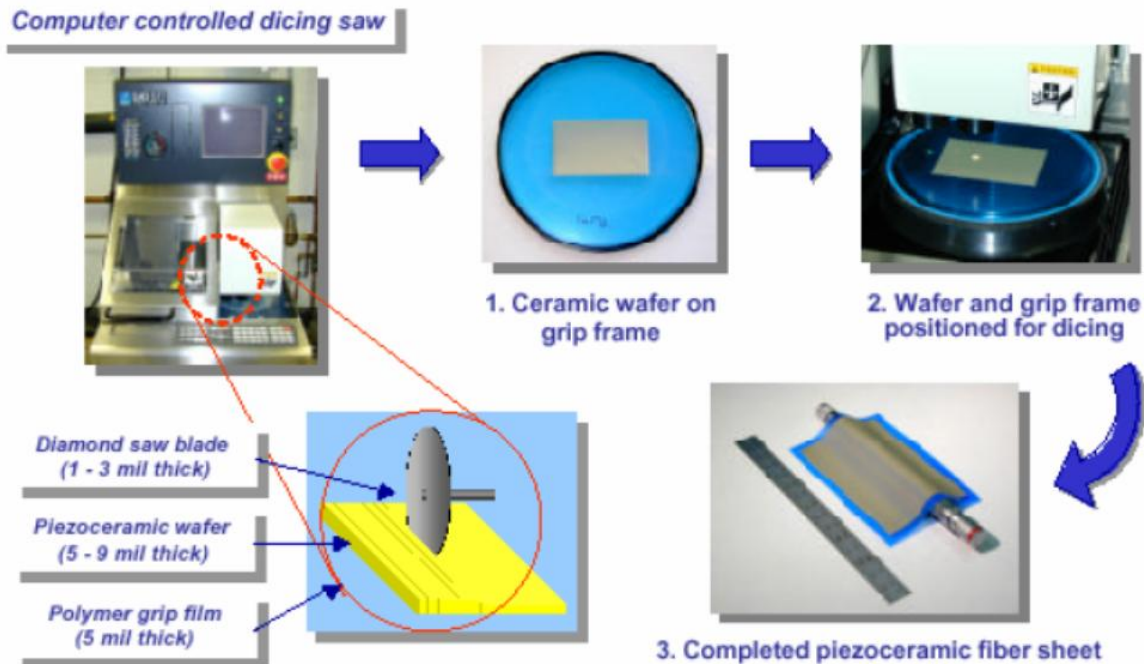
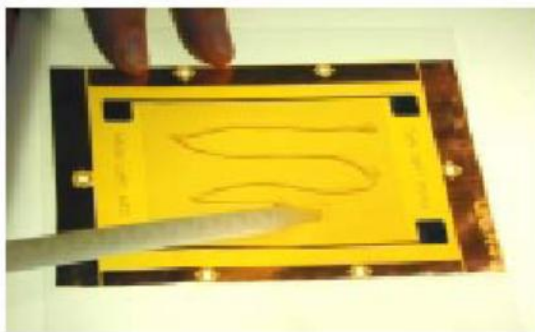


Fig. 1.28. Fabrication process of the macro-fiber composite piezofibers [224].

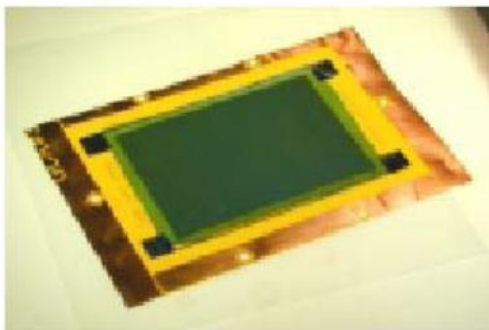
After the piezoceramic wafer has been cut, it is transferred and fixed at the bottom of an electrode film by heating up epoxy (polymer matrix) to secure the piezoceramic fibers. The polymer carrier film is then removed and a layer of epoxy is applied to the top of the piezoceramic fibers before applying the top electrode. This bonding process is shown in Fig 1.29. After the stacking process, the entire assembly is transferred to a vacuum press, where heat and pressure are applied to reduce the possibilities of voids in the epoxy matrix.



a) Preparation of bottom electrode film with epoxy adhesive.



b) Placement of fiber sheet on electrode film.



c) Fiber sheet and electrode film after heat tacking.



c) Removal of polymer carrier film from transferred piezoceramic fibers

Fig. 1.29. Fabrication of the macro fiber composites [225].

Due to the epoxy matrix the MFC is very flexible as shown in Fig. 1.30. Other advantages of MFC are the durability, low manufacturing cost, and high electromechanical coupling coefficients. One application for MFC that has been subject to great interest is structural sensing

and actuation. NASA's investigator W. Wilkie [225] bonded MFC patches to the vertical tail of a fighter aircraft to counteract the bending and torsional stresses that are inflicted on the tail during flight resulting from buffeting loads. A different type of study made by Park et al. [226] demonstrated that the MFC could be as an actuator to globally suppress vibration of an inflatable satellite structure. The component tested in this study was the torus which supports the reflector. This study was later extended by Sodano et al. [2] who showed that MFC could not only be used as an actuator but also as a sensor for the inflated torus. The MFC has also been proven to perform structural health monitoring as an impedance sensor.

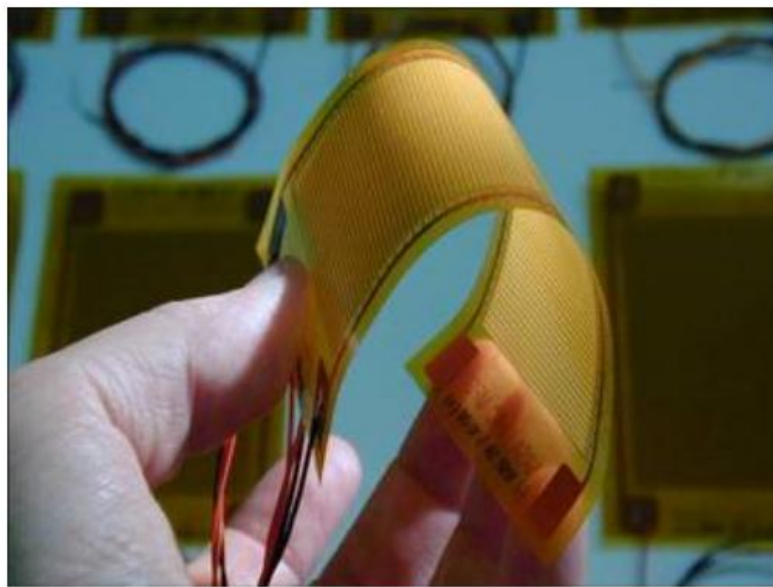


Fig. 1.30. Fabrication of the macro fiber composites.

1.4.2 Hollow fiber composites

The second type of PFC was introduced by Cannon and Brei [223] called hollow fiber composites (HFC). Since the HFC have very small diameters a new manufacturing technique had to be implemented for their fabrication called Microfabrication by Coextrusion (MFCX). The

three steps for this process are feed rod formation, extrusion, and burnout/sintering. A schematic drawing of the manufacturing process is shown in Fig. 1.31.

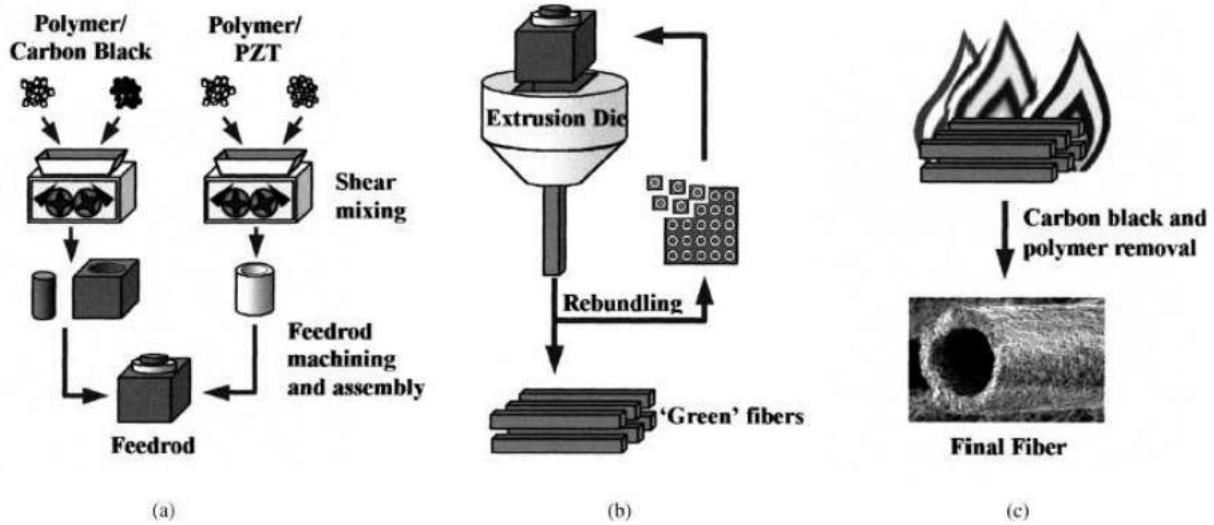


Fig. 1.31. MFCX fabrication process, a) feed rod formation, b) extrusion, c) burnout/sintering. [223]

In the feed rod formation process piezoelectric powder is mixed with thermoplastic polymers, and the same polymers are mixed with carbon black powder to form two mixtures with the same viscosity. The piezoelectric mix is then shaped into a round thin-walled cylinder, while part of the carbon black mix is formed into a smaller solid cylinder with the same outer diameter as the inside of the PZT tube. The remaining carbon black mix is then shaped into a square with a hole in the center to match the PZT cylinder. The extrusion process consists of heating up the assembled feed rod and inserting it into an extrusion die, which reduces the cross section of the rod. The last step called burnout/sintering consists of heating up the resulting "green" fibers to 1300°C for 48 hours. This process burns out the carbon black and thermoplastics polymer, resulting in a stronger and denser ceramic.

To form the electrodes, silver paint has to be added to the interior and exterior circumferences of the hollow fiber, and then the tubes are to be poled under an applied field. The formation of the active lamina is shown in Fig. 1.32.

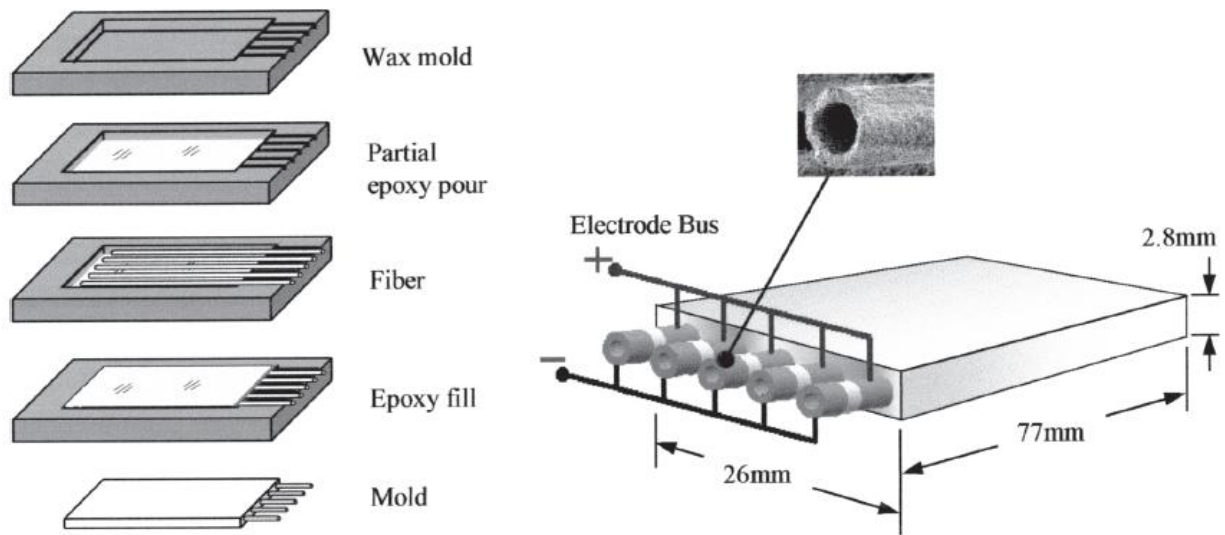


Fig. 1.32. Schematic showing of hollow fiber lamina fabrication. [223]

First, a wax mold is partially filled with epoxy into which the hollow fibers are placed in an aligned manner, leaving the ends of the fibers extending from one side of the mold. The rest of the mold is then filled with epoxy and left to cure. The assembly is then heated to melt the wax mold, leaving only the finished active lamina. The inner and outer electrodes are then connected to copper wires to form the electrode bus to allow an electric field to be applied to the composite.

Under optimal fabrication and volume fraction, the effective electromechanical coupling of active composite could be greater than 95% of the bulk active material used. However, the hollow nature of the fiber composite proved to be extremely fragile making its use in structural applications unlikely.

1.4.3 Active fiber composites

The last type of PFC that will be discussed, and in which this thesis is focused on, is the Active Fiber Composite (AFC) developed at the Active Materials and Structures Lab at MIT. This type of composite consists of aligned piezoceramic fibers embedded in a polymer matrix which may include glass fibers to increase the structural strength. A photomicrograph of an AFC'S cross-section is shown in Fig. 1.33.

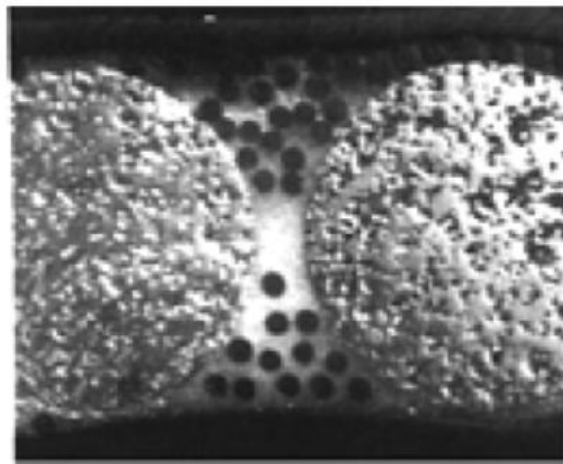


Fig. 1.33. Cross section of an Active Fiber Composite with glass rods. [13]

The solid fibers, circular in cross-section, are made by an extrusion process or injection molding process. A schematic figure of the manufacturing process of the active fiber composite is shown in Fig. 1.34. The fabrication process starts by placing the bottom interdigitated electrode on the aluminum vacuum plate using the locator pins. Two Kapton molds, placed on the bottom electrode, help retain the epoxy matrix while the piezoceramic fibers are aligned in a single layer and laid on top of the bottom electrode. At this point, the glass fibers can be added and aligned with the piezoceramic fibers to increase the mechanical strength of the composite. Epoxy resin mixed with an air-release agent is applied to the fibers, and the top electrode is positioned using the locator pins and positioning holes.

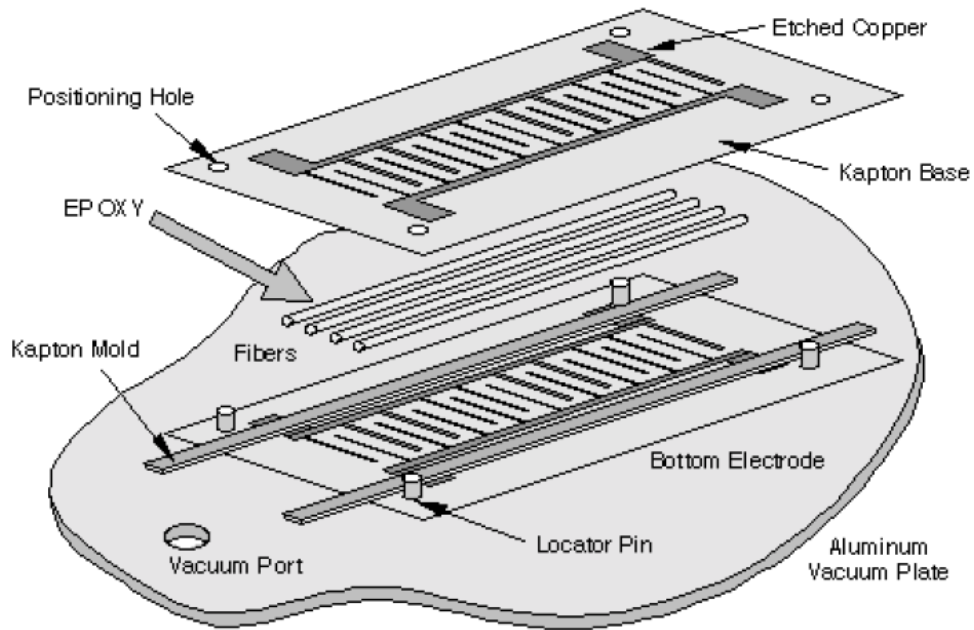


Fig. 1.34. Schematic of the manufacturing process of the active fiber composite. [13]

The plate is then placed in a press, where the resin is cured by applying heat and pressure, to minimize the voids in the composite which would decrease the efficiency. Finally, a DC voltage is applied through the interdigitated electrode to align the dipoles in the piezoceramic fibers. A final assembly of the active fiber composite is shown in Fig. 1.35.

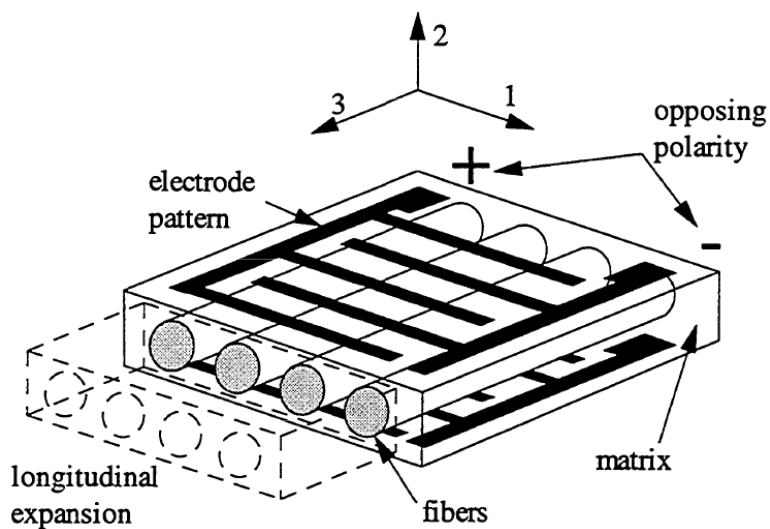


Fig. 1.35. Schematic of the active fiber composites. [227]

The AFC has shown promising structural applications due to its capability for direct incorporation into laminated composite materials.

CHAPTER 2:

MICROMECHANICS MODELING OF AN ACTIVE STRUCTURAL FIBER

2.1 Introduction

While current piezoceramic fiber composites have made huge advantages over monolithic piezoceramic materials, they are typically implemented as surface-bonded patches used for sensing or actuation only, separated from the structural components since they can't provide any additional strength to the composite. Therefore, a need existed to develop a piezoceramic fiber composites that could perform sensing and actuation as well as carry external mechanical loading. Researchers H. Sodano and Y. Lin developed a novel active structural fiber (ASF) that can be placed in a composite material to perform sensing and actuation while providing load bearing functionality. The piezoceramic fiber studied here will be coated onto a conductive structural fiber, which will enhance the piezoceramic mechanical properties while acting as an interior electrode, as shown in Fig 2.1.

The structural fiber will act as reinforcement, providing strength to the piezoelectric material which is very brittle; and at the same time, by using it as an internal electrode, the field required for actuation will be reduced over PFCs. These features will allow composites to be designed with numerous embedded functions such as structural health monitoring, power generation, vibration sensing and control, damping, and shape control through anisotropic actuation.

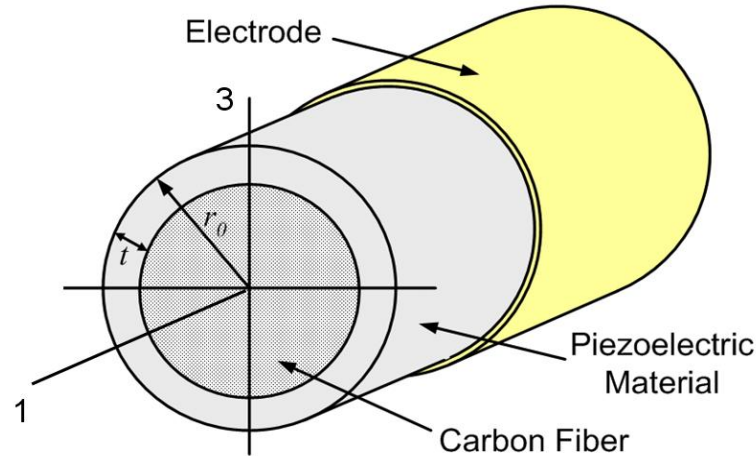


Fig. 2.1. Schematic showing the cross-section of the novel multifunctional fiber. [228]

This thesis will perform the modeling and simulation of a lead-free active structural fiber (ASF). First, a one-dimensional micromechanics model of a structural fiber coated with a piezoelectric material will be performed to evaluate the piezoelectric coupling coefficient of the ASF, which is directly related to its capability to couple energy between mechanical and electrical domains. Secondly, a three-dimensional micromechanics model will be implemented to estimate the effective electroelastic properties of the multifunctional composite and fully understand the electromechanical response of the composite. Lastly, a finite element analysis will be executed to validate the results from the 3D micromechanics model and show its accuracy to predict the electroelastic properties of the multifunctional composite.

2.2 One-Dimensional Micromechanics Model

The model used here was developed by Lin et al. [228], and it's based on the rule of mixture and an analogy between the thermal and piezoelectric responses of the composite to estimate the effective piezoelectric coupling coefficient in the fiber with different design parameters for both the ASF alone and the ASF lamina. For the ASF considered here the electric field will be applied through the thickness of the piezoelectric shell or through the radial axis. In piezoceramic modeling, the electric field applied on a thin plate piezoelectric structure is normally considered by thin-wall approximation. However, since the electric field across the piezoelectric shell is not constant, the non uniform electric field through the ASF must be modeled first. Therefore, from Gauss' Law, the thin wall electric field along the radial direction of the active fiber can be expressed as [229]

$$E(r) = \frac{-V}{r \ln(1 - \alpha)} \quad (2.1)$$

where V is the voltage applied through the fiber thickness, r is the radial position, and α is the aspect ratio of the piezoelectric portion of the fiber, equal to t/r_0 , where t is the thickness of the piezoelectric coating and r_0 is the total radius of the fiber. Using the thin wall approximation, the longitudinal piezoelectric stress of the piezoelectric shell can be expressed as

$$\sigma(r) = Y^p \varepsilon(r) = Y^p d_{31} E(r) \quad (2.2)$$

where Y^p is the longitudinal modulus of elasticity of the piezoelectric shell, α is the piezoelectric's longitudinal stress, ε is the piezoelectric's longitudinal strain, and d_{31} is the piezoelectric coupling. The subscript 31 denotes that the electric field is applied in the 3 direction, while the generated strain is in the 1 direction (see Fig 2.1). The total piezoelectric

force can then be determined by integrating the stress over the cross-section area of the piezoelectric shell,

$$F = \int_0^{2\pi} \int_{r_0-t}^{r_0} Y^p d_{31} E(r) r dr d\theta = \frac{-2\pi d_{31} Y^p V t}{\ln(1 - t/r_0)} \quad (2.3)$$

and the free strain can then be derived using Eq (2.3) and Hook's law:

$$\varepsilon = \frac{\sigma}{Y^p} = \frac{F}{A Y^p} = \frac{-2\pi d_{31} Y^p V t}{\pi [r_0^2 - (r_0 - t)^2] Y^p \ln(1 - t/r_0)} = \frac{-E_{tw} d_{31}}{(r_0/t - 0.5) \ln(1 - t/r_0)} \quad (2.4)$$

where $E_{tw} = V/t$ is the electric field derived by thin wall approximation, A is the cross-sectional area of the piezoelectric shell, and F is the piezoelectric force. Therefore, the free strain can be expresses as the product of thin wall electric field E_{tw} and the effective piezoelectric coupling of the ASF $d_{31,eff}^f$,

$$\varepsilon = \left(\frac{-d_{31}}{\ln(1 - \alpha)(1/\alpha - 0.5)} \right) E_{tw} = d_{31,eff}^f E_{tw} \quad (2.5)$$

where d_{31} is the piezoelectric coupling coefficient and $d_{31,eff}^f$ is the effective coupling of the piezoelectric shell incorporating the thin wall electric field approximation. The coupling for the piezoelectric shell must be then combined with the core fiber to determine the effective piezoelectric coupling of the piezoelectric structural fiber. The longitudinal elastic modulus of the active structural fiber can be defined using the rule of mixtures and written as [230]

$$Y^{multi} = Y^p \nu^p + Y^f (1 - \nu^p) \quad (2.6)$$

where Y is the longitudinal modulus of elasticity, ν is the volume fraction, and the superscripts f , p and $multi$ represent the core fiber, piezoelectric, and complete multifunctional piezoelectric

structural fiber, respectively. The relationship between aspect ratio and fiber volume fraction is shown in Fig. 2.2.

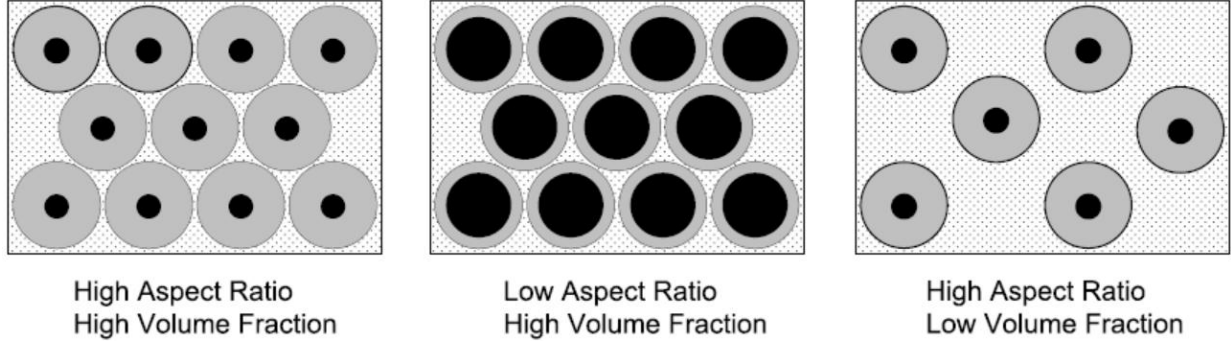


Fig. 2.2. Schematic demonstrating the relationship between the fiber aspect ratio and fiber volume fraction. [225]

According to equation (2.4) and (2.5), the piezoelectric force generated from the piezoelectric shell can be expressed as

$$F = A\varepsilon Y^p = \frac{-E_{tw}d_{31}}{(r_0/t - 0.5)\ln(1 - t/r_0)} AY^p = E_{tw}d_{31,eff}^f AY^p \quad (2.7)$$

Then, using Hook's Law the total strain of the ASF caused by the piezoelectric force is represented by

$$\varepsilon^{multi} = \frac{\sigma^{multi}}{Y^{multi}} = \frac{F}{A/v^p} = \frac{d_{31,eff}^f Y^p v^p E_{tw}}{Y^{multi}} = d_{31}^{multi} E_{tw} \quad (2.8)$$

therefore, the electromechanical coupling of a piezoelectric structural fiber with a piezoelectric coating can be defined as

$$d_{31}^{multi} = \frac{d_{31,eff}^f Y^p v^p}{(Y^p - Y^f)v^p + Y^f} \quad (2.9)$$

Y^p and Y^f are the elastic modulus of the piezoelectric material and fiber, respectively, v^p is the volume fraction of piezoelectric material, d_{31} is the piezoelectric coupling coefficient and $d_{31,eff}^f$ is the effective coupling of the piezoelectric shell as defined from Eq (2.5).

It must be noted that Eq. (2.9) predicts the response of a single active fiber; however, to be used in structural applications, multiple active fibers have to be embedded in a polymer matrix. In order to determine the coupling of a lamina composite with active fibers, the rule of mixture has to be applied once again by taking the piezoelectric shell to be an interphase layer. The resulting coupling can then be written as

$$d_{31}^{lam} = \frac{d_{31,eff}^f Y^p v^p}{(Y^p - Y^m) v^p + (Y^f - Y^m) v^f + Y^m} \quad (2.10)$$

2.3 Three-Dimensional Micromechanics Model

The one dimensional model results of the effective piezoelectric coupling coefficient will be shown in the following section. However, this model is only valid to determine the properties of the fiber; therefore to fully understand the behavior of the multifunctional composite the other electroelastic properties must be predicted. Since the fiber could be used in major research topics such as load bearing energy storage materials and intended to carry external mechanical loading, the effective elastic moduli and dielectric constant are properties necessary to estimate. Various methods exist for evaluating such properties as the Mori-Tanaka and self-consistent approaches. Although, the self-consistent method results in slow and complicated calculations while the Mori-Tanaka approach leads to less accurate estimations of the electromechanical moduli [232-234]. Current literature has shown the double inclusion model to be a powerful method for the

prediction of the effective elastic properties of composites with multiphase and multilayered inclusions. The three dimensional model utilized in this thesis was developed by Lin and Sodano [1] by extending the double inclusion approach for the prediction of the electroelastic properties of multiphase piezoelectric composites. Considering a transversely isotropic piezoelectric material, the linear constitutive equations that describe the coupled interaction between the electrical and mechanical domains can be expressed as

$$\sigma_{ij} = C_{ijmn} \varepsilon_{mn} - e_{nij} E_n \quad (2.11)$$

$$D_i = e_{imn} \varepsilon_{mn} + \kappa_{in} E_n \quad (2.12)$$

where σ_{ij} , ε_{mn} , E_n and D_i are the stress, strain, electric field and electric displacement tensors, respectively. C_{ijmn} is the elastic tensor at a constant electric field, e_{nij} is the piezoelectric field-stress tensor in a constant strain or electric field, and κ_{in} is the dielectric tensor at a constant strain. For the modeling of in homogeneous composites with piezoelectric inclusions, it is convenient to combine the mechanical and electrical variables such that the two equations can be expressed in a single constitutive equation [235]. To this end, the notation introduced by Barnett and Lothe [236] is utilized and briefly reviewed here. This notation is identical to conventional indicial notation with the exception that lower case subscripts are in the range of 1-3, while the capitalized subscripts are in the range of 1-4 and repeated capitalized subscripts summed over 1-4. With this notation, the elastic strain and electric field can be expressed as

$$Z_{Mn} = \begin{cases} \varepsilon_{mn}, & J = 1,2,3, \\ E_n, & J = 4, \end{cases} \quad (2.13)$$

similarly the stress and electric displacement can be represented as

$$\Sigma_{iJ} = \begin{cases} \sigma_{ij}, & J = 1,2,3, \\ D_i, & J = 4, \end{cases} \quad (2.14)$$

the electroelastic moduli can then be presented as

$$E_{iJ Mn} = \begin{cases} C_{ijmn} & J, M = 1, 2, 3, \\ e_{nij} & J = 1, 2, 3; M = 4, \\ e_{imn} & J = 4; M = 1, 2, 3, \\ \kappa_{in} & J, M = 4, \end{cases} \quad (2.15)$$

therefore, according to equations (2.13–2.15), the piezoelectric constitutive equations (2.11) and (2.12) can be combined into a single expression as

$$\Sigma_{iJ} = E_{iJ Mn} Z_{Mn} \quad (2.16)$$

the constitutive equation for an orthotropic piezoelectric material and the core fiber can be expressed in the matrix form as

$$\begin{bmatrix} \sigma_{11} \\ \sigma_{22} \\ \sigma_{33} \\ \sigma_{23} \\ \sigma_{13} \\ \sigma_{12} \\ D_1 \\ D_2 \\ D_3 \end{bmatrix} = \begin{bmatrix} C_{11} & C_{12} & C_{13} & 0 & 0 & 0 & 0 & 0 & -e_{31} \\ C_{12} & C_{22} & C_{23} & 0 & 0 & 0 & 0 & 0 & -e_{32} \\ C_{13} & C_{23} & C_{33} & 0 & 0 & 0 & 0 & 0 & -e_{33} \\ 0 & 0 & 0 & C_{44} & 0 & 0 & 0 & -e_{15} & 0 \\ 0 & 0 & 0 & 0 & C_{55} & 0 & -e_{15} & 0 & 0 \\ 0 & 0 & 0 & 0 & 0 & C_{66} & 0 & 0 & 0 \\ 0 & 0 & 0 & 0 & e_{15} & 0 & \kappa_1 & 0 & 0 \\ 0 & 0 & 0 & e_{15} & 0 & 0 & 0 & \kappa_2 & 0 \\ e_{31} & e_{32} & e_{33} & 0 & 0 & 0 & 0 & 0 & \kappa_3 \end{bmatrix} \begin{bmatrix} \varepsilon_{11} \\ \varepsilon_{22} \\ \varepsilon_{33} \\ \gamma_{23} \\ \gamma_{13} \\ \gamma_{12} \\ E_1 \\ E_2 \\ E_3 \end{bmatrix} \quad (2.17)$$

Using the direct approach [237] for the estimate of overall properties of heterogeneous materials, the volume-averaged piezoelectric fields in a multiphase active composite with N phases can be expressed as

$$\bar{\Sigma} = \sum_{r=1}^N c_r \bar{\Sigma}_r \quad (2.18)$$

$$\bar{Z} = \sum_{r=1}^N c_r \bar{Z}_r \quad (2.19)$$

where c_r is the volume fraction, the subscript r represents r^{th} phase of the composites, with 1 representing the matrix phase, the overbar denotes the volume average of the quantities. For a piezoelectric composite subjected to homogenous elastic strain and electric field boundary conditions, Z^0 , it has been shown that $\bar{Z}=Z^0$ [238]. Therefore, equation (2.16) can be represented as

$$\bar{\Sigma} = E\bar{Z} \quad (2.20)$$

the volume averaged strain and electric field in the r^{th} phase is

$$\bar{Z}_r = A_r \bar{Z} \quad (2.21)$$

where A_r is the concentration tensor of phase r and has the following properties,

$$\sum_{r=1}^N c_r A_r = I \quad (2.22)$$

where I is the forth order identity tensor. Combining equations (2.18–2.22), the overall electroelastic modulus predicted by the double inclusion model can be expressed as

$$E = E_1 + \sum_{r=2}^N c_r (E_r - E_1) A_r \quad (2.23)$$

where E is the extended electroelastic matrix as defined in Eq. (2.18) and A is the concentration tensor which is a function of the eshelby's tensor and the electroelastic properties of each phase. For the double inclusion model of a three phase composite as shown in Fig. 1, the concentration tensor is defined as [239]

$$\begin{aligned} A_3^{di} &= I + \Delta S \Phi_2 + S_3 \Phi_3 \\ A_2^{di} &= I + \left[S_2 - \frac{c_3}{c_2} \Delta S \right] \Phi_2 + \frac{c_3}{c_2} \Delta S \Phi_3 \end{aligned} \quad (2.24)$$

where S is the eshelby's tensor which is a function of the inclusion geometry as well as the electroelastic properties of the matrix, the explicit expression for a fibrous inclusion can be found elsewhere [235]. Φ is the forth order tensor which is a function of the eshelby's tensor and the electroelastic properties of each phase. The expression of Φ is given by the following expression,

$$\Phi_2 = - \left[\Delta S + (S_2 + F_3) \left(S_3 - \frac{c_3}{c_2} \Delta S + F_3 \right)^{-1} \left(S_3 - \frac{c_3}{c_2} \Delta S + F_2 \right) \right]^{-1} \quad (2.25)$$

$$\Phi_3 = - \left[(S_2 + F_3) + \Delta S \left(S_3 - \frac{c_3}{c_2} \Delta S + F_2 \right)^{-1} \left(S_3 - \frac{c_3}{c_2} \Delta S + F_3 \right) \right]^{-1}$$

where the F and ΔS are expressed as

$$F_2 = (E_2 - E_1)^{-1} E_1$$

$$F_3 = (E_3 - E_1)^{-1} E_1 \quad (2.26)$$

$$\Delta S = S_3 - S_2$$

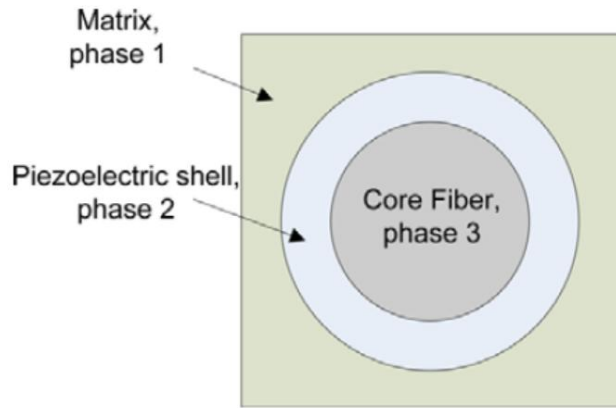


Fig. 2.3. Schematic illustrating of the three phase active composites.

The geometry of the ASF with the coordinate system used in this thesis is shown in Fig. 2 [228, 240]. In order to maintain consistency with Eshelby's tensor coordinates system [235,237], the

electric field applied through the thickness of the piezoelectric layer (along the radial direction) must be considered along the global coordinate system. Therefore, to account for the symmetry in the actual electric field the coupling in the -1 and -2 directions are taken to be equal. Because the ASFs are poled along the transverse direction, the traditional directions of standard convention in composites have been modified due to the concentric electrodes such that the poling axis occurs in both the -1 and -2 directions, as shown in Figure 2.4.

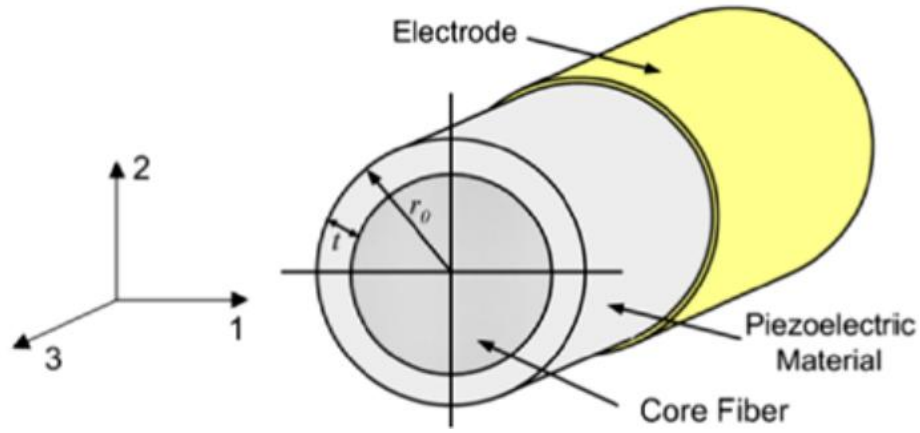


Fig. 2.4. Schematic drawing of the ASF in the global coordinate system.

Due to the concentric nature of the electrodes, a non-uniform local electric field occurs and has been evaluated by Lin and Sodano [228,240]. The relation between the local and the global electric field is defined as

$$E_{local} = \frac{-1}{(1/\alpha - 0.5)\ln(1 - \alpha)} E \quad (2.27)$$

where α is the aspect ratio defined as the ratio of piezoelectric shell thickness to the total radius of the ASF, E_{local} is the local electric field added through the thickness of the piezoelectric shell, and E is the electric field in the global coordinate system [235, 237]. The material properties used for modeling are shown in Table 2.1 [237]; note that not all the properties listed in equation (2.17) are shown due to the orthotropic nature of the materials.

Table 2.1. Electroelastic properties of reinforcement and matrix materials.

Material	C_{11} (GPa)	C_{12} (GPa)	C_{13} (GPa)	C_{33} (GPa)	C_{44} (GPa)	C_{66} (GPa)	κ_{11}	κ_{33}	e_{15} (C/m ²)	e_{31} (C/m ²)	e_{33} (C/m ²)
Matrix	8.1	5.4	5.4	8.1	1.4	1.4	2.8	2.8	0	0	0
Carbon fiber	24	9.7	6.7	11	27	11	12	12	0	0	0
BaTiO ₃	275.1	178.9	151.6	164.8	54.3	113.1	1970	109	21.3	-2.7	3.7

2.4 Results and Discussion

Both one and three-dimensional micromechanics modeling of the ASF were performed using the commercial software MATLAB. For the one-dimensional micromechanics model, the resulting electromechanical coupling ratio of the multifunctional fiber with respect to the fiber aspect ratio is plotted in Fig. 2.5.

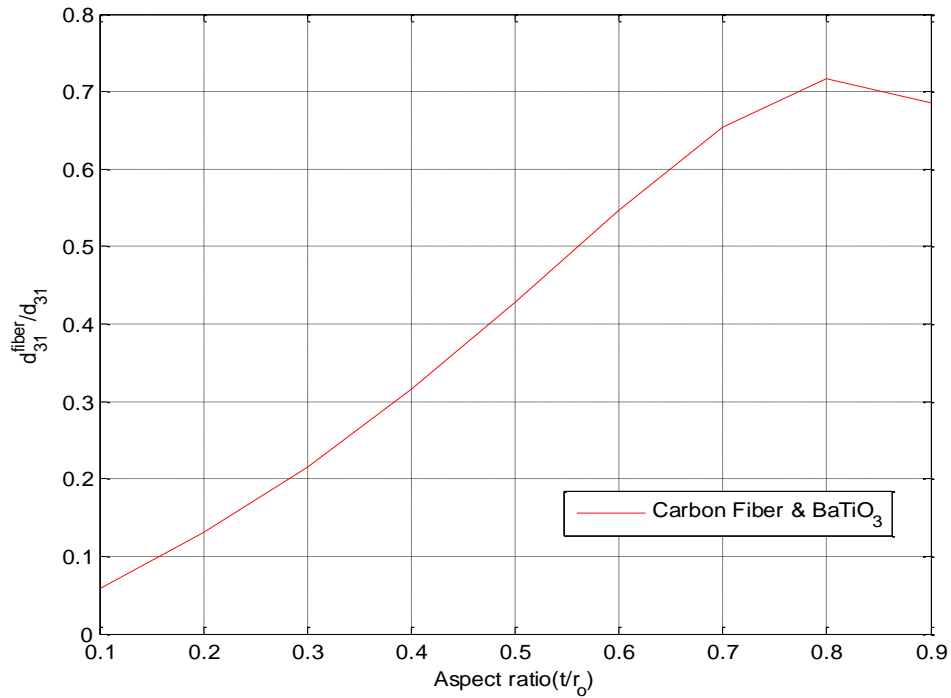


Fig. 2.5. Resulting electromechanical coupling of the ASF with respect to the aspect ratio.

The y-axis represents the ratio of the coupling coefficient, d_{31} of the multifunctional fiber to that of an active constituent. Therefore, a coupling ratio of 0.7 indicates that an active fiber with a BaTiO_3 shell could achieve 70% of the coupling of bulk BaTiO_3 . If we recall Eq. (2.5), it can be seen that at a certain electrical field, the aspect ratio is the only parameter that will influence the effective piezoelectric coupling d_{31}^{eff} of the ASF, and as expected the effective d_{31} increased with aspect ratio. However, the maximum value is obtained at approximately 0.8, point at which the surface area of the inner wall becomes much less than the outer wall, thus resulting in a breakdown of the thin wall approximation and leading to a very high electric field on the inner wall which could potentially depole the piezoelectric material. Therefore, producing active structural fibers (ASFs) with very high aspect ratio fiber is not practical due to the difficulty of the poling process, which will lead to either breakdown of the material at the inner wall due to the high electric field or only partial poling at the outer radius.

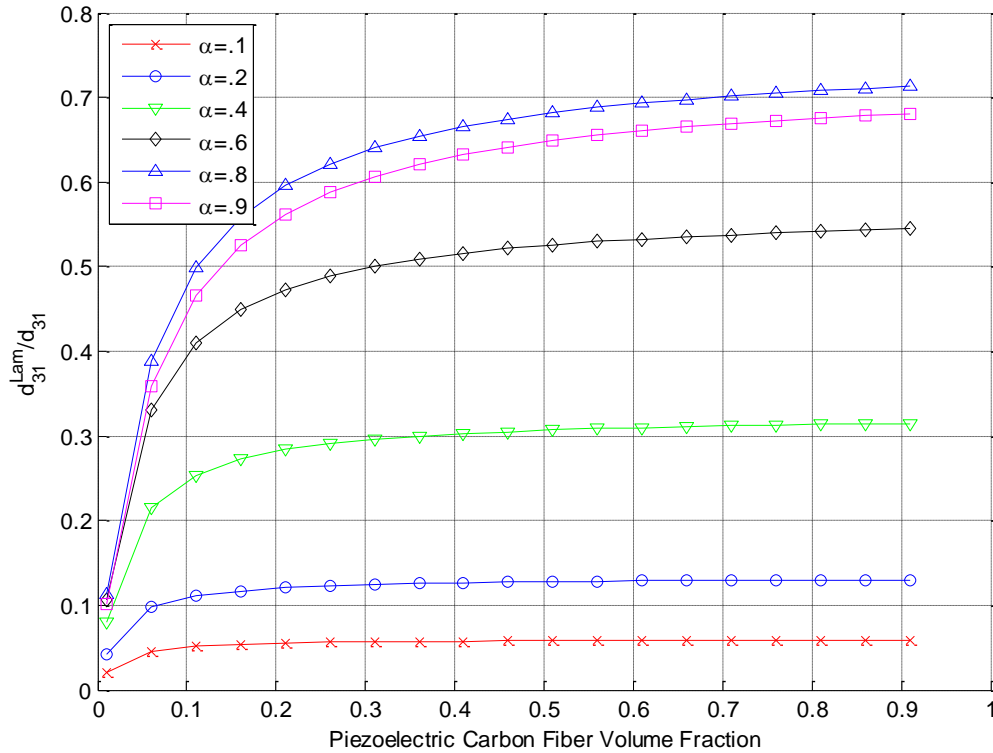


Fig. 2.6. Result for the active fiber coupling of a lamina consisting of the active structural fiber to that of bulk piezoelectric material, with respect to the volume fraction of the active fiber for various fiber aspect ratios.

The electromechanical coupling ratio of a lamina consisting of ASFs to the coupling of the bulk active constituent with different ASF volume fractions is shown in Fig. 2.6. It can be seen that the aspect ratio plays a more important role in the electromechanical coupling of the composite material. The results show that the active structural fiber presented here could lead to structural composites with piezoelectric coupling coefficients as high as 70% of the active constituent. A composite with such coupling levels could be used for a wide variety of applications; but before we have to fully understand the electroelastic properties of the entire composite. This is why a three-dimensional micromechanics model was performed using MATLAB to evaluate the effective electroelastic properties of the multifunctional composite with different aspect ratios. The fiber volume fraction is defined as the ratio of the ASF (core structural fiber and piezoelectric shell) to the matrix material. Fig. 2.7 shows the effective Young's modulus of the composite.

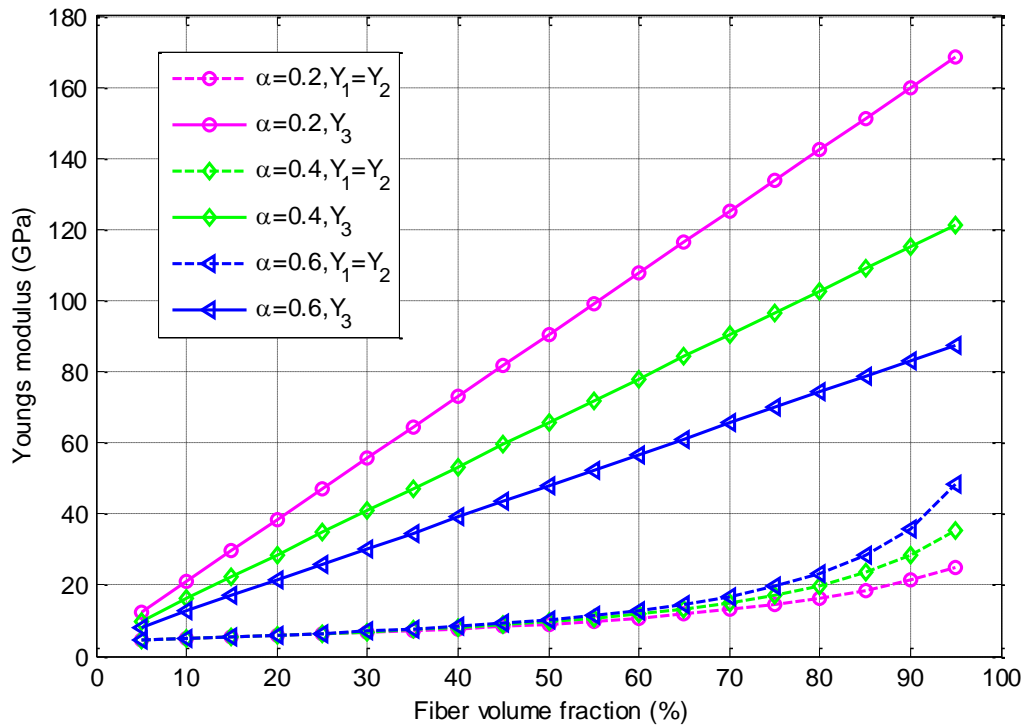


Fig. 2.7. Effective Young's modulus with respect to ASF volume fraction.

The longitudinal Young's modulus Y_3 , increases linearly with volume fraction while the transverse young's modulus $Y_1=Y_2$ increases exponentially. Because the fiber volume fraction is considered to be the fraction of the entire ASF, increasing the aspect ratio at the same volume fraction leads to a larger fraction of piezoelectric constituent. Since the piezoelectric material has a lower longitudinal modulus and higher transverse modulus than the core fiber, the overall longitudinal and transverse moduli decrease and increase respectively with the increasing aspect ratio. The effective shear modulus is shown in Fig. 2.8.

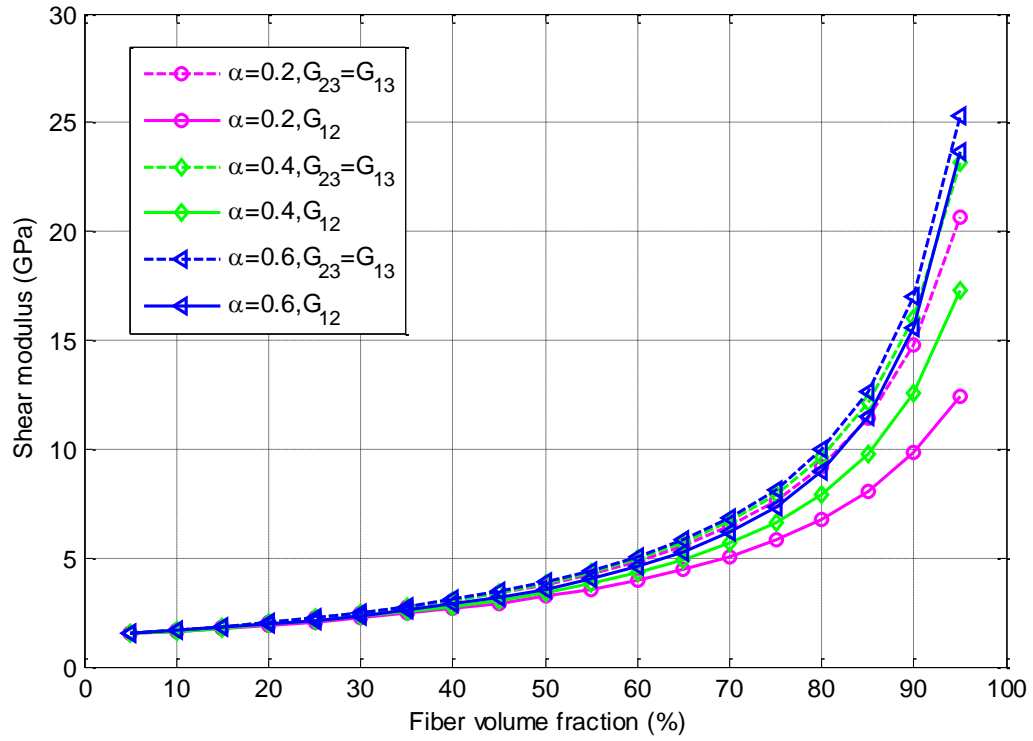


Fig. 2.8. Effective Shear modulus with respect to ASF volume fraction.

It can be seen that the longitudinal shear $G_{23}=G_{13}$ modulus is highly dependent on the volume fraction and quite insensitive to the aspect ratio. Whereas the transverse shear modulus G_{12} has a larger dependence on aspect ratio and increases with volume fraction. The dielectric constant model results of the composite are shown in Fig. 2.9.

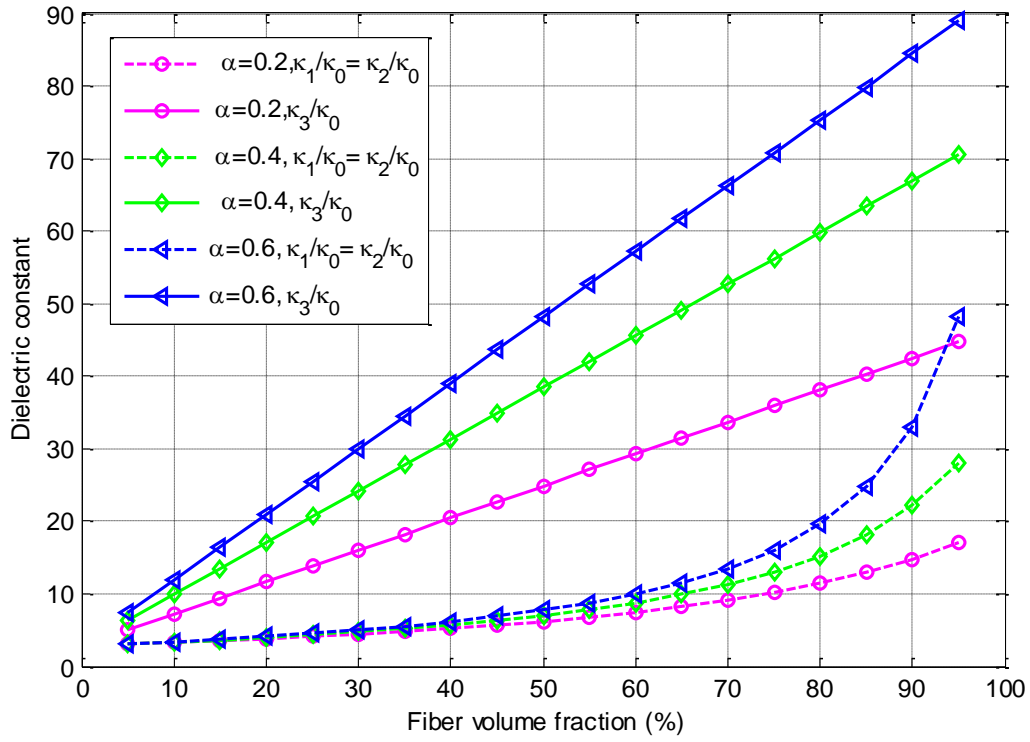


Fig. 2.9. Effective relative dielectric constant with respect to ASF volume fraction.

Both longitudinal and transverse dielectric constants increase with increasing volume fraction and aspect ratio, but the longitudinal constant increases linearly while the transverse constant increases exponentially. The model shows promising results for the electroelastic properties of the multifunctional composite for realistic applications, but before implementing it, we have to corroborate these properties with a finite element analysis.

CHAPTER 3:

FINITE ELEMENT MODELING

3.1 Introduction

In order to validate the micromechanics models, a finite element analysis of a representative volume element (RVE) of the composite has been performed using the commercial software ABAQUS. Because the finite element model predicts the stress and strain fields inside the inclusion, piezoelectric shell and matrix, the predicted properties are very accurate [237]. Therefore, the finite element results can be used to check the accuracy of the three dimensional micromechanics model developed.

3.2 3D Finite Element Model

An example of the FEA model used is shown in Figure 3.1. In order to determine the independent electroelastic material parameters described in the previous section, a series of simulations with different aspect ratio ASFs and volume fraction representative volume elements (RVEs) have been performed.

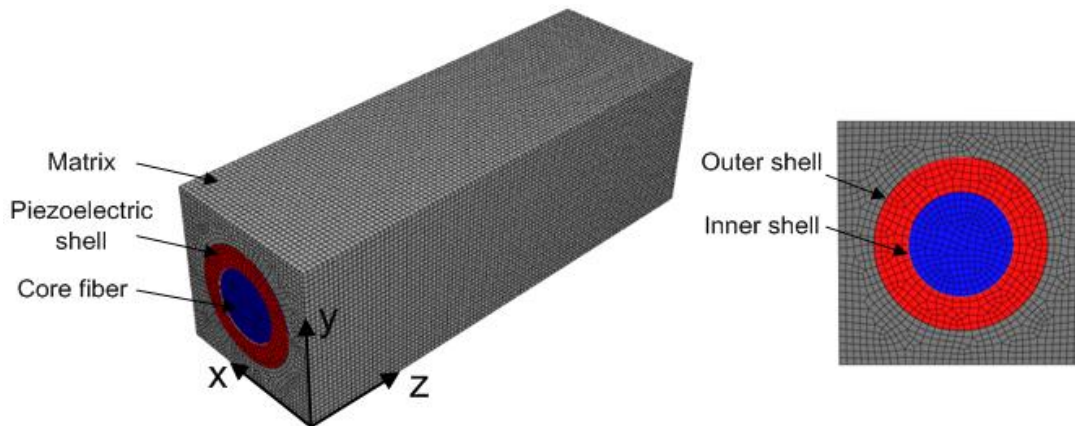


Fig. 3.1. FEM model of multifunctional composite with the front view shown on the right.

As mentioned before, the FEA was performed using the FEM software ABAQUS. The RVEs (core fiber, piezoelectric, and epoxy matrix) were meshed with three dimensional 20-noded quadratic elements, with three displacement degrees of freedom and one electrical degree of freedom for each node. Two “TIE” constraint commands were used for the core fiber/piezoelectric shell and piezoelectric shell/epoxy matrix which result in zero relative motion between the surfaces. To make easier the modification of changing volume fraction, a square RVE has been used. For each FEA, the volume fraction was obtained by holding the same dimensions for the fiber while adjusting the matrix size. The boundary conditions used in all the simulation are listed in Table 3.1. where a and c are the dimensions of the finite element unit cell in the x and z axes.

Using the strain energy approach, the effective Young's and shear modulus can be calculated [237]. The elastic strain energy of the RVE under mechanical strain can be expressed as

$$U_s = \frac{V}{2} C_{ijkl} \epsilon_{ij} \epsilon_{kl} \quad (3.1)$$

where V is the volume of the RVE, C_{ijkl} is the effective elastic modulus, ϵ_{ij} and ϵ_{kl} are the strain applied to the RVE. The strain energy of the entire RVE can be obtained directly from ABAQUS. By solving the equation, the effective tensile modulus ($ij = kl = 11, 22, 33$) and the effective shear modulus ($ij = kl = 44, 55, 66$) can be calculated.

In order to evaluate the effective dielectric constant, the electric field was applied on the surfaces of the RVE. The stored electrostatic energy can be expressed as [241]

$$U_e = \frac{1}{2} \kappa_{eff} \frac{s}{d} (\varphi_2 - \varphi_1)^2 \quad (3.2)$$

where k_{eff} is the effective dielectric constant of the entire RVE, s is the area of the each surface exposed to the electric field, d is the distance between the two surfaces, φ_1 and φ_2 is the electric potential applied to them. The electrostatic energy was calculated in ABAQUS allowing the effective dielectric constant to be calculated from equation (3.2).

Table 3.1. FEA boundary conditions for identifying each of the constituent properties.

Parameter	Mechanical boundary condition	Electrical boundary condition
C_{11}	$u_1(x = 0) = 0$	$\varphi = 0$
	$u_1(x = a) = \varepsilon^0$	
C_{33}	$u_3(z = 0) = 0$	$\varphi = 0$
	$u_3(z = c) = \varepsilon^0$	
C_{44}	$u_1(z = 0) = 0$	$\varphi = 0$
	$u_2(z = 0) = 0$	
	$u_3(z = 0) = 0$	
	$u_2(z = c) = \varepsilon^0$	
C_{66}	$u_1(x = 0) = 0$	$\varphi = 0$
	$u_2(x = 0) = 0$	
	$u_3(x = 0) = 0$	
	$u_2(x = a) = \varepsilon^0$	
κ_{11}	$u_1(x = 0) = 0$	$\varphi(x = 0) = 0$
	$u_2(x = 0) = 0$	
	$u_3(x = 0) = 0$	$\varphi(x = a) = \varphi_0$
κ_{33}	$u_1(z = 0) = 0$	$\varphi(z = 0) = 0$
	$u_2(z = 0) = 0$	
	$u_3(z = 0) = 0$	$\varphi(z = c) = \varphi_0$
d_{13}	$u_1(z = 0) = 0$	$\varphi(\text{outer shell}) = 0$
		$\varphi(\text{inner shell}) = \varphi_0$
d_{11}	$u_3(x = 0) = 0$	$\varphi(\text{outer shell}) = 0$
		$\varphi(\text{inner shell}) = \varphi_0$

3.3 Results and Discussion

Once the finite element (FE) model was created it could be used to validate the accuracy of the micromechanics models developed by comparing the electroelastic properties predicted by the model and the FEA. Due to time constraints, only FE analyses of aspect ratios 2, 4, and 6

were simulated. The fiber volume fraction is defined as the ratio of the ASF (core structural fiber and piezoelectric shell) to the entire RVE. The effective Young's moduli of the multifunctional composites with different aspect ratios predicted by the FEA are shown in Figure 3.2.

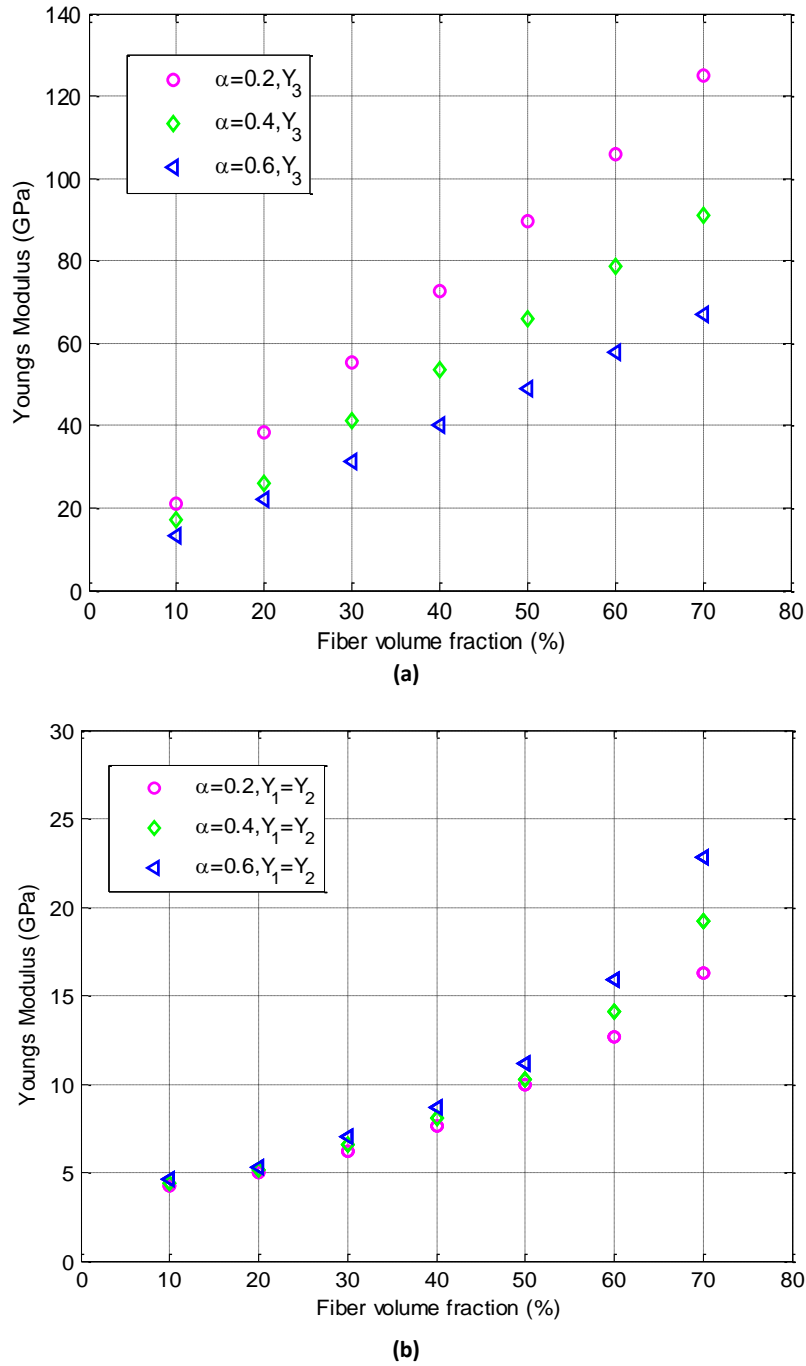


Fig. 3.2. Effective Young's modulus with respect to ASF volume fraction, (a) longitudinal Young's modulus, (b) transverse Young's modulus.

The FEA results of the longitudinal Young's modulus Y_3 increase linearly with volume fraction and show very good agreement with the model for all aspect ratios and volume fractions considered. For the transverse Young's modulus $Y_1=Y_2$, the modulus increases exponentially for both model and FEA, but the FEA predicts a slightly larger rate of increase than the model at bigger volume fractions. The maximum error (26%) occurs when the aspect ratio is 0.6 with a fiber volume fraction of 0.7. By increasing the aspect ratio at the same volume fraction, the portion of the piezoelectric material increases while the core fiber decreases. Since the piezoelectric material has a lower longitudinal modulus and higher transverse modulus than the core fiber, therefore, the overall longitudinal and transverse moduli decrease and increase with the increasing aspect ratio, respectively. The effective shear moduli are shown in Figure 3.3.

As the model, Figure 3.3(a) shows the FEA longitudinal shear $G_{13}=G_{12}$ modulus increases linearly and is highly dependent on the volume fraction and quite insensitive to the aspect ratio. The transverse shear modulus G_{12} is shown in Figure 3.3(b) increasing exponentially with aspect ratio and volume fraction. Although the FEA results show agreement with the model for both the longitudinal and transverse shear modulus, the error increases at high volume fractions.

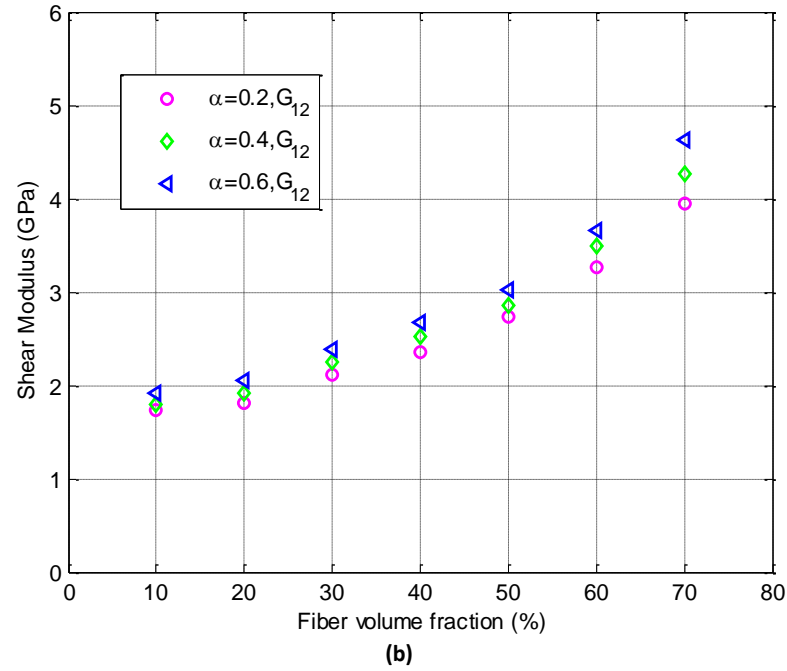
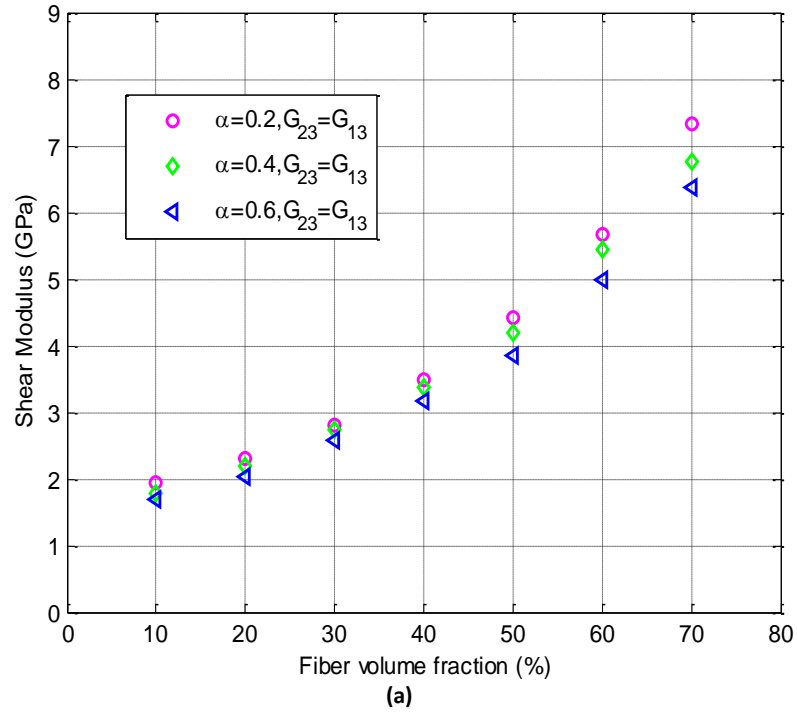


Fig. 3.3. FEA Effective Shear modulus with respect to ASF volume fraction, (a) longitudinal Shear modulus, (b) transverse Shear modulus.

The longitudinal dielectric constants obtained from the FEA are shown in Figure 3.4. Since the piezoelectric has largest dielectric constant of all three constituents, the longitudinal

dielectric constant increases with increasing aspect ratio and volume fraction. The results have a great agreement with the model for all aspect ratios and volume fractions. Due to time constraints, the transverse dielectric constant could not be simulated in ABAQUS. But in general, piezoelectric materials have very high dielectric properties which make the three phase piezoelectric composites studied here a strong candidate for multifunctional structural capacitors that combine energy storage with load bearing capability [242].

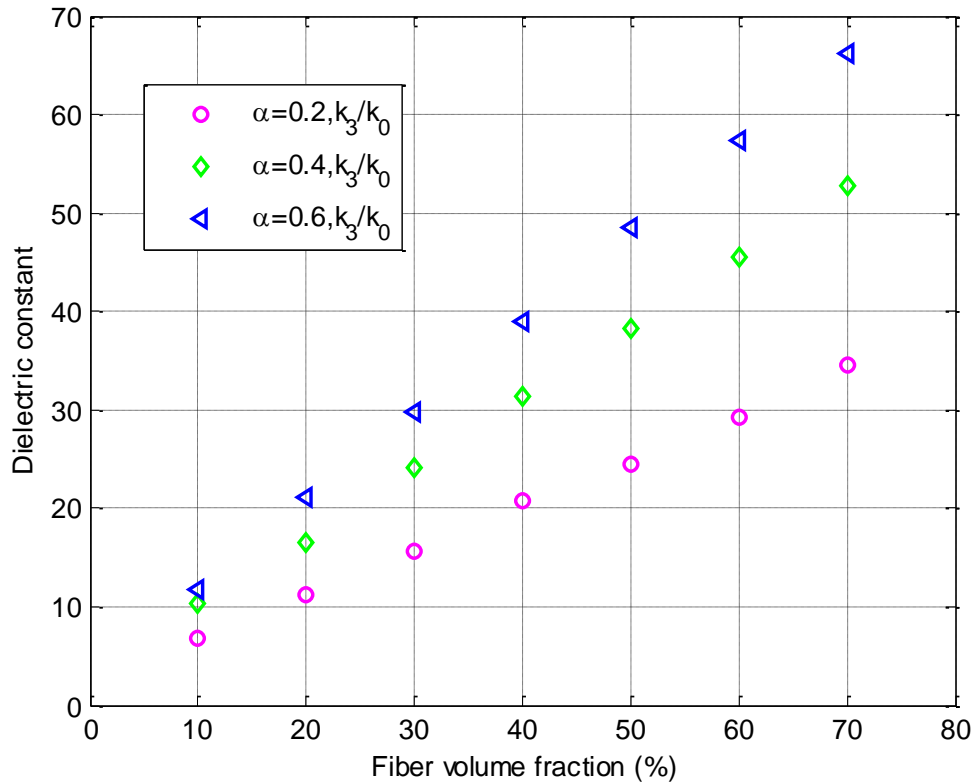


Fig. 3.4. FEA Effective Longitudinal Dielectric constant with respect to ASF volume fraction

CHAPTER 4:

CONCLUSION

4.1 Summary of Thesis and Results

This thesis has studied a one dimensional model, which is able to predict the effective longitudinal piezoelectric coupling coefficient, and a three dimensional micromechanics model which can estimate fully the electroelastic properties of the entire composite. The effective longitudinal piezoelectric coupling coefficient, which defines the materials ability to transforms energy between the electrical and mechanical domains, was evaluated using a code developed in the commercial software MATLAB. The results from the one dimensional model showed that the effective coupling coefficient of the multifunctional composites could reach as high as 70% of that of the bulk piezoceramic constituent used.

While the one dimensional model is be able to predict the effective piezoelectric coupling coefficient of the multifunctional composites, other electroelastic properties such as effective Young's modulus and dielectric constant are also important for the design of the multifunctional composite. Therefore, a three dimensional model based on the double inclusion model was used to evaluate the properties of the composite. The results showed that the properties of the multifunctional composite doubled in the least to the ones of a bulk active constituent. The results predicted by the 3D model were validated by a three dimensional finite element analysis. For all the electroelastic properties, good agreement between the micromechanics model and finite element model was shown, proving the accuracy of the model in evaluating the properties of the multifunctional composite.

The use of a carbon structural fiber allows the resulting active structural fiber to carry external mechanical stresses due to its excellent modulus and strength, while protecting the piezoelectric layer from breaking under mechanical loading. This simplified design allows the active structural fiber to carry mechanical load while performing the electromechanical functionalities of piezoelectrics such as sensing, actuation, health monitoring, energy storage or harvesting, vibration control, etc.

4.2 Recommendations for Future Work

This thesis has performed a one dimensional and three dimensional model of an active structural fiber to predict the effective electroelastic properties of the multifunctional composite. Modeling and FEA results showed that the micromechanics models can accurately predict the response of the active structural fiber and the multifunctional composite. Lead zirconium titanate (PZT) is considered as the lead high-performance piezoelectric material and is widely used in sensors and actuators. However, PZT-based ceramics with above 60 wt % Pb will be prohibited in the near future from many practical applications because of their toxicity during preparation and processing. Barium Titanate was chosen as the piezoelectric material for the active structural fiber due to its lead-free nature to help solve some of the health and environmental issues related to lead-based materials. Its great dielectric properties make a multifunctional composite made of BaTiO₃ excellent candidates for energy storage composites with the added functionality of load bearing capacity. However, the piezoelectric performance of BaTiO₃ is still far lower than that of PZT, and its low Curie temperature is also a factor that limits its applications. Therefore, the need to develop strong lead-free piezoelectric materials to replace PZT resulted in the enhancement of lead-free piezoelectrics based on Potassium Sodium Niobate (KNN). This material is a good candidate to replace PZT due to its high Curie temperature and good

piezoelectric properties. An active structural fiber with piezoelectric coating of KNN could be modeled to evaluate its piezoelectric coupling coefficient and electroelastic properties to predict the possibility of using such multifunctional composite for sensing and actuation, as well as structural strength.

REFERENCES

1. Lin, Y.; Sodano, H.A. "A double inclusion model for multiphase piezoelectric composites". *Smart Mater. Struct.* 2010 19 035003
2. Sodano HA, Park G, Inman DJ. "An investigation into the performance of macro-fiber composites for sensing and structural vibration applications". *Mechanical Systems and Signal Processing* 2003; 18(3): 683-97
3. Jones, D.J., S.E. Prasad, and J.B. Wallace, "Piezoelectric materials and their applications, in *Advanced Ceramic Materials*". 1996, *Trans Tech Publications*: Clausthal Zellerfe. p. 71-143.
4. Uchino K. "Ch. 10: Present status of piezoelectric/electrostrictive actuators and remaining problems". *Piezoelectric Actuators and Ultrasonic Motors*. ed. H.L. Tuller. 1997, Boston: Kluwer Academic Publishers.
5. Setter, N., "Piezoelectric materials and devices". *Ceramics Laboratory*, EPFL Swiss Federal Institute of Technology, Lausanne, 2005.
6. Randall, C.A., et al., "High strain piezoelectric multilayer actuators - A material science and engineering challenge". *Journal of Electroceramics*, 2005 14(3) p. 177-191.
7. Jaffe, B.; Cook, W.R.; Jaffe, H. "Piezoelectric ceramics". *New York: Academic Press*. 1971
8. Donnelly, N.J., T.R. Shrout, and C. A. Randall, "Addition of a Sr, K, Nb (SKN) combination to PZT(53/47) for high strain applications". *Journal of the American Ceramic Society*, 2007 90(2) p. 490-495.
9. EU-Directive 2002/96/EC: "Waste Electrical and Electronic Equipment (WEEE)". *Off. J. Eur. Union*, 2003 46(L37) p. 14.
10. EU-Directive 2002/95/EC: "Restriction of the Use of Certain Hazardous Substances in Electrical and Electronic Equipment (RoHS)". *Off. J. Eur. Union*, 2003 46(L37) p. 4.
11. California Health and Safety Code, 2006 p. 25214.9-25214.10.2.
12. Directive 2000/53/EC of the European Parliament and of the Council of 18 September 2000 in end-of-life vehicles. *Off. J. Eur. Union*, 2000 L 269(21.10.2000) p. 34-42.
13. Williams, R.B; Park, G.; Inman, D.J.; Wilkie, W.K. "An Overview of Composite Actuators with Piezoceramic Fibers" *Proc. of the 20th International Modal Analysis Conference*, Orlando, FL. 2002
14. Park, S.E; Shrout, T.R.; "Ultrahigh strain and piezoelectric behavior in relaxor based ferroelectric single crystals". *Journal of Applied Physics*, 1997 82(4) p. 1804-1811.

15. Tuller, H.L.; Avrahami, Y. "Electroceramics" *Encyclopedia of Smart Materials*. John Wiley & Sons, New York, 2002.
16. Goldschmidt, V.M.; Shrifter Norske, I.; Mat.-Naturv. 2(1926)
17. Von Hippel, A.; Breckenridge, R.G.; Chesley, F.G.; Tisza, L. *Ind. Eng. Chem.* 38, p.1097-109 (1946).
18. L. Guo; Luo, H.; Gao, J.; Guo, L.; Yang, J. *Materials Letters* 60 (2006) 3011.
19. H.T. Kim, Y.H. Han, *Ceram. Int.* 30 (2004) 1719.
20. M. Boulos; Guillement-Fritsch, S.; Mathieu, F.; Durand, B.; Lebey, T.; Bley, V. *Solid State Ionics* 176 (2005) 1301.
21. F. Jona; Shirane, G. *Ferroelectric crystals*, Dover Publications, INC., New York, 1993
22. M.T. Benlahrache; Barama, S.E.; Benhamla, N.; Achour, A. *Mater. Sci. in Semicond. Proc.* 9 (2006) 1115.
23. N.J. Donnelly; Shrout, T.R; Randall C.A. 2007 *J. Am. Ceram. Soc.* 90 490
24. <http://www.faqs.org/health/Sick-V3/Lead-Poisoning.html>.
25. Off. J. Eur. Union 46 14. 2003.
26. Off. J. Eur. Union 46 4. 2003.
27. 2006 California Health and Safety Code 25214.9–25214.10.2
28. Off. J. Eur. Union L 269 34. 2000.
29. M. Miyayama and I.-S. Yi, *Ceramics International* 26, 529-533 (2000).
30. T. Takenaka and K. Sakata, *Japanese Journal of Applied Physics* 19, 31-39 (1980).
31. Z. Zhang, H. Yan, P. Xiang, X. Dong, and Y. Wang, *Journal of the American Ceramic Society* 87, 602-605 (2004).
32. E. C. Subbarao, *Journal of Physics and Chemistry of Solids* 23, 665-676 (1962).
33. R. E. Newnham; Wolfe, R.W.; Horsey, R.S.; Diaz-Colon, F.A; Kay, M.I. *Materials Research Bulletin* 8, 1183-1195 (1973).
34. V. M. Goldschmidt, *Klasse* 2, 8 (1929).
35. Jaffe, B.; Cook, J.W.R.; Jaffe, H. "Piezoelectric ceramics". *Vol. Academic Press*. 1971, London.
36. Grinberg, L., et al., "Predicting morphotropic phase boundary locations and transition temperatures in Pb- and Bi-based perovskite solid solutions from crystal chemical data and first-principles calculations". *Journal of Applied Physics*, 2005 98(9) p. 094111.

37. Kay, H.F.; Vousden, P. "Symmetry changes in barium titanate at low temperatures and their relation to its ferroelectric properties". *Phil. Mag.* 1949, 40, 1019-1040.
38. Merz, W.J. "The electric and optical behavior of BaTiO₃ single-domain crystals". *Phys. Rev.* 1949, 76, 1221-1225.
39. Wada, S.; Suzuki, S.; Noma, T.; Suzuki, T.; Osada, M.; Kakihana, M.; Park, S.E.; Cross, L.E.; Shrout, T.R. "Enhanced piezoelectric property of barium titanate single crystals with engineered domain configurations". *Jpn. J. Appl. Phys. Pt. 1* 1999, 38, 5505-5511.
40. Takahashi, H.; Numamoto, Y.; Tani, J.; Matsuta, K. "Lead-Free Barium Titanate Ceramics with Large Piezoelectric Constant Fabricated by Microwave Sintering". *Japanese Journal of Applied Phys. Part 1*, 45(1):L30–L32, 2006.
41. Capurso, J.S.; Schulze, W.A. "Piezoresistivity in PTCR barium titanate ceramics: I, experimental findings". *J. Amer. Ceram. Soc.* 1998, 81, 337-346.
42. Guillemet-Fritsch, S.; Valdez-Nava, Z.; Tenailleau, C.; Lebey, T.; Durand, B.; Chane-Ching, J.Y. "Colossal permittivity in ultrafine grain size BaTiO_{3-x} and Ba_{0.95}La_{0.05}TiO_{3-x} materials". *Advan. Mater.* 2008, 20, 551-555.
43. Ren, X.B. "Large electric-field-induced strain in ferroelectric crystals by point-defect-mediated reversible domain switching". *Nat. Mater.* 2004, 3, 91-94.
44. Rogan, R.C.; Tamura, N.; Swift, G.A.; Ustundag, E. "Direct measurement of triaxial strain fields around ferroelectric domains using X-ray microdiffraction". *Nat. Mater.* 2003, 2, 379-381.
45. Zhang, L.X.; Erdem, E.; Ren, X.B.; Eichel, R.A. "Reorientation of (MnTi"-VO••) x defect dipoles in acceptor-modified BaTiO₃ single crystals: an electron paramagnetic resonance study". *Appl. Phys. Lett.* 2008, 93, 2002901-1-202901-3.
46. Leontsev, S.O.; Eitel, R.E. "Progress in engineering high strain lead-free piezoelectric ceramics". *Sci. Technol. Adv. Mater.* 2010, v.11, 044302.
47. Jaffe, B.; Cook, W. R.; Jaffe, H. "Piezoelectric Ceramics". *New York: Academic.* 1971. 135-171.
48. Shrout, T. R.; Zhang, S. J. "Lead free piezoelectric ceramics: Alternatives for PZT?". *Electroceram.* 2007, 19, 111-124.
49. Tani, T. "Crystalline-oriented piezoelectric bulk ceramics with a perovskite-type structure". *J. Korean Physical Society.* 1998, 32 p. S1217-S1220.
50. Messing, G.L. "Templated grain growth of textured piezoelectric ceramics". *Critical Reviews in Solid State and Materials Sciences.* 2004, 29(2) p. 45-96.
51. Wada, S. "Enhanced piezoelectric properties of barium titanate single crystals with different engineered-domain sizes". *J. of Applied Physics*, 2005 98(1) p. 014109.

52. Park, S.E.; Shrout, T.R. "Ultrahigh strain and piezoelectric behavior in relaxor-based ferroelectric single crystals". *Journal of Applied Physics*, 1997 82(4) p. 1804-1811.
53. Wada, S. "Domain wall engineering in lead-free piezoelectric grain-oriented ceramics". *Ferroelectrics*. 2008. 373 p. 11-21.
54. Park, S.E. "Crystallographically engineered BaTiO₃ single crystals for high performance piezoelectrics". *Journal of Applied Physics*, 1999. 86(5) p. 2746-2750.
55. Takenaka, T.; Nagata, H.; Hiruma, Y. "Current developments and prospective of lead-free piezoelectric ceramics". *Japan. J. Appl. Phys.* 2008, v.47, 3787-3801.
56. Gray, R.B. "Transducer and method of making the same, in United States Patent Office". 1949, Erie Resistor Corporation: USA.
57. Roberts, S. "Dielectric and piezoelectric properties of barium titanate". *Physical Review*, 1947, 71(12) p. 890-895.
58. Bechmann, R. "Elastic, piezoelectric, and dielectric constants of polarized barium titanate ceramics and some applications of the piezoelectric equations". *Journal of the Acoustical Society of America*, 1956, 28(3) p. 347-350.
59. Takahashi, H. "Lead-free barium titanate ceramics with large piezoelectric constant fabricated by microwave sintering". *Japanese Journal of Applied Physics. Part 2-Letters & Express Letters*, 2006, 45(1-3) p. L30-L32.
60. Takahashi, H. "Piezoelectric properties of BaTiO₃ ceramics with high performance fabricated by microwave sintering". *Japanese Journal of Applied Physics. Part 1-Regular Papers Brief Communications & Review Papers*, 2006 45(9B) p. 7405-7408.
61. Takahashi, H. "Considerations for BaTiO₃ ceramics with high piezoelectric properties fabricated by microwave sintering method". *Japanese Journal of Applied Physics*, 2008 47(11) p. 8468-8471.
62. Karaki, T.; Yan, K.; Adachi, M. "Barium titanate piezoelectric ceramics manufactured by two-step sintering". *Japanese Journal of Applied Physics. Part 1- Regular Papers Brief Communications & Review Papers*, 2007, 46(10B) p. 7035-7038.
63. Karaki, T. "Lead-free piezoelectric ceramics with large dielectric and piezoelectric constants manufactured from BaTiO₃ nano-powder". *Japanese Journal of Applied Physics. Part 2-Letters & Express Letters*, 2007. 46(4-7) p. L97-L98.
64. Egerton, L.; Dillon, D.M. "Piezoelectric and dielectric properties of ceramics in the system potassium sodium niobate". *Journal of the American Ceramic Society*, 1959 42(9) p. 438-442.
65. Popper, P.; Ruddlesden, S.N.; Ingles, T.A. "Structure and electric properties of Bi₄Ti₃O₁₂ and its application in dielectrics". *Trans. Br. Ceram. Soc.*, 1957 56 p. 356-365.

66. Buhrer, C.F., "Some properties of bismuth perovskites". *Journal of Chemical Physics*, 1962 36(3) p. 798.
67. Wada, T., et al., "Dielectric and piezoelectric properties of $(\text{A}_{0.5}\text{Bi}_{0.5})\text{TiO}_3$ - ANbO_3 (A = Na, K) systems". *Japanese Journal of Applied Physics Part 1-Regular Papers Short Notes & Review Papers*, 2001 40(9B) p. 5703-5705.
68. Hiruma, Y., et al., "Ferroelectric and piezoelectric properties of $\text{Bi}_{1/2}\text{K}_{1/2}\text{TiO}_3$ ceramics fabricated by hot-pressing method". *Journal of Electroceramics*, 2008 21(1-4) p.296-299.
69. Hiruma, Y.; Nagata, H.; Takenaka, T. "Grain-size effect on electrical properties of $\text{Bi}_{1/2}\text{K}_{1/2}\text{TiO}_3$ ceramics". *Japanese Journal of Applied Physics Part 1-Regular Papers Brief Communications & Review Papers*, 2007 46(3 A) p. 1081-1084.
70. Smolenskii, G.A., et al., "New ferroelectrics of complex composition". *Soviet Physics-Solid State*, 1961 2(11) p. 2651-2654.
71. Jones, G.O.; Thomas, P.A. "Investigation of the structure and phase transitions in the novel A-site substituted distorted perovskite compound $\text{Na}_{0.5}\text{Bi}_{0.5}\text{TiO}_3$ ". *Acta Crystallographica Section B-Structural Science*, 2002 58 p. 168-178.
72. Roleder, K.; Suchanicz, J.; Kania, A. "Time-dependence of electric permittivity in $\text{Na}_{0.5}\text{Bi}_{0.5}\text{TiO}_3$ single-crystals". *Ferroelectrics*, 1989 89 p. 1-5.
73. Suchanicz, J., "Investigations of the phase transitions in $\text{Na}_{0.5}\text{Bi}_{0.5}\text{TiO}_3$ ". *Ferroelectrics*, 1995 172(1) p. 455 - 458.
74. Suchanicz, J., et al., "Electrostrictive strain and pyroeffect in the region of phase coexistence in $\text{Na}_{0.5}\text{Bi}_{0.5}\text{TiO}_3$ ". *Ferroelectrics*, 1988 77 p. 107-110.
75. Sakata, K.; Masuda, Y. "Ferroelectric and antiferroelectric properties of $(\text{Na}_{0.5}\text{Bi}_{0.5})\text{TiO}_3$ - SrTiO_3 solid-solution ceramics". *Ferroelectrics*, 1974 7(1-4) p. 347-349.
76. Nagata, H., et al., "Developments in dielectric materials and electronic devices". *Ceramic Transactions*, 2004 167 p. 8.
77. Nemoto, M., et al., "Electrical properties of textured $(\text{Bi}_{1/2}\text{K}_{1/2})\text{TiO}_3$ - BaTiO_3 lead free piezoelectric ceramics". *Japanese Journal of Applied Physics*, 2009 48(7) p.07GA04.
78. Nemoto, M., et al., "Fabrication and piezoelectric properties of grain-oriented $(\text{Bi}_{1/2}\text{K}_{1/2})\text{TiO}_3$ - BaTiO_3 Ceramics". *Japanese Journal of Applied Physics*, 2008 47(5) p. 3829-3832.
79. Takenaka, T.; Maruyama, K.; Sakata, K. " $(\text{Bi}_{1/2}\text{Na}_{1/2})\text{TiO}_3$ - BaTiO_3 system for lead-free piezoelectric ceramics". *Japanese Journal of Applied Physics Part 1- Regular Papers Short Notes & Review Papers*, 1991 30(9B) p. 2236-2239.

80. Takenaka, T.; Nagata, H. "Present status of non-lead-based piezoelectric ceramics, in Electroceramics" in Japan I, N. Mizutani, et al., Editors. 1999, *Trans Tech Publications: Clausthal Zellerfe*. p. 57-63.
81. Takenaka, T.; Sakata, K.; Toda, K. "Piezoelectric properties of $(\text{Bi}_{1/2}\text{Na}_{1/2})\text{TiO}_3$ -based ceramics". *Ferroelectrics*, 1990 106 p. 375-380.
82. Li, H.D.; Feng, C.D.; Yao, W.L. "Some effects of different additives on dielectric and piezoelectric properties of $(\text{Bi}_{1/2}\text{Na}_{1/2})\text{TiO}_3$ - BaTiO_3 morphotropic phase- boundary composition". *Materials Letters*, 2004 58(7-8) p. 1194-1198.
83. Xu, C.G.; Lin, D.M.; Kwok, K.W. "Structure, electrical properties and depolarization temperature of $(\text{Bi}_{0.5}\text{Na}_{0.5})\text{TiO}_3$ - BaTiO_3 lead-free piezoelectric ceramics". *Solid State Sciences*, 2008 10(7) p. 934-940.
84. Chen, M., et al., "Structure and electrical properties of $(\text{Na}_{0.5}\text{Bi}_{0.5})_{(1-x)}\text{Ba}_x\text{TiO}_3$ piezoelectric ceramics". *Journal of the European Ceramic Society*, 2008 28(4) p. 843-849.
85. Chu, B.J., et al., "Electrical properties of $(\text{Na}_{1/2}\text{Bi}_{1/2})\text{TiO}_3$ - BaTiO_3 ceramics". *Journal of the European Ceramic Society*, 2002 22(13) p. 2115-2121.
86. Oh, T.; Kim, M.H. "Phase relation and dielectric properties in $(\text{Bi}_{1/2}\text{Na}_{1/2})\text{Ba}_x\text{TiO}_3$ lead-free ceramics. Materials Science and Engineering B-Solid State Materials for Advanced Technology, 2006 132(3) p. 239-246. 93.
87. Lin, D.; Kwok, K.W.; Chan, H.L.W. "Structure and electrical properties of $\text{Bi}_{0.5}\text{Na}_{0.5}\text{TiO}_3$ - BaTiO_3 - $\text{Bi}_{0.5}\text{Li}_{0.5}\text{TiO}_3$ lead-free piezoelectric ceramics". *Solid State Ionics*, 2008 178(37-38) p. 1930-1937.
88. Lin, D.M., et al., "Piezoelectric and ferroelectric properties of lead-free $\text{Bi}_{1-y}(\text{Na}_{1-x-y}\text{Li}_x)-0.5\text{Ba}_y\text{TiO}_3$ ceramics". *Journal of the European Ceramic Society*, 2006 26(15) p. 3247-3251.
89. Elkechai, O.; Manier, M.; Mercurio, J.P., " $\text{Na}_{0.5}\text{Bi}_{0.5}\text{TiO}_3$ - $\text{K}_{0.5}\text{Bi}_{0.5}\text{TiO}_3$ (NBTKBT) system: A structural and electrical study". *Physica Status Solidi a-Applied Research*, 1996 157(2) p. 499-506.
90. Sasaki, A., et al., "Dielectric and piezoelectric properties of $(\text{Bi}_{0.5}\text{Na}_{0.5})\text{TiO}_3$ - $(\text{Bi}_{0.5}\text{K}_{0.5})\text{TiO}_3$ systems". *Japanese Journal of Applied Physics Part 1-Regular Papers Short Notes & Review Papers*, 1999 38(9B) p. 5564-5567.
91. Zhao, S.C., et al., "Ferroelectric and piezoelectric properties of $(\text{Na}, \text{K})_{0.5}\text{Bi}_{0.5}\text{TiO}_3$ lead free ceramics". *Journal of Physics D-Applied Physics*, 2006 39(10) p. 2277-2281.
92. Yang, Z.P., et al., "Structure and electrical properties of $(1-x)\text{Bi}_{0.5}\text{Na}_{0.5}\text{TiO}_3$ - $x\text{Bi}_{0.5}\text{K}_{0.5}\text{TiO}_3$ ceramics near morphotropic phase boundary". *Materials Research Bulletin*, 2008 43(1) p. 81-89.

93. Yoshii, K., et al., "Electrical properties and depolarization temperature of $(\text{Bi}_{1/2}\text{Na}_{1/2})\text{TiO}_3$ - $(\text{Bi}_{1/2}\text{K}_{1/2})\text{TiO}_3$ lead-free piezoelectric ceramics". *Japanese Journal of Applied Physics Part 1-Regular Papers Brief Communications & Review Papers*, 2006 45(5B) p. 4493-4496.
94. Zhang, Y.R.; Li, J.F.; Zhang, B.P., "Enhancing electrical properties in NBT/KBT lead-free piezoelectric ceramics by optimizing sintering temperature". *Journal of the American Ceramic Society*, 2008 91(8) p. 2716-2719.
95. Oh, T., "Dielectric relaxor properties in the system of $(\text{Na}_{1-x}\text{K}_x)_{1/2} \text{Bi}_{1/2}\text{TiO}_3$ ceramics". *Japanese Journal of Applied Physics Part 1-Regular Papers Brief Communications & Review Papers*, 2006 45(6A) p. 5138-5143.
96. Zhang, S.J., et al., "Piezoelectric properties in $\text{K}_{0.5}\text{Bi}_{0.5}\text{TiO}_3$ - $(\text{Na}_{0.5}\text{Bi}_{0.5})\text{TiO}_3$ - BaTiO_3 lead-free ceramics". *Ieee Transactions on Ultrasonics Ferroelectrics and Frequency Control*, 2007 54(5) p. 910-917.
97. Hiruma, Y., et al., "Piezoelectric properties and depolarization temperatures of $(\text{Bi}_{1/2}\text{Na}_{1/2})\text{TiO}_3$ - $(\text{Bi}_{1/2}\text{K}_{1/2})\text{TiO}_3$ - BaTiO_3 lead-free piezoelectric ceramics", in *Electroceramics in Japan IX*, K. Katayama, et al., Editors. 2006, *Trans Tech Publications Ltd: Stafa-Zurich*. p. 23-26.
98. Nagata, P.L., et al., "Large piezoelectric constant and high Curie temperature of lead-free piezoelectric ceramic ternary system based on bismuth sodium titanate-bismuth potassium titanate-barium titanate near the morphotropic phase boundary". *Japanese Journal of Applied Physics Part 1-Regular Papers Short Notes & Review Papers*, 2003 42(12) p. 7401-7403.
99. Makiuchi, Y., et al., " $(\text{Bi}_{1/2}\text{Na}_{1/2})\text{TiO}_3$ - $(\text{Bi}_{1/2}\text{K}_{1/2})\text{TiO}_3$ - BaTiO_3 -based lead-free piezoelectric ceramics". *Japanese Journal of Applied Physics Part 1-Regular Papers Brief Communications & Review Papers*, 2005 44(6B) p. 4350-4353.
100. Lin, D.M., et al., "Electrical properties of $\text{Bi}_{1-z}(\text{Na}_{1-x-y-z}\text{K}_x\text{Li}_y)(0.5)\text{Ba}_z\text{TiO}_3$ multicomponent lead-free piezoelectric ceramics". *Physica Status Solidi a-Applications and Materials Science*, 2005 202(9) p. R89-R91.
101. Saito, Y., et al., "Lead-free piezoceramics". *Nature*, 2004 432(7013) p. 84-87.
102. Cross, E., "Materials science - lead-free at last". *Nature*, 2004 432(7013) p. 24-25.
103. Matthias, B.T. and J.P. Remeika, "Dielectric properties of sodium and potassium niobates". *Physical Review*, 1951 82(5) p. 727-729.
104. Shirane, G., et al., "Phase transitions in ferroelectric KNbO_3 ". *Physical Review*, 1954 93(4) p. 672-673.

105. Nakamura, K.; Kawamura, Y., "Orientation dependence of electromechanical coupling factors in KNbO_3 ". *Ieee Transactions on Ultrasonics Ferroelectrics and Frequency Control*, 2000 47(3) p. 750-755.
106. Zgonik, M., et al., "Materials constants of KNbO_3 relevant for electrooptics and acoustooptics". *Journal of Applied Physics*, 1993 74(2) p. 1287-1297.
107. Nakamura, K.; Oshiki, M., "Theoretical analysis of horizontal shear mode piezoelectric surface acoustic waves in potassium niobate". *Applied Physics Letters*, 1997 71(22) p. 3203-3205.
108. Davis, M., et al., "Large and stable thickness coupling coefficients of 001 (C)-oriented KNbO_3 and Li-modified $(\text{K,Na})\text{NbO}_3$ single crystals". *Applied Physics Letters*, 2007 90(6) p. 062904.
109. Nagata, H., et al., "Fabrication and electrical properties of potassium niobate ferroelectric ceramics". *Japanese Journal of Applied Physics Part 1-Regular Papers Brief Communications & Review Papers*, 2007 46(10B) p. 7084-7088.
110. Li, E.Z., et al., "A shear-mode ultrasonic motor using potassium sodium niobate-based ceramics with high mechanical quality factor". *Japanese Journal of Applied Physics*, 2008 47(9) p. 7702-7706.
111. Hikita, K., et al., "Shear-Mode Piezoelectric Properties of KNbO_3 -Based Ferroelectric Ceramics. *Japanese Journal of Applied Physics*, 2009 48(7) p. 07GA05.
112. Wood, E.A., "Polymorphism in potassium niobate, sodium niobate, and other ABO_3 compounds". *Acta Crystallographica*, 1951 4(4) p. 353-362.
113. Ahtee, M.; Glazer, A.M. "Lattice-parameters and tilted octahedra in sodium potassium niobate solid-solutions". *Acta Crystallographica Section A*, 1976 32 p. 434.
114. Ahtee, M.; Hewat, A.W. "Structural phase-transitions in sodium-potassium niobate solid-solutions by neutron powder diffraction". *Acta Crystallographica Section A*, 1978 34(MAR) p. 309-317.
115. Birol, H.; Damjanovic, D.; Setter, N. "Preparation and characterization of $(\text{K}_{0.5}\text{Na}_{0.5})\text{NbO}_3$ ceramics". *Journal of the European Ceramic Society*, 2006 26(6) p. 861-866.
116. Du, H.L., et al., "Preparation and piezoelectric properties of $(\text{K}_{0.5}\text{Na}_{0.5})\text{NbO}_3$ lead free piezoelectric ceramics with pressure-less sintering". *Materials Science and Engineering B-Solid State Materials for Advanced Technology*, 2006 131(1-3) p. 83-87.
117. Matsubara, M., et al, "Sinterability and piezoelectric properties of $(\text{K,Na})\text{NbO}_3$ ceramics with novel sintering aid". *Japanese Journal of Applied Physics Part 1- Regular Papers Short Notes & Review Papers*, 2004 43(10) p. 7159-7163.

118. Matsubara, M., et al., "Synthesis and characterization of $(K_{0.5}Na_{0.5})(Nb_{0.7}Ta_{0.3})O_3$ piezoelectric ceramics sintered with sintering aid $K_{5.4}Cu_{1.3}Ta_{10}O_{29}$ ". *Japanese Journal of Applied Physics Part 1-Regular Papers Brief Communications & Review Papers*, 2005 44(9A) p. 6618-6623.
119. Matsubara, M., et al., "Processing and piezoelectric properties of lead-free $(K,Na)(Nb,Ta)O_3$ ceramics". *Journal of the American Ceramic Society*, 2005 88(5) p. 1190-1196.
120. Jaeger, R.E.; Egerton, L. "Hot pressing of potassium-sodium niobates". *Journal of the American Ceramic Society*, 1962 45(5) p. 209-213.
121. Haertlin, G.H., "Properties of hot-pressed ferroelectric alkali niobate ceramics". *Journal of the American Ceramic Society*, 1967 50(6) p. 329.
122. Egerton, L.; Bieling, C.A. "Isostatically hot-pressed sodium-potassium niobate transducer material for ultrasonic devices". *American Ceramic Society Bulletin*, 1968 47(12) p. 1151.
123. Wang, R.P., et al., "Fabrication and characterization of potassium-sodium niobate piezoelectric ceramics by spark-plasma-sintering method". *Materials Research Bulletin*, 2004 39(11) p. 1709-1715.
124. Li, J.F., et al., "Ferroelectric and piezoelectric properties of fine-grained $Na_{0.5}K_{0.5}NbO_3$ lead-free piezoelectric ceramics prepared by spark plasma sintering". *Journal of the American Ceramic Society*, 2006 89(2) p. 706-709.
125. Zhang, B.P., et al., "Compositional dependence of piezoelectric properties in $Na_xK_{1-x}NbO_3$ lead-free ceramics prepared by spark plasma sintering". *Journal of the American Ceramic Society*, 2006 89(5) p. 1605-1609.
126. Saito, Y.; Takao, H. "High performance lead-free piezoelectric ceramics in the $(K,Na)NbO_3$ - $LiTaO_3$ solid solution system". *Ferroelectrics*, 2006 338 p. 1433-1448.
127. Guo, Y.P.; Kakimoto, K.; Ohsato, H. " $(Na_{0.5}K_{0.5})NbO_3$ - $LiTaO_3$ lead-free piezoelectric ceramics". *Materials Letters*, 2005 59(2-3) p. 241-244.
128. Kim, M.S.; Jeong, S.J.; Song, J.S. "Microstructures and piezoelectric properties in the Li_2O -Excess $0.95(Na_{0.5}K_{0.5})NbO_3$ - $0.05LiTaO_3$ ceramics". *Journal of the American Ceramic Society*, 2007 90(10) p. 3338-3340.
129. Rubio-Marcos, F.; Ochoa, P.; Fernandez, J.F. "Sintering and properties of lead free $(K,Na,Li)(Nb,Ta,Sb)O_3$ ceramics". *Journal of the European Ceramic Society*, 2007 27(13-15) p. 4125-4129.
130. Chang, Y.F., et al., "Effects of Li content on the phase structure and electrical properties of lead-free $(K_{0.46-x/2}Na_{0.54-x/2}Li_x)(Nb_{0.76}Ta_{0.2}Sb_{0.04})O_3$ ceramics". *Applied Physics Letters*, 2007 90(23) p. 232905.

131. Zhang, S.J., et al., "Piezoelectric properties in perovskite $0.948(\text{K}_{0.5}\text{Na}_{0.5})\text{NbO}_3$ - 0.052LiSbO_3 lead-free ceramics". *Journal of Applied Physics*, 2006 100(10) p.104-108.
132. Yang, Z., et al., "Effects of composition on phase structure, microstructure and electrical properties of $(\text{K}_{0.5}\text{Na}_{0.5})\text{NbO}_3$ - LiSbO_3 ceramics". *Materials Science and Engineering A-Structural Materials Properties Microstructure and Processing*, 2006 432(1-2) p. 292-298.
133. Wu, J.G., et al., "Phase structure and electrical properties of $(\text{K}_{0.48}\text{Na}_{0.52})(\text{Nb}_{0.95}\text{Ta}_{0.05})\text{O}_3$ - LiSbO_3 lead-free piezoelectric ceramics". *Journal of the American Ceramic Society*, 2008 91(1) p. 319-321.
134. Akdogan, E.K., et al., "Origin of high piezoelectric activity in ferroelectric $(\text{K}_{0.44}\text{Na}_{0.52}\text{Li}_{0.04})$ - $(\text{Nb}_{0.84}\text{Ta}_{0.1}\text{Sb}_{0.06})\text{O}_3$ ceramics". *Applied Physics Letters*, 2008 92(11) p. 112908.
135. Zhang, S.J.; Xia, R.; Shrout, T.R. "Modified $(\text{K}_{0.5}\text{Na}_{0.5})\text{NbO}_3$ based lead-free piezoelectrics with broad temperature usage range". *Applied Physics Letters*, 2007 91(13) p.132913.
136. Zhang, S.J., et al., "Mitigation of thermal and fatigue behavior in $\text{K}_{0.5}\text{Na}_{0.5}\text{NbO}_3$ -based lead free piezoceramics". *Applied Physics Letters*, 2008 92(15) p. 152904.
137. Zhang, S.J.; Xia, R.; Shrout, T.R. "Lead-free piezoelectric ceramics vs. PZT?" *Journal of Electroceramics*, 2007 19(4) p. 251-257.
138. Shrout, T.R.; Eitel, R.E.; Randall, C.A., "High performance, high temperature perovskite piezoelectric ceramics in Piezoelectric Materials in Devices", N. Setter, Editor. 2002, *EPFL Swiss Federal Institute of Technology*: Lausanne, Switzerland.
139. Hiruma, Y., et al., "Ferroelectric and piezoelectric properties of $(\text{Bi}_{1/2}\text{K}_{1/2})\text{TiO}_3$ ceramics". *Japanese Journal of Applied Physics Part 1-Regular Papers Brief Communications & Review Papers*, 2005 44(7A) p. 5040-5044.
140. Chang, Y.F., et al., "< 001 > textured $((\text{K}_{0.5}\text{Na}_{0.5})\text{Nb}_{0.97}\text{Sb}_{0.03})\text{O}_3$ piezoelectric ceramics with high electromechanical coupling over a broad temperature range". *Applied Physics Letters*, 2009 95(23) p. 232905.
141. Lei, C.; Ye, Z.G. "Lead-free piezoelectric ceramics derived from the $\text{K}_{0.5}\text{Na}_{0.5}\text{NbO}_3$ - AgNbO_3 solid solution system". *Applied Physics Letters*, 2008 93(4) p. 042901.
142. Hollenstein, E., et al., "Piezoelectric properties of Li- and Ta-modified $(\text{K}_{0.5}\text{Na}_{0.5})\text{NbO}_3$ ceramics". *Applied Physics Letters*, 2005 87(18) p. 182905.
143. Zhang, J.L., et al., "Polymorphic phase transition and excellent piezoelectric performance of $(\text{K}_{0.55}\text{Na}_{0.45})_{0.965}\text{Li}_{0.035}\text{Nb}_{0.8}\text{Ta}_{0.2}\text{O}_3$ lead-free ceramics". *Applied Physics Letters*, 2009 95(2) p. 022909.

144. Wang, R., et al., "Enhanced piezoelectricity around the tetragonal/orthorhombic morphotropic phase boundary in (Na,K)NbO₃-ATiO₃ solid solutions". *Journal of Electroceramics*, 2008 21(1-4) p. 263-266.
145. Guo, Y.P.; Kakimoto, K; Ohsato, H. "Phase transitional behavior and piezoelectric properties of (Na_{0.5}K_{0.5})NbO₃ -LiNbO₃ ceramics". *Applied Physics Letters*, 2004 85(18) p. 4121-4123.
146. Hao, J.G., et al., "Structure and electrical properties of (Li, Sr, Sb)-modified K_{0.5}Na_{0.5}NbO₃ lead-free piezoelectric ceramics". *Journal of Alloys and Compounds*, 2009 479(1-2) p. 376-380.
147. Zuo, R.Z.; Fu, J.; Lv, D.Y. "Phase transformation and tunable piezoelectric properties of lead-free (Na_{0.52}K_{0.48-x}Li_x)(Nb_{1-x-y}Sb_yTa_x)O₃ System". *Journal of the American Ceramic Society*, 2009 92(1) p. 283-285.
148. Safari, A., et al, "(K_{0.44},Na_{0.52},Li_{0.04})(Nb_{0.84},Ta_{0.10}Sb_{0.06})O₃ ferroelectric ceramics". *Ieee Transactions on Ultrasonics Ferroelectrics and Frequency Control*, 2009 56(8) p. 1586-1594.
149. Fu, J., et al., "Structure and piezoelectric properties of lead-free (Na_{0.52}K_{0.44-x})(Nb_{0.95-x}Sb_{0.05})O₃-xLiTaO₃ ceramics". *Journal of Materials Science-Materials in Electronics*, 2010 21(3) p. 241-245.
150. Wang, Y.Y., et al., "Piezoelectric properties of (Li, Ag) modified (Na_{0.5}K_{0.5})NbO₃ lead-free ceramics with high Curie temperature". *Journal of Alloys and Compounds*, 2008 459(1-2) p. 414-417.
151. Wang, Y.Y., et al., "Piezoelectric properties of (1-x)(Na_{0.5}K_{0.5})NbO₃-xAgSbO₃ lead-free ceramics". *Journal of the American Ceramic Society*, 2009 92(3) p. 755-757.
152. Gibson, R.F., et al., "A review of recent research on mechanics of multifunctional composite materials and structures". *Composite Structures*, 2010 92 p. 2793–2810.
153. Bauhofer, W.; Kovacs, J.Z. "A review and analysis of electrical percolation in carbon nanotube polymer composites". *Compos Sci Technol* 2009 69(10): 1486–98.
154. Li, J.; Ma, P.C.; Chow, W.S.; To, C.K.; Tang, B.Z.; Kim, J-K. "Correlations between percolation threshold, dispersion state, and aspect ratio of carbon nanotubes". *Advanced Functional Materials* 2007 17 p.3207–15.
155. Gibson, T.; Putthanarat, S.; Fielding, J.C.; Drain, A.; Will, K.; Stoffel, M. "Conductive nanocomposites: focus on lightning strike protection". In: *Proc int SAMPE tech conf and exhibition – from art to science: advancing mater and proc eng*; 2007.
156. Allaoui, A.; Bai, S.; Cheng, H.M.; Bai, J.B. "Mechanical and electrical properties of a MWNT/epoxy composite". *Compos Sci Technol* 2002 62 p.1993–8.

157. Qiu, J.; Zhang, C.; Wang, B.; Liang, R. "Carbon nanotube integrated multifunctional composites". *Nanotechnology* 2007 18 p.275708.
158. Kalaitzidou, K.; Fukushima, H.; Drzal, L.T. "Multifunctional polypropylene composites produced by incorporation of exfoliated graphite nanoplatelets". *Carbon* 2007 45 p.1446–52.
159. Cebeci, H.; Guzman de Villoria, R.; Hart, A.J.; Wardle, B.L. "Multifunctional properties of high volume fraction aligned carbon nanotube polymer composites with controlled morphology". *Compos Sci Technol* 2009 69 p.2649–56.
160. Sandler, J.K.W.; Kirk, J.E.; Kinloch, I.A.; Shaffer, M.S.P.; Windle, A.H. "Ultra-low electrical percolation threshold in carbon-nanotube–epoxy composites". *Polymer* 2003 44 p.5893–9.
161. Thostenson, E.T.; Ziaee, S.; Chou, T-W. "Processing and electrical properties of carbon nanotube/vinyl ester nanocomposites". *Compos Sci Technol* 2009 69 p.801–4.
162. Shenogina, N.; Shenogin, S.; Xue, L.; Keblinski, P. "On the lack of thermal percolation in carbon nanotube composites". *Applied Physics Letters* 2005 87 p.133106.
163. Biercuk, M.J.; Llaguno, M.C.; Radosavljevic, M.; Hyun, J.K.; Johnson, A.T. "Carbon nanotube composites for thermal management". *Applied Physics Letters* 2002 80(15) p.2767–9.
164. Bonnet, P, Sireude, D.; Garnier, B.; Chauvet, O. "Thermal properties and percolation in carbon nanotube–polymer composites". *Applied Physics Letter* 2007 91 p.201910.
165. Kim, Y.A.; Kamio, S.; Tajiri, T.; Hayashi, T.; Song, S.M.; Endo, M. et al. "Enhanced thermal conductivity of carbon fiber/phenolic resin composites by the introduction of carbon nanotubes". *Applied Physics Letter* 2007 90 p.093125.
166. Ganguli, S.; Roy, A.K.; Anderson, D.P. "Improved thermal conductivity for chemically functionalized exfoliated graphite/epoxy composites". *Carbon* 2008 46(5) p.806–17.
167. Sihn, S.; Ganguli, S.; Roy, A.K.; Qu, L.; Dai, L. "Enhancement of through-thickness thermal conductivity in adhesively bonded joints through using aligned carbon nanotubes". *Composite Science Technology* 2008;68:658–65.
168. Li, C.; Thostenson, E.T.; Chou, T-W. "Sensors and actuators based on carbon nanotubes and their composites: a review". *Compos Sci Technol* 2008 68 p.1227–49.
169. Gibson, R.F.; Ayorinde, E.O.; Wen, Y-F. "Vibrations of carbon nanotubes and their composites: a review". *Compos Sci Technol* 2007 67 1–28.
170. Ratna, D.; Karger-Kocsis, J. "Recent advances in shape memory polymers and composites: a review". *J Mater Sci* 2008;43(1):254–69.

171. Lesieutre, G.A.; Davis, C.L. "Can a coupling coefficient of a piezoelectric device be higher than those of its active material?" *J Intell Mater Syst Struct* 1997 8(10) p.859–67.
172. Giurgiutiu, V.; Zagrai, A.N. "Characterization of piezoelectric wafer active sensors". *J Intell Mater Syst Struct* 2001 11(12) p.959–76.
173. Muralt, P.; Polcawich, R.G.; Troiler-McKinstry, S. "Piezoelectric thin films for sensors, actuators and energy harvesting". *MRS Bull* 2009 34(9) p.658–664.
174. Tadigadapa, S.; Mateti, K. "Piezoelectric MEMS sensors: state-of-the-art and perspectives". *Meas Sci Technol* 2009 20 p.092001.
175. Hagood, N.W.; Bent, A.A. "Development of piezoelectric fiber composites for structural actuation". In: *Proc 34th AIAA structures, structural dynamics and mater conference*; AIAA paper no. 93-1717, La Jolla, CA; 1993.
176. Bent, A.A.; Hagood, N.W.; Rogers, J.P. "Anisotropic actuation with piezoelectric fiber composites". *J Intell Mater Syst Struct* 1995 6 p.338–349.
177. Fernandez, J.F.; Dogan A, Zhang QM, Tressler JF, Newnham RE. "Hollow piezoelectric composites". *Sens Actuators, A* 1996 51 p.183–192.
178. Brei, D.; Cannon, B.J. "Piezoceramic hollow fiber active composites". *Composite Science Technology* 2004 64 p.245–261.
179. Fuchs, A.; Shang, Q.; Elkins, J.; Gordaninejad, F.; Evremsel, C. "Development and characterization of magnetorheological elastomers". *Journal Applied Polymer Science* 2007 105 p.2497–508.
180. Montalvao, D.; Maia, N.M.M.; Ribeiro, A.M.R. "A review of vibration-based structural health monitoring with special emphasis on composite materials". *Shock Vibration Digest* 2006 38(4) p.295–324.
181. Zou, Y.; Tong, L.; Steven, G.P. "Vibration-based model dependent damage identification and health monitoring for composite structures – a review". *J Sound Vib* 2000 230(2) p.357–78.
182. Wu, D.Y.; Meure, S.; Solomon, D. "Self-healing polymeric materials: a review of recent developments". *Prog Polym Sci* 2008 33(5) p.479–522.
183. Park, G.; Rosing, T.; Todd, M.D.; Farrar, C.R.; Hodgkiss, W. "Energy harvesting for structural health monitoring sensor networks". *J Infrastruct Syst* 2008 14(1) p.64–79.
184. Lin, M.; Chang, F-K. "The manufacture of composite structures with a built-in network of piezoceramics". *Compos Sci Technol* 2002 62 p.919–39.
185. Qing, X.P.; Beard, S.; Kumar, A.; Ooi, T.K.; Chang, F-K. "Built-in sensor network for structural health monitoring of composite structure". *J Intell Mater Syst Struct* 2007 18(1) p.39–49.

186. Wu, Z.; Qing, X.P.; Chang, F.-K. "Damage detection for composite laminate plates with a distributed hybrid PZT/FBG sensor network". *J Intell Mater Syst Struct* 2009 20 p.1069–77.
187. Su, Z.; Wang, X.; Chen, Z.; Ye, L.; Wang, D. "A built-in active sensor network for health monitoring of composite structures". *Smart Mater Struct* 2006 15 p.1939–49.
188. Su, Z.; Wang, X.; Chen, Z.; Ye, L. "Damage assessment of multi-layered composite structure using an embedded active sensor network". *Key Eng Mater* 2007 334–335 p.461–464.
189. Watkins, S.E.; Akhavan, F.; Dua, R.; Chandrashekhara, K.; Wunsch, D.C. "Impact-induced damage characterization of composite plates using neural networks". *Smart Mater Struct* 2007 16 p.515–524.
190. Haywood, J.; Coverley, P.T.; Staszewski, W.J.; Worden, K. "An automated impact monitor for a composite panel employing smart sensor technology". *Smart Mater Struct* 2005 14 p.265–271.
191. Yu, L.; Cheng, L.; Yam, L.H.; Yan, Y.J.; Jiang, J.S. "Online damage detection for laminated composite shells partially filled with fluid". *Compos Struct* 2007 80 p.334–342.
192. Srivastava, A.; Agarwal, A.; Chakraborty, D.; Dutta, A. "Control of smart laminated FRP structures using artificial neural networks". *J Reinf Plast Compos* 2005 24(13) p.1353–1364.
193. Loh, K.J.; Kim, J.; Lynch, J.P.; Kam, N.W.S.; Kotov, N. "Multifunctional layer-by-layer carbon nanotube-polyelectrolyte thin films for strain and corrosion sensing". *Smart Mater Struct* 2007 16 p.429–438.
194. Loh, K.J.; Lynch, J.P.; Kotov, N. "Passive wireless sensing using SWMT-based multifunctional thin film patches". *Int J Appl Electromag Mech* 2008;28: 887–94.
195. Olek, M.; Ostrander, J.; Jurga, S.; Mohwald, H.; Kotov, N.; Kempa, K, et al. "Layer-by-layer assembled composites from multiwall carbon nanotubes with different morphologies". *Nano Lett* 2004 4(10) p.1889–95.
196. Shim, B.S.; Starkovich, J.; Kotov, N. "Multilayer composites from vapor-grown carbon nano-fibers". *Compos Sci Technol* 2006 66 p.1174–1181.
197. Sodano, H.A.; Inman, D.J.; Park, G. "A review of power harvesting from vibration using piezoelectric materials". *Shock Vib Digest* 2004 36(3) p.197–205.
198. Anton, S.R.; Sodano, H.A. "A review of power harvesting using piezoelectric materials (2003–2006)". *Smart Mater Struct* 2007 16(3) p.R1–21.

199. Cook-Chennault, K.A.; Thambi, N.; Sastry, A.M. "Powering MEMS portable devices– a review of non-regenerative and regenerative power supply systems with special emphasis on piezoelectric energy harvesting systems". *Smart Mater Struct* 2008 17(4) p.043001.
200. Sodano, H.A.; Inman, D.J.; Park, G. "Generation and storage of electricity from power harvesting devices". *J Intell Mater Syst Struct* 2005 16(1) p.67–75.
201. Pereira, T.; Guo, Z.; Nieh, S.; Arias, J.; Hahn, H.T. "Embedding thin-film lithium energy cells in structural composites". *Compos Sci Technol* 2008 68 p.1935–41.
202. Pereira, T.; Guo, Z.; Nieh, S.; Arias, J.; Hahn, H.T. "Energy storage structural composites: a review". *J Compos Mater* 2009 43(5) p.549–60.
203. Kim, H.S.; Kang, J.S.; Park, J.S.; Hahn, H.T.; Jung, H.C.; Joung, J.W. "Inkjet printed electronics for multifunctional composite structure". *Compos Sci Technol* 2009 69(7–8) p.1256–1264.
204. Liu, P.; Sherman, E.; Jacobsen, A. "Design and fabrication of multifunctional structural batteries". *J Power Sources* 2009 189(1) p.646–50.
205. Snyder, J.F.; Carter, R.H.; Wetzel, E.D. "Electrochemical and mechanical behavior in mechanically robust solid polymer electrolytes for use in multifunctional structural batteries". *Chem Mater* 2007 19(15) p.3793–3801.
206. Snyder, J.F.; Wong, E.L.; Hubbard, C.W. "Evaluation of commercially available carbon fibers, fabrics and papers for potential use in multifunctional energy storage applications". *J Electrochem Soc* 2009 156(3) p.A215–24.
207. O'Brien, D.J.; Baechele, D.M.; Wetzel, E.D. "Multifunctional structural composite capacitors for US Army applications". *Proc int SAMPE tech conf, 38th fall tech conf: global adv mater proc eng*; 2006.
208. Baechele, D.M.; O'Brien, D.J.; Wetzel, E.D. "Design and processing of structural composite capacitors". *Proc int SAMPE symposium and exhibition, M and P– from coast to coast and around the world*; 2007.
209. Luo, X.; Chung, D.D.L. "Carbon fiber/polymer matrix composites as capacitors". *Compos Sci Technol* 2001 61(6) p.885–8.
210. White, S.R.; Sottos, N.R.; Geubelle, P.H.; Moore, J.S.; Kessler, M.R.; Sriram, S.R.; et al. "Autonomic healing of polymer composites". *Nature* 2001 409 p.794–797.
211. Brown, E.N.; Sottos, N.R.; White, S.R. "Fracture testing of a self-healing polymer composite". *Exp Mech* 2002 42 p.372–379.
212. Caruso, M.M.; Blaiszik, B.J.; White, S.R.; Sottos, N.R.; Moore, J.S. "Full recovery of fracture toughness using a nontoxic solvent-based self-healing system". *Advanced Functional Materials* 2008 18(13) p.1898–1904.

213. Brown, E.N.; White, S.R.; Sottos, N.R. "Retardation and repair of fatigue cracks in a microcapsule toughened epoxy composite – part I: manual infiltration". *Composite Science Technology* 2005 65 p.2466–473.
214. Brown, E.N.; White, S.R.; Sottos, N.R. "Retardation and repair of fatigue cracks in a microcapsule toughened epoxy composite – part II: in situ self-healing". *Composite Science Technology* 2005 65 p.2474–2480.
215. Brown, E.N.; White, S.R.; Sottos, N.R. "Fatigue crack propagation in microcapsule toughened epoxy". *Journal of Material Science* 2006 41(19) p.6266–6273.
216. Patel, A.J.; Sottos, N.R.; Wetzel, E.D.; White, S.R. "Autonomic healing of low-velocity impact damage in fiber-reinforced composites". *Compos Part A: Applied Science Manufacturing* 2010 41(3) p.360–8.
217. Cho, S.H.; White, S.R.; Braun, P.V. "Self-healing polymer coatings". *Advanced Materials* 2009 21(6) p.645–9.
218. Toohey, K.S.; Sottos, N.R.; Lewis, J.A.; Moore, J.S.; White, S.R. "Self-healing materials with microvascular networks". *Nat Mater* 2007 6 p.581–585.
219. Kirk, J.G.; Naik, S.; Moosbrugger, J.C.; Morrison, D.J.; Volkov, D.; Sokolov, I. "Self-healing epoxy composites based on the use of nanoporous silica capsules". *Int J Fract* 2009 159(1) p.101–102.
220. Privman, V.; Dementsov, A.; Sokolov, I. "Modeling of self-healing polymer composites reinforced with nanoporous glass fibers". *J Comput Theor Nanosci* 2007 4(1) p.190–193.
221. Williams, G.; Trask, R.; Bond, I. "A self-healing carbon fibre reinforced polymer for aerospace applications". *Compos Part A: Appl Sci Manuf.* 2007 38(6) p.1525–1532.
222. Yin, T.; Rong, M.Z.; Zhang, M.Q.; Zhao, J.Q. "Durability of self-healing woven glass fabric/epoxy composites". *Smart Mater Struct* 2009 18(7) p.074001.
223. Cannon, B.J. and Brei, D. 2000. "Feasibility Study of Microfabrication by Coextrusion (MFCX) Hollow Fibers for Active Composites," *Journal of Intelligent Material Systems and Structures*, 11: 659-669.
224. Williams, B.R.; Grimsley, B.W.; Inman, D.J.; Wilkie, W.K. "Manufacturing and Mechanics-Based Characterization of Macro Fiber Composite Actuators," *Proc of the ASME Int. Mech. Eng. Conf. and Exposition*, New Orleans, Louisiana. November, 2002.
225. Wilkie, W.K.; Bryant, R.G.; High, J.W.; Fox, R.L.; Hellbaum, R.F.; Jalink, A.; Little, B.D.; Mirick, P.H. "Low-Cost Piezocomposite Actuator for Structural Control Applications," *Proc. of 7th SPIE Int. Symp. on Smart Structures and Materials*, March, 2000.

226. Park, G.; Kim, M.H.; Inman, D.J. "Integration of Smart Materials into Dynamics and Control of Inflatable Space Structures," *Journal of Intelligent Materials Systems and Structures*, 2002, 12:423-433.
227. Bent, A.A. "Piezoelectric Fiber Composites for Structural Actuation," *Master of Science Thesis*, Massachusetts Institute of Technology. 1994.
228. Lin, Y.; Sodano, H.A. "Concept and model of a piezoelectric structural fiber for multifunctional composites". *Comp. Sc. And Tech.* 2006 68 p.1911-1918.
229. Halliday D, Resnick R. "Fundamentals of physics". *New York: John Wiley & Sons, Inc.*; 1988.
230. Hyer MW. "Stress analysis of fiber-reinforced composite materials". *New York: The McGraw-Hill companies, Inc.*; 1998.
231. Burcu Ertuğ, "The Overview of the Electrical Properties of Barium Titanate". *American Journal of Engineering Research*, 2, 2013, 01-07.
232. Christensen, R.M. "A critical evaluation for a class of micromechanics models". *J Mech Phys Solids* 1990; 38 p.379–404.
233. Christensen, R.M.; Schantz, H.; Shapiro, J. "On the range of validity of the Mori–Tanaka method". *J Mech Phys Solids* 1992; 40 p.69–73.
234. Benedikt, B; Rupnowski, P; Kumosa, M. "Visco-elastic stress distributions and elastic properties in unidirectional composites with large volume fractions of fibers". *Acta Mater.* 2003; 51(12) p.3483–93.
235. Dunn M.L. and Taya, M. "Micromechanics predictions of the effective electroelastic moduli of piezoelectric composites". *Int. J. Solids Struct.* 1993; 30 p.161–75.
236. Barnett, D.M. and Lothe, J. "Dislocations and line charges in anisotropic piezoelectric insulators". *Phys. staf. sol.* (b) 67, 105-111.
237. Odegard, G.M. "Constitutive modeling of piezoelectric polymer composites". *Acta Mater.* 2004; 52 p.5315–30.
238. Dunn, M.L; Taya, M. "An analysis of piezoelectric composite materials containing ellipsoidal inhomogeneities". *Proc. Roy. Soc. London, Ser A* 1993; 443 p.265–87.
239. Dunn, M.L; Ledbetter, H. "Elastic moduli of composites reinforced by multiphase particles". *J. Appl. Mech.* 1995; 62 p.1023–8.
240. Lin, Y; Sodano, H.A. "Fabrication and electromechanical characterization of a piezoelectric structural fiber for multifunctional composites". *SAMPE Fall Tech. Conf.* (Memphis, TN Sept. 2008)
241. Chen, X; Cheng, Y; Wu, K; Meng, Y; Wu, S. "Calculation of dielectric constant of two phase disordered composites by using FEM" *ISEI 2008: Conf. Record of the 2008 IEEE Int. Symp. on Electr. Insul.* p. 215–8
242. Chao, F; Bowler, N; Tan, X; Kessler, M.R. "Three phase composites for multifunctional structural capacitors". *SAMPE Fall Tech. Conf.* 2008 (Memphis, TN, Sept.)

VITA

Linda Vera was born on July 10th 1990 in El Paso TX. She is the first child of Raul Vera and Hilda Bernal. Ms. Linda Vera completed her Bachelor of Science in Mechanical Engineering in December 2012 from the University of Texas at El Paso. After completion of Bachelor's degree she started her Master of Science in Mechanical Engineering at the University of Texas at El Paso in January 2013 and was appointed as a Graduate Research Assistant. Ms. Vera also served as a Teaching Assistant and Undergraduate Peer Advisor during her master's degree, as well as having two conference paper publications. She started working as an Engineering Assistant for Bizlink Tech in April 2014.

Permanent address: 8216 Tonto Pl

El Paso, TX. 79904. USA

This thesis was typed by Linda Vera.